Title
Elucidating dynamics in soft materials using low-dose electron and cathodoluminescence microscopy

Author
Wai, Rebecca Bo-Lam

Publication Date
2021

Peer reviewed|Thesis/dissertation

Elucidating dynamics in soft materials using low-dose electron and cathodoluminescence microscopy

by

Rebecca Bo-Lam Wai

A dissertation submitted in partial satisfaction of the

requirements for the degree of

Doctor of Philosophy

in

Chemistry

in the

Graduate Division

of the

University of California, Berkeley

Committee in charge:

Professor Naomi Ginsberg, Chair
Professor Stephen Leone
Professor Markita Landry

Summer 2021

Elucidating dynamics in soft materials using low-dose electron and cathodoluminescence microscopy

Abstract

Elucidating dynamics in soft materials using low-dose electron and cathodoluminescence microscopy

by

Rebecca Bo-Lam Wai

Doctor of Philosophy in Chemistry

University of California, Berkeley

Professor Naomi Ginsberg, Chair

Real-space imaging provides real-space information about the properties of a sample, which in turn provides insight into the correlation between physical properties and different regions of the sample. With repeated imaging, we can record movies that reveal spatio-temporal correlations. Many processes that are important for life and in emergent technologies occur at the nanoscale, a length scale that is typically difficult for optical microscopies to access. In particular, observing dynamics in these systems proves to be challenging, where existing microscopy techniques provide different trade-offs in spatial resolution, temporal resolution, and sample damage. In this dissertation, we use low-dose scanning electron microscopy (SEM) and cathodoluminescence (CL) microscopy to elucidate dynamics in delicate materials at the nanoscale.

Chapter 2 focuses on using time-resolved cathodoluminescence (TRCL) microscopy to determine the spatial variation in the lifetime of a Mn^{2+} dopant in a metal halide perovskite. We observe enhanced Mn^{2+} luminescence at the edges of halide perovskite microplates. Using TRCL, we reveal two luminescent decay components that we attribute to two different Mn^{2+} populations. While each component appears to be present both near the surface and in the bulk, the origin of the intensity variation stems from a higher proportion of the longer lifetime component near the perovskite surface. We suggest that this increased CL emission is caused by an increased probability of electron-hole recombination on the Mn^{2+} dopant near the perovskite surface due to an increased trap concentration there.

Chapter 3 of this dissertation focuses on developments in cathodoluminescence-activated imaging by resonant energy transfer (CLAIRE) microscopy. We discuss the production of thin, free-standing scintillator imaging chips for CLAIRE imaging and demonstrate that CLAIRE is capable of imaging dynamic processes in both soft materials and with metal nanoparticle labels. We then discuss our efforts to expand CLAIRE capabilities to other samples. We developed an aqueous encapsulation scheme using multi-layer graphene to

expand the compatibility of CLAIRE imaging to samples that are otherwise incompatible with the vacuum environment of the experiment. Additionally, we report preliminary steps towards using CLAIRE imaging to study photosynthetic membranes.

Chapter 4 focuses on the use of a low-dose electron beam to both drive and record dynamics in an interfacial polycrystalline colloidal monolayer. We describe the formation of these polycrystalline monolayers at the surface of an ionic liquid droplet and the incorporation of large particle dopants in the polycrystalline lattice. We demonstrate that an electron beam perturbation drives a reduction in particle density in the center of the imaging field of view due to a combination of outward particle flow and detaching from the interface and becoming immersed into the bulk ionic liquid. We find that the rate of this reduction in particle density depends on the number of large particle dopants present in the lattice and discuss possible explanations for this dependence.

Together, these experiments demonstrate the utility of low-dose SEM and CL microscopy in capturing nanoscale dynamics in a variety of samples that are not typically robust to electron beam imaging. These methods extend nanoscale imaging to materials that are not compatible with other super-resolution imaging techniques or traditional electron microscopy, providing opportunities to explore dynamics in a wide range of other samples, from soft biological materials to next generation self assembled meta-materials.

To Mom and Dad

Contents

List of Figures

Acknowledgments

I would first like to thank my advisor, Prof. Naomi Ginsberg, for all of her support through my graduate career. Thank you for all of the encouraging advice, probing scientific questions, and last minute revisions.

Thank you to my cathodoluminescence comrades for making these experiments possible. To Namrata Ramesh, Jonathan Raybin, Connor Bischak, Jonathon Kruppe, Clarice Aiello, Craig Hetherington, and Claire Stachelrodt - team work makes the dream work, and none of this work would have happened without you. Thank you for all of the discussions, for teaching me how to do everything in the lab, and for being there with me.

Thank you to the other members of the Ginsberg Group past and present for their support, advice, and friendship. Hannah Weaver, Jenna Tan, Trevor Roberts, Milan Delor, Leo Hamerlynck, Christian Tanner, James Utterback, Rongfeng Yuan, Brendan Folie, Eniko Zsoldos, Dannielle McCarthy, Sam Penwell, Lucas Ginsberg, Rodrigo Noriega, and Ben Cotts- you are all the best. Thank you for making the D level of Hildebrand as wonderful as possible.

Thank you to Shaul Aloni, Frank Ogletree, Ed Barnard, and Ed Wong at the Molecular Foundry for their support.

Thank you to all of my collaborators, including Steve Zeltmann, Prof. Andrew Minor, Masakazu Iwai, Zhe Wang, Prof. Darrell Schlom, Dr. Charles Cherqui, Jacob Busche, Steven Quillin, and Prof. David Masiello.

Thank you to everyone in the Chemistry Department who keeps it running, especially to Jessie Woodcock, Ellen Levitan, Joel Adlen, Roy Washington, and Carl Lamey.

Thank you to the amazing fellow students and professors in the Haverford College Chemistry Department for getting me started on my journey in chemistry, Prof. Karin Akerfeldt, Prof. Fran Blase, Prof. Lou Charkoudian, Prof. Helen White, Prof. Alex Norquist, Prof. Rob Scarrow, Prof. Josh Schrier. A special and extra large thank you to Prof. Casey Londergan who gave me the best first experience in research and all of the skills and encouragement I needed to keep going.

Chapter 1

Introduction

1.1 Super-resolution microscopy and the diffraction limit

Imaging science enables access to real-space information, which can provide important insight into various aspects of many systems, such as correlations between properties of different regions of the sample. With the addition of time resolution, images can be used to create movies that directly show changes in both time and space, enabling further understanding of how these samples evolve and revealing spatio-temporal correlations. An important frontier for applications of imaging science is the size scale of the samples that are accessible to imaging techniques. Nanoscale samples and processes, ranging from protein motion in biological samples [1, 2] to colloidal nanoparticle assemblies [3, 4] have many mysteries to solve, where the size of the system presents both a new avenue for scientific inquiry but also a fundamental challenge to overcome.

Imaging science in the form of optical microscopy has been well developed and used widely across many fields. However, an important limitation exists for directly extending those capabilities to nanoscale samples. The optical diffraction limit restricts the resolving power of a very good traditional fluorescence microscope to about 200 nm, leaving many nanoscale processes out of reach [5]. Many approaches to imaging nanoscale samples have been developed, each with their own tradeoffs for size resolution, time resolution, and sample considerations. Here, we first provide an overview of available nanoscale imaging techniques. We then introduce the techniques used in this dissertation to probe various nanoscale phenomena.

1.2 Existing approaches to super-resolution imaging

The optical diffraction limit describes the size at which two features that are close together become impossible to distinguish with an optical microscope [5]. A single emitter in an

optical microscope will produce an Airy disk, comprised of a high intensity central emission surrounded by lower intensity "rings" produced by the constructive and destructive interference of the emitted light, which defines the resolution of an optical microscope in the focal plane [6]. This resolution is given by $\frac{\lambda}{2NA}$, where λ is the wavelength of the light used for imaging and NA is the numerical aperture of the imaging setup. Practical limitations to the enhancement of the NA in microscope objectives limit this approach to enhancing spatial resolution. Widely used nanoscale imaging techniques either use short wavelength light sources or clever optical techniques to circumvent the limitations of distinguishing Airy disks.

1.2.1 Short wavelength sources

UV and X-ray sources have shorter wavelengths than visible light and therefore can access smaller length scales even if they are diffraction limited. X-ray imaging can provide either real-space information, such as in scanning transmission X-ray microscopy or reciprocal space information, such as in X-ray diffraction techniques [7]. A major consideration for techniques based on these sources is that the interaction between the high energy source and the sample can result in unwanted sample damage, particularly in soft material samples [8]. In this case, samples may either be too susceptible to damage to image or repeated imaging to study dynamics may not be possible. However, UV and X-ray based imaging techniques are powerful resources for samples that are not adversely affected by the high energy.

1.2.2 Optical methods

Another strategy for super-resolution microscopies is to employ optical excitation with visible wavelengths, but to circumvent the optical diffraction limit in some other way. A widely used class of related techniques uses activated emitters to take advantage of the ability to fit a single point spread function and assign the position of the emitter to the center of the point spread function. This includes photoactivated localization microscopy (PALM), stochastic optical reconstruction microscopy (STORM), and fluorescence photoactivation localization (fPALM) [9, 10]. The general concept centers around fluorophores that are sparsely activated, such that only a few emit at any given time and can be individually localized. By repeating this activation, the localized emitters can be used to gradually build up a map of the full system. These strategies can provide spatial resolution on the order of 10 nm laterally and 20 nm axially. Limitations include the time resolution, which depends on the speed at which the emitters can be activated and deactivated to build up the map, and the necessity to attach specific fluorophores to the sample, which can preclude studying systems where that chemistry is not available.

Stimulated emission depletion (STED) microscopy takes yet another approach to achieving super-resolution by reducing the area of the excited region. To generate an image, a pulsed laser with a Gaussian profile first excites the sample [9]. Then, a second laser pulse with an annular profile and a red shifted emission interacts with the same area of the sam-

ple, stimulating emission in the outer area of the initial excitation, resulting in a trimmed excitation volume in the sample. This can be repeated in a raster scan to build up an image of the sample. STED requires that the fluorophore readily undergo stimulated emission while reducing the possibility of having the second depletion pulse excite any more of the sample, such that the emission spectrum of the fluorophore should be well red-shifted from the fluorophore's absorption spectrum. The size of the remaining excitation volume depends on the intensity of the STED depletion pulse.

1.2.3 Scanning probe techniques

Nanoscale imaging can also be achieved through scanning probe techniques that circumvent the optical diffraction limit by using a cantilever tip that interacts with the sample rather than focusing an optical probe. Atomic force microscopy (AFM) is a widely used type of nanoscale scanning probe microscopy [11]. A very thin cantilever tip, which can be as small as a single atom in width at the tip, is rastered across the surface of a sample. The cantilever tip is placed very close to or in contact with the surface of the sample, such that variations in the height of the sample cause a displacement in the cantilever position, which is detected using the change in the deflection angle of a laser beam reflected from the top of the cantilever. AFM can be used to measure changes in sample height down to 0.1 nm on a rigid sample. The lateral spatial resolution depends on the radius of the AFM cantilever tip and is commonly on the order of nanometers.

Additionally, AFM can be used to measure properties beyond the height of the sample, depending on the specific interaction between the tip and the sample and the resonance of the cantilever tip. One example is AFM phase-imaging, where the image contrast depends on the elastic interaction between the tip and the sample, which changes the phase shift offset between the driving force of the AFM tip and the tip's oscillation. For example, in block copolymers, the different polymer components can be distinguished using AFM phase-imaging [12]. Because AFM contrast depends on the interaction between the sample surface and the cantilever tip, AFM only measures the sample at the surface. In scanning probe microscopy, the time resolution is dictated by the speed at which the probe can be scanned across the sample. High speed AFM measurements at scanning rates above 100 Hz are currently possible, resulting in 1 frame per second for a 100×100 pixel image [11].

In comparison to the previously discussed optical techniques (Section 1.2.2), AFM is sensitive to a sample's mechanical properties but not to optical contrast mechanisms that provide more chemically specific information. Near-field scanning optical microscopy (NSOM) bridges this gap [13, 14]. There are several implementations of this technique, but generally they rely on using a probe to localize the light to achieve nanoscale resolution, either by using the probe to generate the excitation or facilitate light collection. NSOM is compatible with many types of optical measurements, including fluorescence measurements, infrared spectroscopy and Raman spectroscopy.

1.3 Scanning electron microscopy

Electron microscopy is another approach to nanoscale imaging where the excitation source can be focused to achieve nanoscale resolution because the wavelength of the source is small. Depending on the energy of the electrons used to probe the sample, electron microscopy typically falls under the regime of scanning electron microscopy (SEM), which uses lower energy electrons, and transmission electron microscopy (TEM), which uses higher energy electrons. Here, we will focus on SEM but will discuss TEM in the context of a comparison of the two techniques.

In SEM, a beam of electrons is focused onto the sample and raster scanned across it to build up an image. The primary electrons enter the sample and scatter multiple times, producing lower energy secondary electrons (defined as electrons with energies lower than 50 eV) and backscattered electrons [15]. In secondary electron (SE) imaging, the secondary electrons that are able to exit the material are collected by Everhart-Thornley detector placed to one side of the sample. Contrast in SE imaging is determined by the number of secondary electrons that reach the detector, which has several possible factors [15, 16]. The depth from which the secondary electrons can escape from the material is one factor, where samples with higher density or higher mean atomic weight have a lower exit depth, resulting in fewer secondary electrons escaping and a lower signal on the detector. One result of this effect is a characteristic enhancement of SE signal from the edges and corners of a sample, where the distance for secondary electrons to exit the sample is lower compared to the bulk sample and the probability for escape and subsequent detection is therefore higher. Sample topography also generates contrast in SE imaging. Taller features in a sample can block the trajectory of secondary electrons on their path to the detector, resulting in a lower detected signal from surfaces on the far side of the shadowing feature. Another possible detection geometry is InLens imaging, where a detector is placed at the pole piece (a component in the final electron focusing optic before the sample) of the SEM, directly above the sample [15]. The different collection geometry leads to different contrast compared to SE images. InLens and SE images can be collected simultaneously.

Spatial resolution in SEM is controlled by the spread of the electron beam in the material, but can be less than 1 nm [18]. This depends on the mean atomic weight and density of the material and also the energy of the primary electron beam used to probe the sample [15]. Primary beam energies range from 0.1 to 50 kV with beam energies around 10 kV commonly used. In this dissertation, we focus on experiments conducted with a low energy electron beam, ranging from 1.5 to 7 kV. The energy of the primary electron beam controls the penetration depth into the material, where higher energy primary electrons probe deeper into the material. This can be visualized using CASINO, a Monte Carlo electron scattering simulation [19] (Figure 1.1). At higher electron beam accelerating voltages, the electron beam energy is deposited further into the material and also spreads further in the lateral direction. The shape of the electron plume within the sample is controlled not only by the energy of the primary electrons but also by the mean atomic weight and density of the sample. Higher resolution SEM imaging is achieved through a smaller plume of electrons in

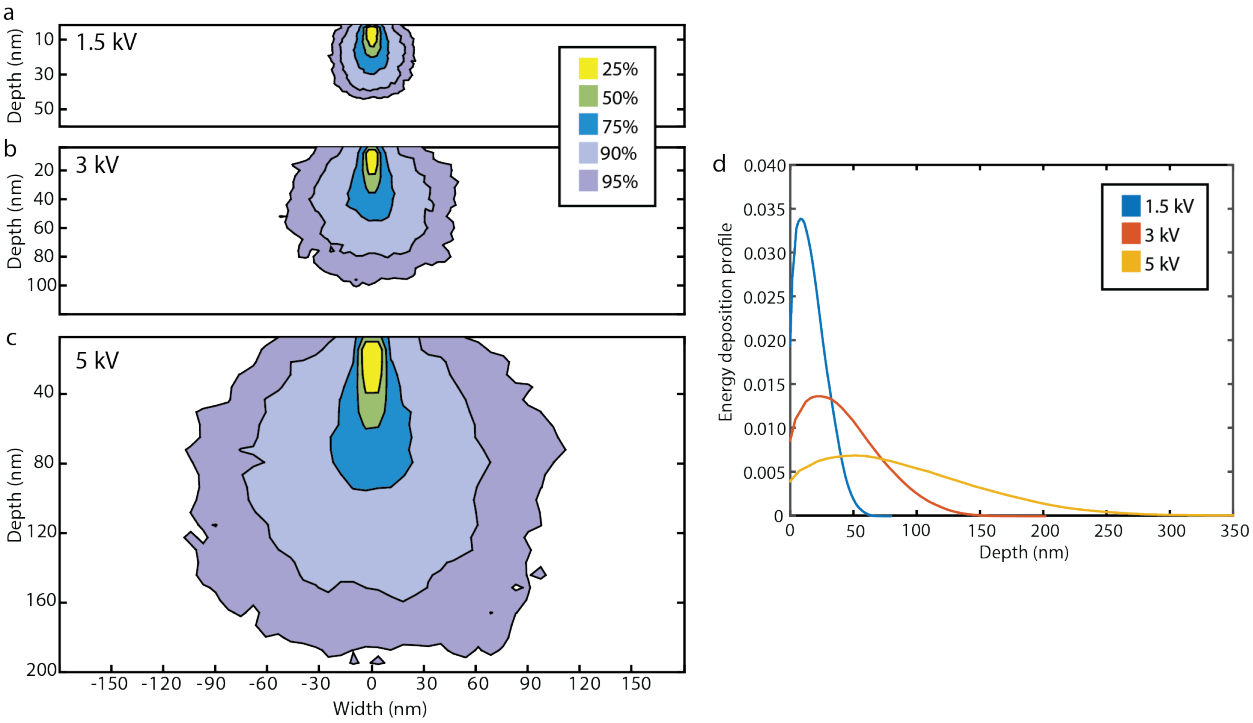

Figure 1.1: Comparison of electron beam penetration at different accelerating voltages. (a-c) Electron beam energy deposition in an example material with accelerating voltages of 1.5, 3, and 5 kV respectively. (d) Energy deposition profile of the electron beam, showing that the higher energy electron beam penetrates further into the sample. Adapted from Reference [17].

the material, which typically occurs at higher accelerating voltages and for higher sample average atomic weight and density. SEM is also capable of fast time resolution, since the only inherent limiting factor is the speed at which the electron beam can be rastered, so long as sufficient signal is collected from the sample to achieve meaningful contrast. A drawback to SEM is the possibility of sample damage caused by the high energy electrons as they scatter within the sample. In addition to the initial interaction between the primary electrons and the samples, the primary electrons will continue to scatter many times in the sample and produce even more secondary and backscattered electrons, which can also interact with the sample and cause damage.

At this point, we compare SEM to TEM. As the name suggests, transmission electron microscopy detects electrons that are transmitted through a sample to generate an image [20, 21]. To achieve transmission through a sample, the energy of an electron used in TEM is an order of magnitude higher than SEM, typically on the order of 100 to 200 kV. With these higher electron energies, TEM is capable of higher spatial resolution than SEM. Contrast

in TEM is generated by the number of electrons transmitting through the sample, which is sensitive to the thickness of the sample and the atomic number of the sample. Because TEM relies on electrons transmitting through the sample, the sample must be sufficiently thin for electrons to pass through. This is an important distinction between SEM and TEM, where SEM is capable of imaging the surface of bulk samples and TEM is limited to thin samples, on the order of 300 to 800 nm for soft materials [20]. Another important result is the difference in the electron probe energy used in SEM and TEM and the interaction of the electron probe with the sample. As previously discussed, the lower energy electrons in SEM scatter within the sample in an interaction volume. The higher energy electrons used in TEM do not scatter multiple times, resulting in a lower number of sample-electron interactions. TEM can be performed in either widefield or focused scanning (STEM) geometries, and the latter method can also be used to extract electron diffraction patterns that provide information about the sample's lattice structure [22]. When accounting for electron beam induced damage in samples, while the electron energies used in TEM are higher, the lower energy electrons used in SEM provide more interaction opportunities with the sample and therefore more possibilities for damage. While different samples are likely damaged differently by the electron beam in TEM and SEM, the higher energy electron beam used in TEM does not automatically result in more sample damage.

While SEM may not be ideal for imaging sensitive samples, imaging samples that are not entirely inorganic is possible with careful management of the electron dose budget. Compared to the other microscopies discussed, SEM imaging by itself lacks the ability to cleanly observe processes with well-defined energies, since the electron beam acts as a broadband perturbation and the detected signal is not energetically specific. For instance, this precludes the ability to select a particular signal to monitor the presence of a certain chemical species based on its emission wavelength. In contrast, TEM enables electron energy loss spectroscopy (EELS) where the energy lost by the transmitted electron in a single scattering event can be determined and used to extract detailed information about the sample [21, 23].

One example where low energy SEM imaging provides a novel perspective is in studying the dynamics of crystalline colloidal monolayers assembled at the top interface of an ionic liquid droplet [24]. Colloids are a useful model system for atomic scale processes in crystals, such as assembly, since their larger size is more experimentally accessible [25, 26]. However, for system properties or interactions that scale with size, using a model system on a size scale closer to an atomic system can provide more insight than a larger model system. In this case, nanoscale imaging enables using smaller colloidal particles compared to optical methods. The fast scanning of a SEM enables imaging dynamic processes in these colloidal assemblies, which we discuss more extensively in Chapter 4.

1.4 Cathodoluminescence microscopy

Cathodoluminescence (CL) microscopy addresses the aforementioned lack of chemical specificity available in SEM imaging. CL is the light emitted from a material after being irradiated

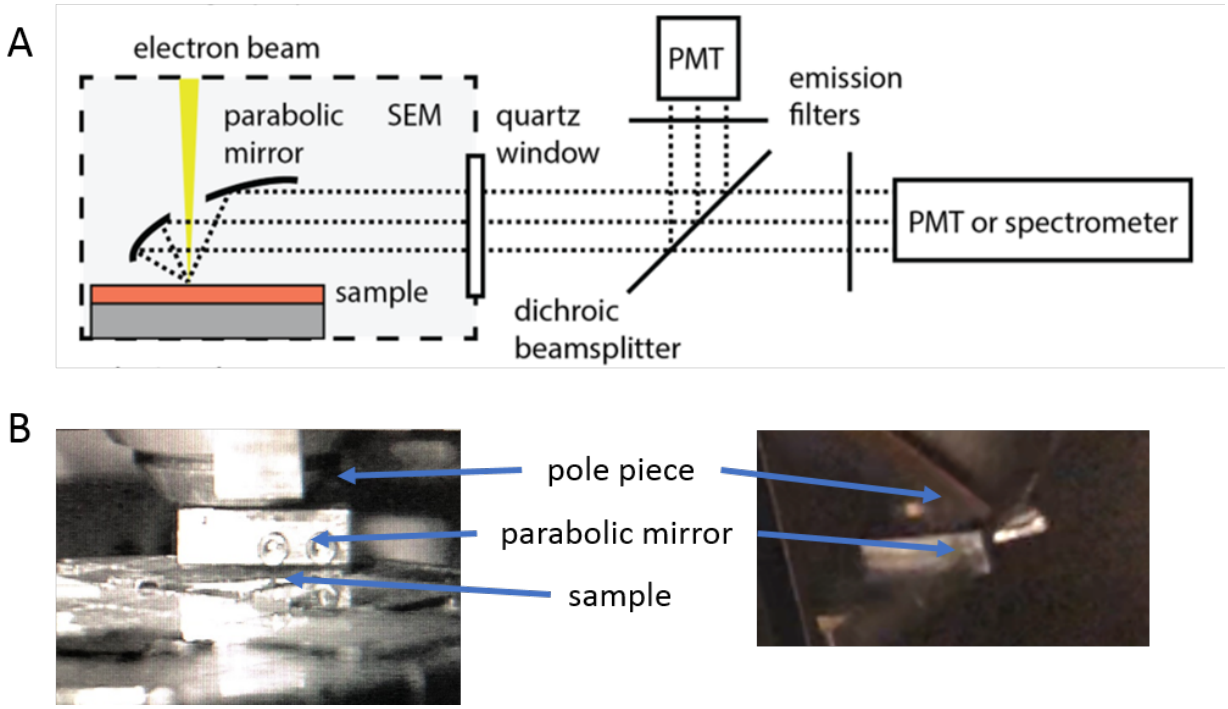

Figure 1.2: Schematic showing cathodoluminescence acquistion setup. (a) Cartoon representation of electron beam and light path. (b) Images of the experimental setup.

by electrons [27]. In CL, a small portion of the primary scattering events generate electron-hole pairs, just as a photoexcitation would but not limited to a specific excitation wavelength. CL is often comparable to fluorescence in that it involves similar relaxation from an excited to ground state energy levels in organic molecules or the recombination of an electron and hole in semiconductor materials. The wavelength of the emitted light corresponds to the energy of the associated decay process, which is defined by the physical properties of the material. In a well-defined sample, the CL wavelength can be used to uniquely identify the process from which it arose, which can then be used to determine the origin of the luminescence.

To achieve the imaging aspect of CL microscopy, a focused electron beam is rastered across the sample to excite the material and the CL signal is detected. The electron beam source is the same as in SEM or scanning TEM, where in conventional electron microscopy, the CL signal is always generated but simply not collected. In practice, CL microscopy can be viewed as an imaging modality that can be conducted in addition to conventional electron microscopy. In SEM CL, the method used in this dissertation, the electron beam inside a SEM is rastered across the sample. The emitted CL signal is collected and correlated to the position of the electron beam to build up a map of the CL emission from the sample. Specifically, the CL signal emitted from the sample is collected in the far field with a parabolic mirror placed above the sample which has a small hole to allow the electron beam to pass

through (Figure 1.2). The light is directed outside the SEM chamber and coupled into a spectrometer or separated into different wavelength channels using dichroic mirrors and collected with photomultiplier tubes (PMTs).

With this imaging setup, there are several possible ways to collect CL data. For standard CL imaging, the PMTs collect photons in different wavelength channels and the electron beam is rastered across the sample to build up an image. Here, one pixel in a CL image corresponds to the emission from the entire sample when it is excited at that position. With our current experimental setup, we can use four PMTs to achieve up to four color channels acquired simultaneously. This CL acquisition setup is exceptionally sensitive and can collect more photons than other CL acquisition geometries, rendering it capable of detecting dynamic signals non-invasively on samples that are otherwise too sensitive to electron beam exposure [28]. The other detection schemes make use of a spectrometer. The electron beam can be used as an excitation source for generating a signal to collect a CL spectrum, without preserving the spatial mapping of CL microscopy. While the CL spectrum collection is limited to the area of the sample where we efficiently collect CL photons, the large depth of field of the SEM allows us to zoom out and collect signal from a large region of the sample. This is useful for comparison with bulk photoluminescence spectra. Another possibility is to collect the CL spectrum at each pixel to create a hyperspectral map of the sample. This requires more photons than a bulk CL spectrum or typical CL imaging, where collecting over wider wavelength ranges improves contrast. Hyperspectral CL mapping is therefore most useful for very luminescent samples or samples that are very stable to the electron beam that can be imaged for longer exposure times.

An important feature of CL microscopy is the capacity for correlated image acquisition with electron microscopy. So long as the CL acquisition setup does not interfere with the electron detector, the same perturbation (the electron beam) can be used to generate an electron micrograph simultaneously with a CL image. In our current experimental setup, SE and CL images are collected simultaneously and automatically correlated (Figure 1.3, top). This correlated imaging of a sample's nanoscale topography (SE) and luminescence properties (CL) enables an understanding of how a sample's luminescence depends on the sample topography. Otherwise, correlated measurements done with separate microscopes can be difficult endeavors, typically requiring matching of different experimental requirements for each microscope and careful image registration.

Because CL microscopy uses the same electron beam perturbation as SEM, many of the considerations in spatial and temporal resolution are the same. The spatial resolution of CL and SEM are similar, where both are controlled by the lateral spread of the scattering electrons in the material (Figure 1.1). CL spatial resolution in semiconductors also depends on the diffusion length of charge carriers that recombine to emit photons. The temporal resolution of CL imaging is controlled by the time needed to acquire enough photons to generate sufficient contrast in a CL image, which varies based on the luminescence properties of the sample but can be as fast as tens of seconds per frame. Most photophysical relaxation processes occur faster than a typical pixel dwell time (μs or longer) and therefore do not limit the scanning speed. When CL emission is longer than a pixel dwell time, "streaking" can be

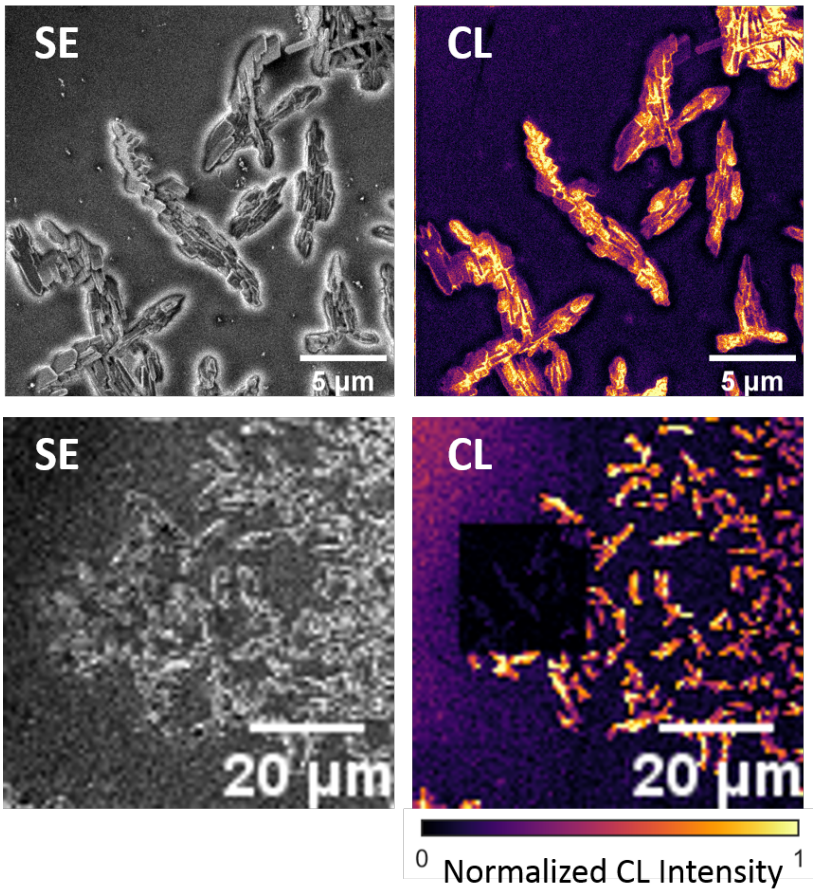

Figure 1.3: Comparison of secondary electron and cathodoluminescence images of organic semiconductor crystals. Secondary electron and cathodoluminescence images (top). Zoomed out images on same sample area, emphasizing depletion of CL signal caused by electron beam exposure during measurement of top images (bottom).

observed, where the signal from the originally excited pixel is attributed to the subsequent pixels in the raster scan pattern, leading to emission that appears as a line rather than a single point. In Chapter 2 we measure the photophysical relaxation of dopants with somewhat longer spin-forbidden transition lifetimes, where the dwell time must be carefully planned to ensure that each pixel records its own independent signature.

However, because CL microscopy still uses a focused electron beam to excite the sample, it retains the same disadvantage of SEM with respect to electron beam induced sample damage. As is the case with SEM, this is less of a drawback for primarily inorganic samples, but limits repeated imaging of organic samples. For samples with some electron beam robustness, CL microscopy is possible with careful management of the electron beam dose [17, 28, 29]. In a sample containing crystallites of the organic semiconductor rubrene, single CL images are possible (Figure 1.3, top) but the electron beam irreversibly destroys the sample luminescence (Figure 1.3, bottom). These experiments are only possible with an exceptionally sensitive CL detection scheme, which enables the collection of more photons per unit electron exposure and therefore allows us to detect enough CL before the delicate sample is irreversibly damaged.

An additional imaging modality is time resolved cathodoluminescence (TRCL) imaging. We discuss TRCL more extensively in Chapter 2, but provide a brief explanation here. TRCL imaging is analogous to fluorescence lifetime imaging (FLIM), where the luminescence lifetime at each pixel is recorded. Compared to the intensity used in normal fluorescence or CL microscopy, the lifetime of the emitter is more sensitive to changes in the local environment, which can affect the relaxation pathways to the ground state and therefore change the emitter lifetime. We implement TRCL imaging by blanking (i.e. electrostatically deflecting) the electron beam and collecting the emitted CL signal in time bins (Figure 1.4). The number of CL photons detected per time bin can be used to extract the CL lifetime of the sample excited at that pixel. By rastering the electron beam across the sample, we create a spatial map of the CL lifetime in the sample (Figure 1.4c). This is particularly useful for measuring changes in the local environment of an emitter, which could result in a larger change in CL lifetime that is more readily measured than a smaller change in CL intensity or emission wavelength. Another possible use of TRCL imaging is using the CL lifetime to select for a desired signal. For instance, in materials with a desired chromophore emission superimposed on a broader background, such as autofluorescence in biological samples, selecting time bins where the chromophore emission dominates should produce an image with improved contrast.

Direct CL microscopy still retains the interaction between the sample and the electron beam, which is unfavorable for imaging soft material samples. To address this, we have also developed cathodoluminescence imaging by resonant energy transfer (CLAIRE) as an imaging platform. It retains the advantages of CL microscopy, namely fast scanning, nanoscale resolution, and chemical specificity, but achieves better compatibility with soft materials. We discuss CLAIRE more extensively in Chapter 3, but provide a brief explanation here. In CLAIRE imaging, a thin cathodoluminescent scintillator film is placed above the sample of interest. A low energy electron beam from a SEM is focused onto the scintillator, creating a

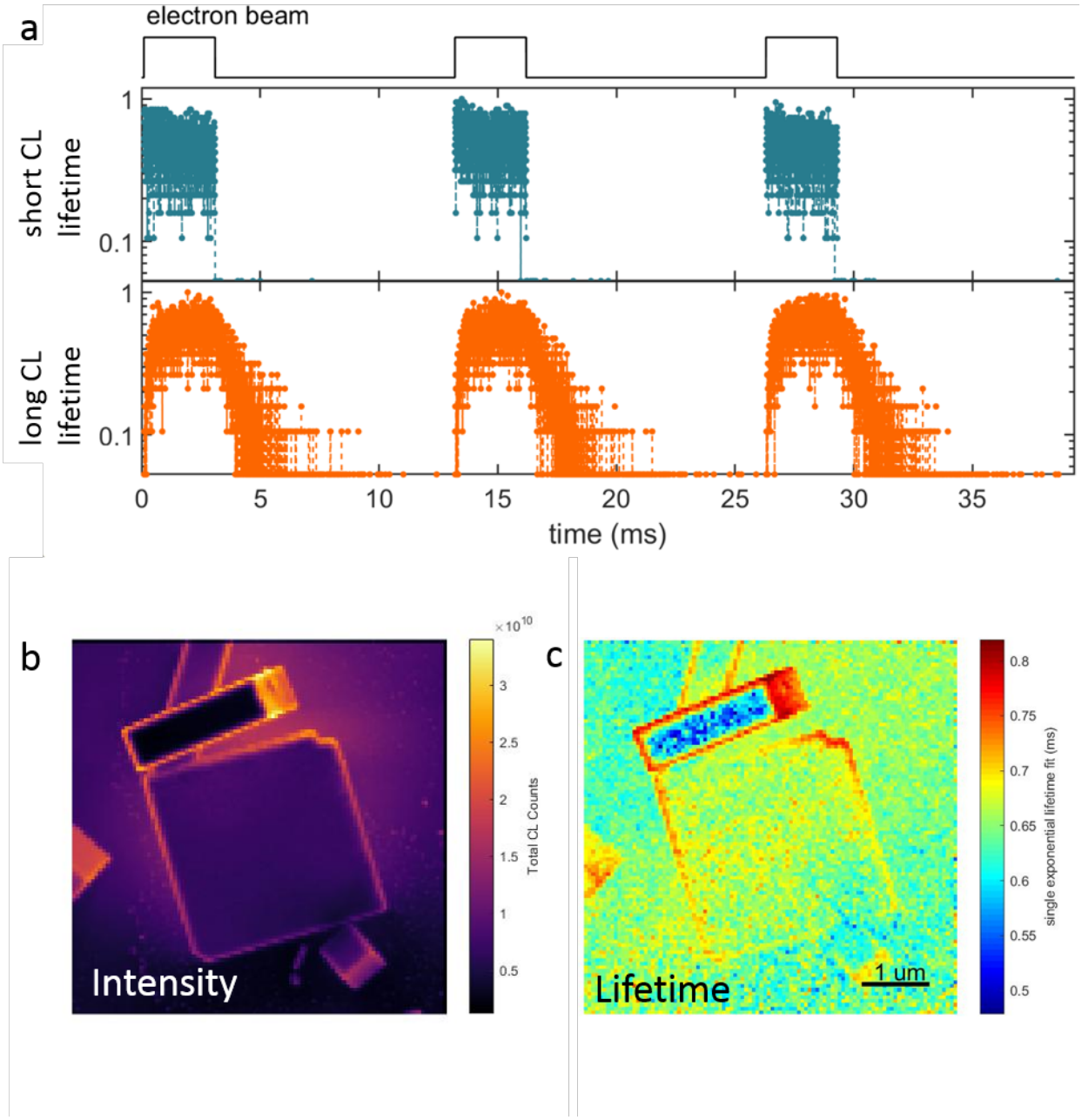

Figure 1.4: Time-resolved cathodoluminescence electron beam sequence and example images. (a) Schematic showing time-resolved cathodoluminescence electron beam sequence. (top) Electron beam duty cycle. (bottom) Example time-resolved CL emission with a short lifetime (teal) or a long lifetime (orange). (b) Example CL intensity map. (c) Corresponding example CL lifetime map.

nanoscale optical excitation source, which can then transfer energy in the near-field to the underlying sample. By rastering the electron beam across the scintillator and correlating its position with the light emitted by the underlying sample, a super-resolution image can be generated. The scintillator film greatly reduces the contact between the electron beam and the sample, minimizing damage to soft material samples. CLAIRE imaging is capable of non-invasive nanoscale imaging of soft materials with chemical specificity.

1.5 Overview of subsequent chapters

In Chapter 2, we demonstrate how time-resolved cathodoluminescence (TRCL) microscopy can be used to probe the near-surface and bulk behavior of an emissive dopant in a metal halide perovskite material. In Chapter 3, we describe our progress towards using CLAIRE microscopy to achieve super-resolution imaging of soft material samples. Finally, in Chapter 4, we return to low dose SEM imaging to characterize the dynamics of a colloidal monolayer comprised of nanoparticles in response to perturbation by the electron beam. In this case, the chemical specificity required in the previous two experiments is not necessary, and low dose SEM is sufficient. Together, these studies illustrate the versatility of SEM-based imaging and the wide range of dynamical phenomena that it can access, especially when taking care to manage the electron dose.

Chapter 2

Resolving enhanced Mn^{2+} luminescence near the surface of Mn^{2+}-doped $CsPbCl_3$ perovskite with time-resolved cathodoluminescence imaging

2.1 Introduction

Mn^{2+} is a common, highly emissive semiconductor dopant that has been extensively studied, especially recently in metal halide perovskites [30, 31]. Introducing Mn^{2+} dopants is a method for obtaining orange emission and enables simultaneous two color emission from the perovskite host matrix and the Mn^{2+} dopant (Figure 2.1a) [32–36]. In this system, Mn^{2+} substitutes for Pb^{2+} in the perovskite crystal lattice (Figure 2.1b) [33, 34, 37]. The Mn^{2+} ion provides a $^4T_1$ to $^6A_1$ transition, though its coordination and environment can alter the emissive properties. For example, Mn-Mn coupled pairs, formed at higher Mn^{2+} concentrations, alter the coordination environment and have been cited as a source for biexponential photoluminescence (PL) decay behavior in these materials [38, 39]. Intriguingly, doping has previously been used to achieve desirable perovskite properties, such as stability of the preferred crystal structure [40, 41].

While certain qualitative trends can be surmised from the literature, e.g. a red shift in the wavelength of the Mn^{2+} emission wavelength as a function of increasing Mn^{2+} concentration, quantitative inconsistencies remain [33, 36, 38, 39, 42–45]. Many studies have previously focused on the luminescence properties of ensembles of Mn^{2+} doped $CsPbCl_3$ nanocrystals synthesized using various methods [32–40, 42, 44–58]. Yet ensembles of particles often have some distribution of properties, and ensemble average measurements can obscure information about variations within the sample. For example, non-uniformity in Mn^{2+} dopant concentration or dispersity in particle size or shape within or across different ensembles is a possible source of variation in photophysical properties. Energy dispersive

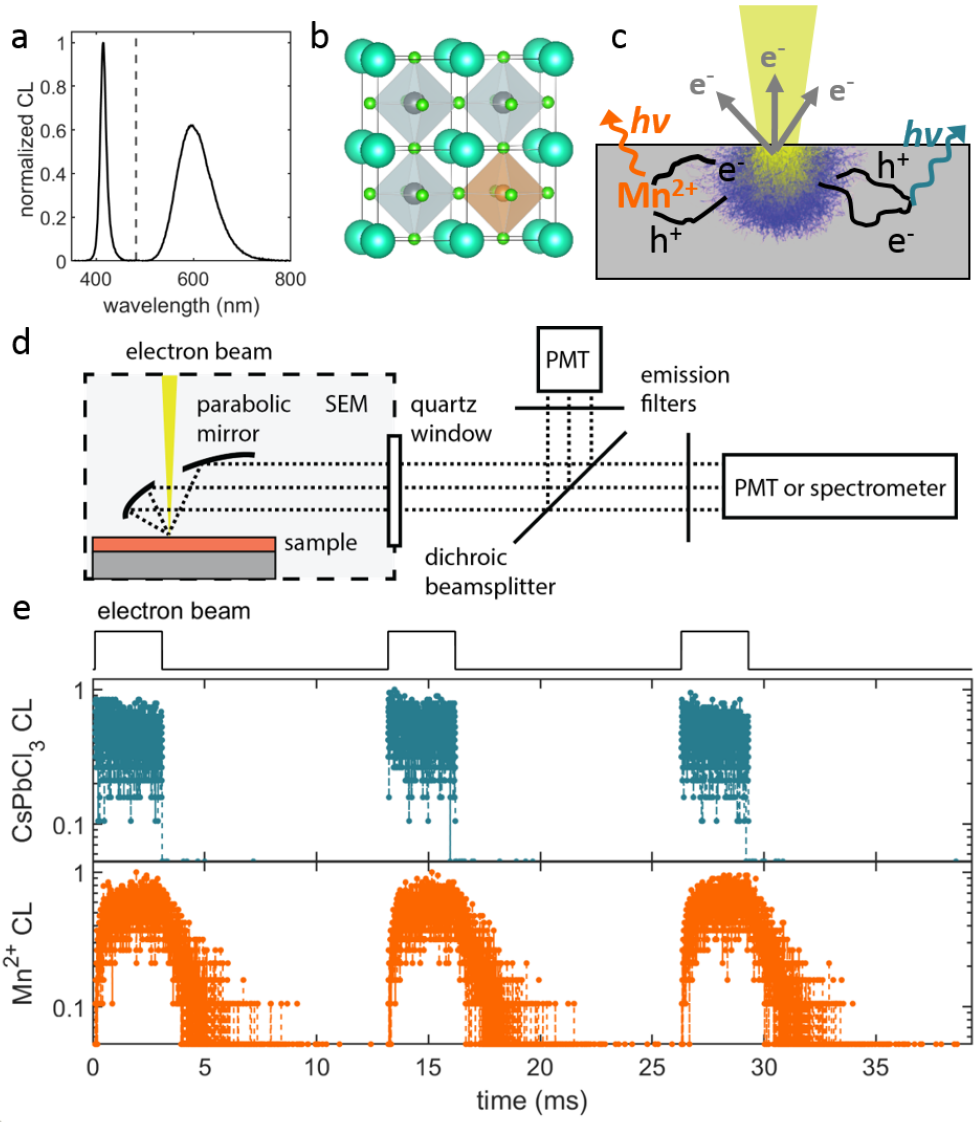

Figure 2.1: Bulk CL spectra and structure of Mn:$CsPbCl_3$ and time-resolved CL emission schematic. (a) Bulk CL spectrum of Mn^{2+} doped perovskite plates. Dotted gray line indicates filter used to separate $CsPbCl_3$ and Mn^{2+} emission. (b) Schematic showing the substitution of Mn^{2+} (orange) for Pb^{2+} (gray) in the perovskite lattice.(c) CL emission arising from the recombination of electrons and holes generated when electrons from a focused electron beam scatter within the sample. (d) CL detection apparatus. (e) Electron beam duty cycle (top) with corresponding raw CL emission from the perovskite and the Mn^{2+} dopant.

X-ray spectroscopy (EDS) can be used to spatially characterize elemental composition and has previously been used to map Mn^{2+} distributions within perovskite materials [36, 37]. The presence of Mn^{2+} alone, however, does not report on spatial variations in Mn^{2+} decay dynamics nor does the local concentration of Mn^{2+} obtained by EDS provide the concomitant spatial variation of Mn^{2+} luminescence properties. Ideally, to identify concentration, environment, and luminescence variations in Mn^{2+} doped perovskites, a combination of EDS and spatially resolved luminescence would be required.

2.2 Time-resolved cathodoluminescence microscopy

Here, we use the capabilities of time resolved cathodoluminescence (TRCL) imaging in combination with EDS to achieve a more detailed and spatially-resolved understanding of the photophysical behavior of the Mn^{2+} dopant. Photoluminescence (PL) lifetimes are commonly used to detect small changes in the local environment of a luminescent species [59]. Fluorescence lifetime imaging (FLIM) combines the lifetime information with spatial resolution [60, 61]. While valuable, optical diffraction-limited measurements make comparing surface and bulk properties a challenge. In CL, a focused electron beam in a SEM generates electron and hole pairs that can radiatively recombine to produce luminescence (Figure 2.1c). To create an image, the electron beam is rastered across the sample, and the emitted light is collected in the far-field (Figure 2.1d), building up a spatial map in which each pixel value represents the luminescence due to the electron beam excitation of the sample. CL imaging has previously been used to measure spatially varying chemical composition of perovskite materials, including in halide demixing, dopant incorporation, and enhanced edge emission [28, 29, 62, 63]. In other materials, CL has been used to identify regions of enhanced emission efficiency [64]. CL imaging provides superior, typically nanoscale, spatial resolution (a convolution of electron beam generation volume and sample-specific carrier diffusion length) and correlated secondary electron (SE) and CL images. These aspects of CL imaging are highly advantageous, yet CL images alone do not contain luminescence lifetime information.

Fortunately, time-resolved CL acquisition is also possible for photophysical characterization of luminescent samples and has previously been performed in perovskites [65–67]. We therefore use TRCL imaging to spatially characterize the Mn^{2+} dopant's emission at high spatial resolution. Unlike CL intensity imaging alone, we show that TRCL imaging is able to resolve variations in luminescence lifetime to report on variations in electronic structure or environment more sensitively than the spectral shift of the characteristically broad Mn^{2+} emission peak. Like FLIM, TRCL imaging proved also to be robust to many intensity-based imaging artifacts, potentially including geometry-associated changes in excitation density, photon escape probability, or acquisition geometry, which could affect the total intensity but not the relative contribution to the overall lifetime.

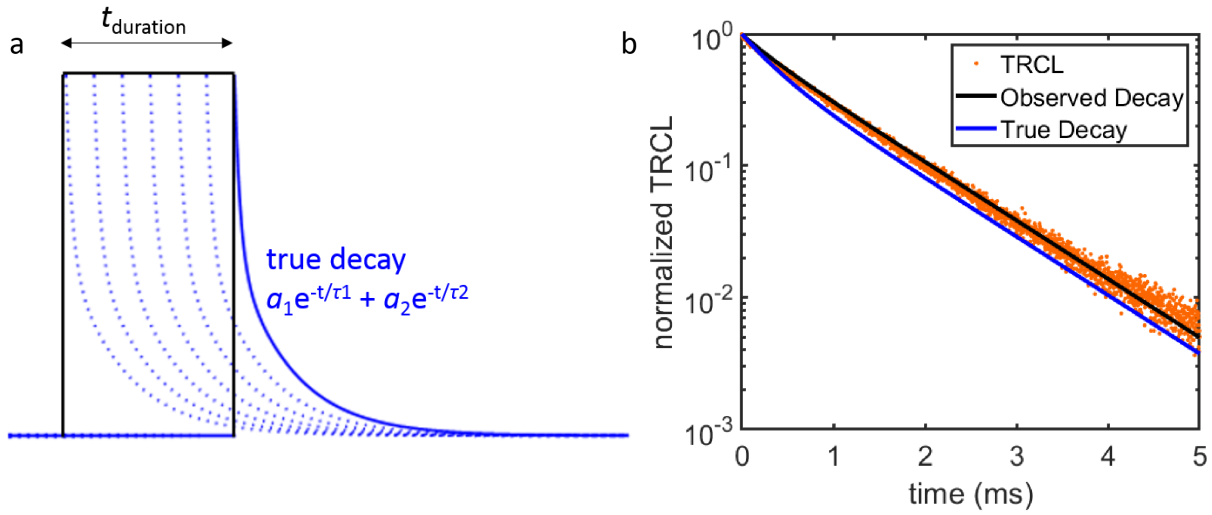

Figure 2.2: Depiction of TRCL deconvolution. (a) Visualization of buildup of multiple "true" decay curves (blue) during a finite duration excitation (black). (b) Comparison of TRCL data (orange) with observed decay (black) and deconvolved decay (blue).

2.2.1 Time-resolved cathodoluminescence microscopy implementation

To acquire TRCL images, CL lifetime acquisition is implemented via electronic beam blanking using a Raith electrostatic beam blanker and by collecting emitted light in time bins on a data acquisition card [68]. The data acquisition card (National Instruments) is controlled by a home-built adaptation of ScopeFoundry, the control/acquisition software platform at the Molecular Foundry [68]. All SE and CL images were collected with an accelerating voltage of 3.0 kV and a beam current of 200 pA, using a 482 nm dichroic filter (indicated by the gray line in Figure 2.1a) and a subsequent 500 nm long pass filter to separate the CL color channels corresponding to $CsPbCl_3$ and Mn^{2+}, respectively.

Because the Mn^{2+} transition is forbidden, the anticipated lifetime is on the order of a ms. Data are collected at a single pixel, ranging in size from 85 to 165 nm, by exciting the corresponding region for 3.0 to 3.5 ms before blanking the beam for a 10 ms acquisition time, after which the beam is moved to the next pixel. CL photons are collected for the full duration of an experiment (Figure 2.1e), binned in 2 μs intervals, and analyzed in distinct ways. First, a CL *intensity* image can be generated simultaneously by integrating all photons emitted pixel by pixel. For *TRCL* imaging, however, the data acquired when the beam is blanked are normalized, fit to two exponential decays, and deconvolved from the effects of the finite-duration excitation as described in Section 2.2.2.

2.2.2 Deconvolution for non-impulsive excitation effects

The non-impulsive excitation used in this implementation of TRCL has a significant effect on the observed decay. To extract meaningful fitting parameters, the decay and the excitation need to be decoupled. The observed decay is a convolution of the spread of excitation times and the true decay. Because the contribution from components with longer lifetimes persists for a longer time, the observed decay has a greater contribution from the long lifetime components. By treating the observed decay as a number of "true" decay curves with the lifetimes τ_1 and τ_2 and corresponding amplitudes $a_{1,true}$ and $a_{2,true}$, offset by infinitesimal excitation times until the full excitation is complete ($t_{duration}$), the expression for the observed decay can be solved by integrating over the duration of the excitation time (Figure 2.2a). The resulting expression for the observed decay, $a_{1,true}\tau_1(1-e^{-t_{duration}/\tau_1})\times e^{-t/\tau_1}+a_{2,true}\tau_2(1-e^{-t_{duration}/\tau_2})\times e^{-t/\tau_2}$, shows that the observed decay has the same lifetimes, τ_1 and τ_2, as the true decay. The difference between the observed decay and the true decay is the observed amplitudes, $a_{1,obs}$ and $a_{2,obs}$, which are weighted by the corresponding lifetimes, τ_1 and τ_2 and the finite duration of the excitation, $t_{duration}$. The CL lifetime decays (orange) are fitted directly to the expression for the observed decay (black) and the extracted parameters $a_{1,true}$, $a_{2,true}$, τ_1, and τ_2 are used to plot the true CL decay (blue), $a_{1,true}\times e^{-t/\tau_1}+a_{2,true}\times e^{-t/\tau_2}$ (Figure 2.2b). To achieve a better fit, CL decays are normalized to the highest value, fitted to the observed decay expression, and amplitudes $a_{1,true}$ and $a_{2,true}$ are subsequently corrected through multiplication by the normalization factor.

Error bars in the lifetime contribution (Figure 2.4g) and the lifetime (Figure 2.7) barplots indicate the standard deviation in data from six different microplates. This error representation was chosen because the variation between samples was more significant than other sources of error (e.g. error from fitting the CL decay data). The metal halide perovskite plates likely had slightly different defect densities, supported by the observation that the perovskite CL emission was not necessarily homogeneous even within a given plate (Figure 2.4b). This heterogeneity in the perovskite lattice could directly affect the environment of the Mn^{2+} dopant and therefore its lifetime. Additionally, the CL data was recorded at somewhat different magnifications for each sample, so exact width of a bright edge pixel varies from sample to sample. Therefore, an edge pixel for a given sample could have slightly different amounts of near-surface and bulk contributions, which could affect the measured short lifetime contribution.

2.3 Mn^{2+} doped $CsPbCl_3$ characterization

2.3.1 Synthesis and bulk characterization of Mn^{2+} doped $CsPbCl_3$

In this study, we focused on Mn^{2+} doped $CsPbCl_3$ microplates. To make the microplates, lead (III) acetate trihydrate (0.46 g/mL) in dimethylformamide was filtered to remove undissolved reagent and spincoated onto the substrate at 5000 rpm for 1 minute. The substrate was heated at 130 °C for 60 minutes to evaporate excess solvent, allowed to cool to room

temperature, and immersed in a solution of 20 mg/mL $MnCl_2 \cdot 4H_2O$ and 120 mg/mL CsCl in methanol for 30 minutes. The substrate was removed from the solution, the final product was rinsed thoroughly with isopropyl alcohol to remove excess reagents and was dried with N_2 gas. The microplates produced with this method had persistent rectangular shapes consistent with the possible orthorhombic, tetragonal or cubic structure of $CsPbCl_3$ perovskite (Figure 2.1b) [30]. Although we did not explicitly measure the structure, the rectangular prism structure of the microplates could arise due to crystal formation on the substrate proceeding in both in-plane directions while only occurring in a single out-of-plane direction.

Scanning transmission electron microscope (STEM) EDS characterization in the Minor lab shows 1 atom % Mn^{2+} doping with 22% Cs, 17% Pb and 60% Cl, consistent with the expected stoichiometry for $CsPbCl_3$. To perform CL spectral acquisition, a fiber was used to couple the CL signal to a QE65PRO spectrometer with a HC1-QE grating (Ocean Optics). The bulk CL emission spectrum of the microplates shows emission from the $CsPbCl_3$ band edge emission at 415 nm and broad emission from Mn^{2+} centered at around 595 nm (Figure 2.1a).

To mimic the TRCL protocol, photoluminescence lifetimes were acquired with a Picoquant FluoTime 300 fluorimeter using pulsed 408 nm wavelength excitation at 40 MHz for 1 ms before acquiring for 4 ms. Mn^{2+} emission was detected from 595 to 605 nm. The bulk PL decay dynamics (Figure 2.3) of the microplates are consistent with reported ensemble average properties of nanocrystal Mn:$CsPbCl_3$ [32, 34–36, 38, 48]. The bulk Mn^{2+} decay fits to a biexponential decay with lifetimes of 0.22 ms and 0.74 ms with the deconvolution method described in Section 2.2.2. While these time constants are consistent with the literature [35], there is a finite probability that the sample does not fully relax to the ground state during the 4 ms between 1 ms excitation periods. The longer lifetime component (0.74 ms) is likely somewhat shorter than that measured in TRCL (around 1 ms) because of this effect. Whereas in TRCL a single repetition of the beam on/beam off cycle is employed for a given pixel, the bulk PL measurement repeatedly excites and measures the same volume.

2.3.2 CL Intensity Mapping of Mn doped $CsPbCl_3$

Even before analyzing TRCL data, the CL intensity images, generated by integrating the photons emitted from the sample irrespective of the time of emission, show intriguing results. First, we observe mostly spatially homogeneous perovskite emission intensity. The small increase of the signal at the edge (Figure 2.4 b,e) mimics the SE signal (Figure 2.4 a,e) and can be attributed to edge effects that are well-known in electron microscopy. In comparison, the intensity of the Mn^{2+} CL image is approximately two to ten times greater at the edge than the middle region of the perovskite microplates (Figure 2.4 c,e). The increased edge Mn^{2+} CL intensity is reproducible across more than thirty samples.

To readily compare the edge and middle region of the microplates, we sequentially threshold, segment, and aggregate the data separately for each of these two regions (Figure 2.4d). The edge pixels of a Mn:$CsPbCl_3$ plate were identified in the Mn^{2+} CL image as having a higher total intensity. To identify these regions of interest (ROIs), a local Bernsen thresh-

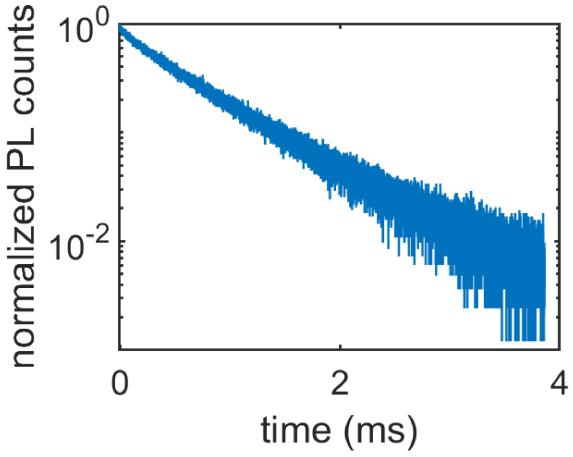

Figure 2.3: Mn^{2+} PL decay in bulk $Mn:CsPbCl_3$

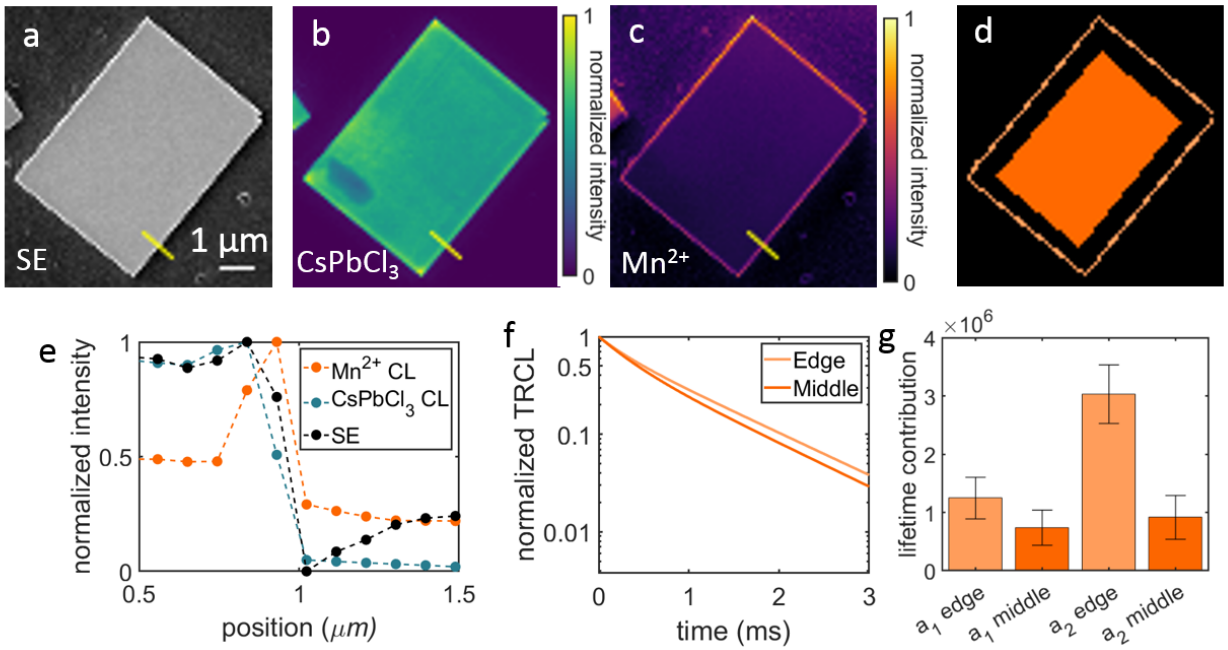

Figure 2.4: CL imaging and TRCL plots of $Mn:CsPbCl_3$ plates. (a, b, c) Characteristic perovskite SE and CL images. (d) Segmented Mn^{2+} CL image showing the edge (pale orange) and middle (orange) regions. (e) Linecuts across the yellow line show the pronounced change in Mn^{2+} intensity compared to the $CsPbCl_3$ intensity or SE signal. (f) Deconvolved TRCL decay shows different decay behavior between edge and middle. (g) A bar plot of the fitted TRCL amplitudes for each lifetime.

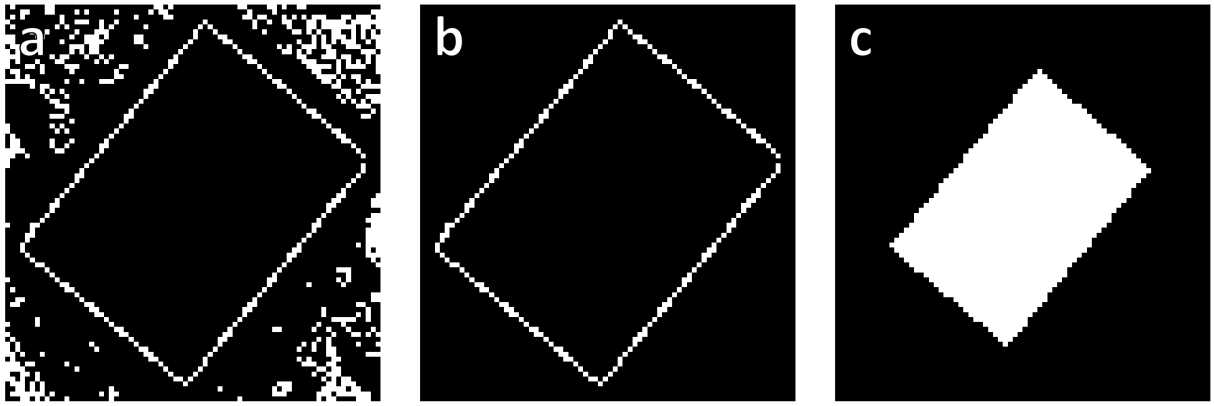

Figure 2.5: Example thesholding analysis for Mn:$CsPbCl_3$ plates. (a) Binarized raw data. (b) Edge determined by removal of non-contiguous pixels. (c) Manually selected center region.

olding method was implemented in ImageJ (Figure 2.5a) [69]. Areas not contiguous with the plate edge were removed manually to isolate the plate edge region shown in Figure 2.5b. The middle region ROI was manually chosen to maintain a border a distance of several pixels from the edge (Figure 2.5c).

Using STEM-EDS to perform elemental mapping, we find that the concentration of Mn^{2+} is uniform across the microplate to within the spatial resolution and sensitivity of the measurement (Figure 2.6g). EDS measurements were performed at 60 kV using a FEI TitanX equipped with a SuperX EDS detector. Line-cut profiles of the Mn Kα peak show sharp plate boundaries with no concentration enhancement along the plate edges (Figure 2.6 h,i). This result suggests that the enhanced CL intensity at the edges is not caused by a local increase in the Mn^{2+} concentration.

2.4 Using TRCL imaging to identify two different Mn^{2+} dopant populations

TRCL imaging provides more insight into the increase in Mn^{2+} emission intensity at the microplate edges. In the Mn^{2+} TRCL, we observe a biexponential decay of the form $I(t) = a_1 \times e^{-t/\tau_1} + a_2 \times e^{-t/\tau_2}$. The biexponential decay is present in both edge and middle regions with the same time constants, $\tau_1 = 0.2$ ms and $\tau_2 = 1$ ms (Figures 2.4f, 2.7). The most significant difference between the edge and the middle is that a_2, the contribution of the longer lifetime component, is approximately three-fold higher at the edge (Figure 2.4g). In comparison, a_1, the contribution from the short lifetime component, differs very little between the edge and middle. The increase in a_2 manifests as a longer average lifetime

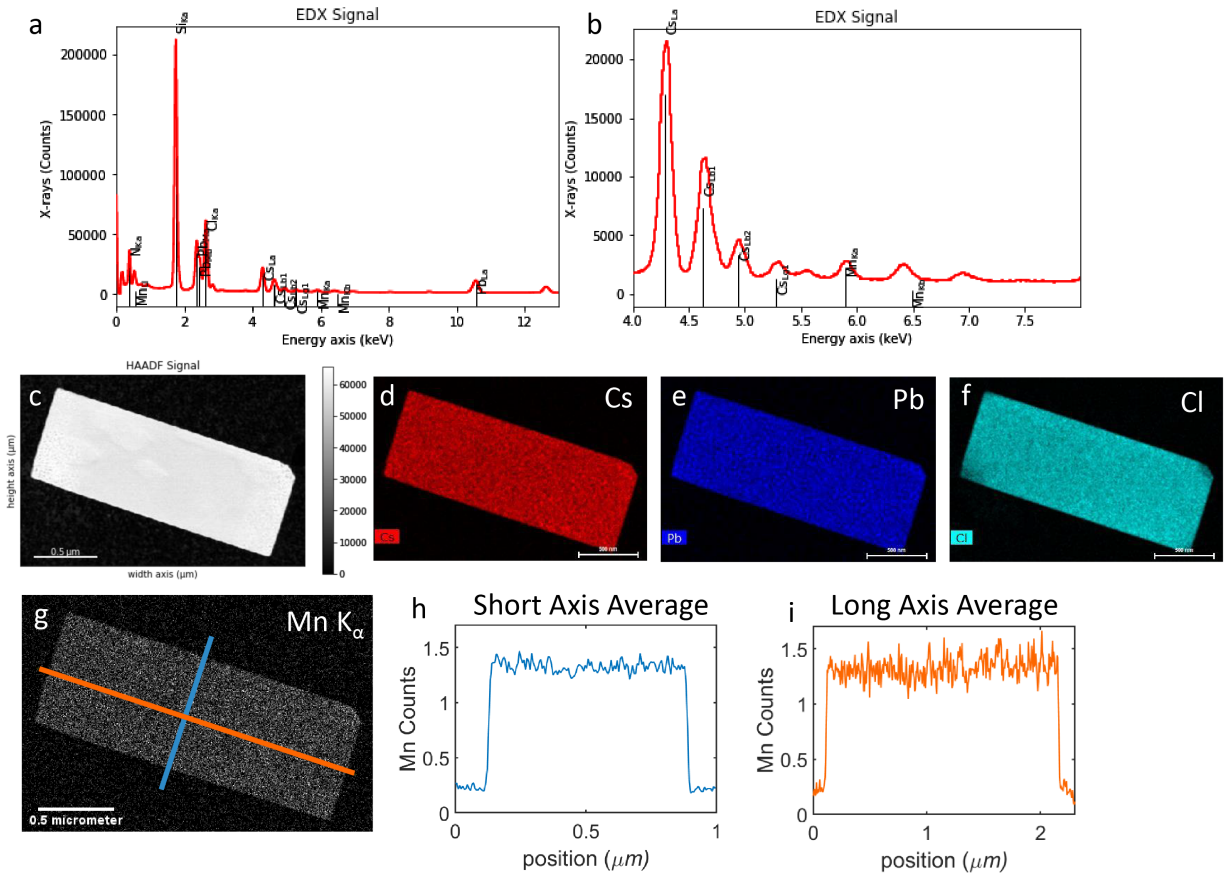

Figure 2.6: EDS spectra and chemical composition maps of a Mn:$CsPbCl_3$ plate. (a,b) EDS spectra (c) A high-angle annular dark-field image shows the plate. (d,e,f,g) Elemental maps of Cs, Pb, Cl, and Mn respectively. (h,i) Line-cut profiles of the Mn Kα peak along the short and long axis, respectively, corresponding to lines drawn in (g).

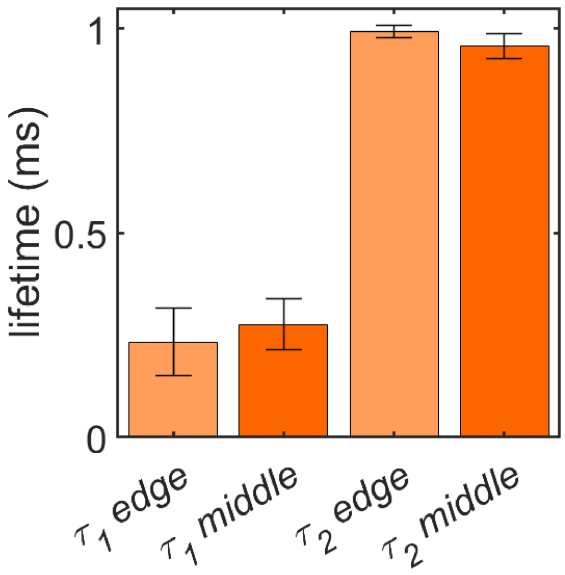

Figure 2.7: Barplot of fitted lifetime of Mn:$CsPbCl_3$ plates at different ROIs. Neither lifetime τ_1 or τ_2 changes significantly between the edge and middle. Error bars indicate the standard deviation of the lifetimes averaged over data from six different plates.

and is consistent with a higher total number of emitted photons at the edge (Figure 2.4 c,f). Because the CL experiment probes a finite generation volume (Figure 2.1c), measurements at each of the middle and edge regions both contain some combination of near-surface and bulk material contributions. The edge of perovskite microplates has a higher contribution from the near-surface region due to the inclusion of both the top and side faces, so we attribute the larger value of a_2 at the edge to an even larger value of a_2 in the near-surface region.

Explaining this difference in TRCL requires developing a hypothesis for why the TRCL of the microplates exhibits a biexponential decay and why a_2 differs between the edge and middle of the microplate while a_1, τ_1 and τ_2 are the same in both regions. The explanation that is most consistent with a differing a_2 and uniform a_1 is the presence of two different Mn^{2+} populations that each independently contribute to the overall signal, with their own respective lifetimes, τ_1 and τ_2. We associate one population with τ_1 and the other with τ_2. Because both lifetimes of the Mn^{2+} luminescence are several orders of magnitude longer than the timescales associated with perovskite radiative recombination, self-absorption and reemission, trapping, or energy transfer, each of the two different Mn^{2+} lifetimes is most likely caused by a distinct property that is directly associated with the Mn^{2+} ions and their surroundings. In addition, self-absorption by the dopant is symmetry forbidden and therefore unlikely, and the emission from the dopant is sufficiently red-shifted that reabsorption by the perovskite host is unlikely (Figure 2.1a). To assign the independent populations, we compare

the two lifetimes. The longer lifetime τ_2 is likely due to a less perturbed, intrinsic Mn^{2+} d–d transition, heretofore labeled Mn^{2+}_{Intr}, which is virtually symmetry forbidden. This assignment is consistent with the Mn^{2+} lifetime previously observed in Mn:$CsPbCl_3$ nanocrystals [32, 34–36, 38, 49]. We suggest that τ_1 is shorter because it arises from a distortion to the Mn^{2+} symmetry environment, and heretofore call this population Mn^{2+}_{Dist}. Such a distortion to the Mn^{2+} would decrease the intrinsic octahedral symmetry, which would also decrease the "forbidden" nature of the transition. Biexponential decays in Mn:$CsPbCl_3$ have been previously measured in PL and were suggested to be caused by the presence of Mn-Mn coupled pairs [39], surface-exposed Mn^{2+} [49], or other trap states [38]. Surface-exposed Mn^{2+} is unlikely to contribute greatly to the overall TRCL signal, since the volume probed in the CL experiment would geometrically contain only a small contribution from the atomic layer at the surface, so Mn-Mn coupled pairs or other trap states would be more likely sources of Mn^{2+}_{Dist}. In summary, we propose that a Mn^{2+}_{Dist} population in some distorted environment contributing a signal with amplitude $a_1 = a_{Dist}$ is responsible for the lifetime $\tau_1 = \tau_{Dist}$ and that a Mn^{2+}_{Intr} population in the intrinsic symmetric environment contributes a signal with amplitude $a_2 = a_{Intr}$ and is responsible for the lifetime $\tau_2 = \tau_{Intr}$.

To explain the three-fold increase in the excited population of Mn^{2+}_{Intr} between the edge and middle while the excited state population of Mn^{2+}_{Dist} remains constant, we consider the excitation mechanism of CL. The electrons from the electron beam scatter within the material, generating electrons and holes that diffuse and undergo radiative recombination to emit a photon. Mn^{2+}_{Intr} luminescence necessarily requires the encounter of an electron and a hole at a Mn^{2+}_{Intr} site. While most treatments of this process describe excitonic energy transfer from the perovskite to the Mn^{2+}, this has been demonstrated in the more commonly studied nanoparticle form factor, where charge carrier confinement is possible. We speculate that, due to the low exciton binding energy in bulk microplates, the charge carriers can instead arrive independently on the Mn^{2+} center. This encounter could be made more probable if charge carriers could be preferentially localized near Mn^{2+} ions. One possible way that this could occur is for a charge carrier to spend more time near a Mn^{2+} site, for instance due to a proximal trap site, such as a halide vacancy. If the concentration of such traps were to increase with proximity to the plate surface then the probability of recombination at Mn^{2+} dopants could also increase, in turn increasing the excited state population, a_2, near the plate surface (Figure 2.8). In the bulk, a lower trap density would determine a lower baseline probability that a trap and a Mn^{2+} were within a distance small enough to enhance recombination on Mn^{2+}. This reasoning is supported by bulk PL measurements on nano- and microcrystals of Mn^{2+} doped $CsPbCl_3$ that identify a trap-assisted mechanism for energy transfer from the perovskite to the Mn^{2+} [57, 58, 70, 71]. Importantly, the region near halide perovskite surfaces can be complex, with different properties than the bulk material. Thus, other near-surface associated behaviors of the perovskite could also plausibly lead to more efficient electron-hole recombination on the Mn^{2+}. Consistent with the assignment of a_1 to the Mn^{2+}_{Dist} population, the unchanging value for a_1 at edge and middle could be explained in the case that the number of available Mn-Mn pairs or of other features that reduce octahedral symmetry of the Mn^{2+} were much smaller than the number of electrons

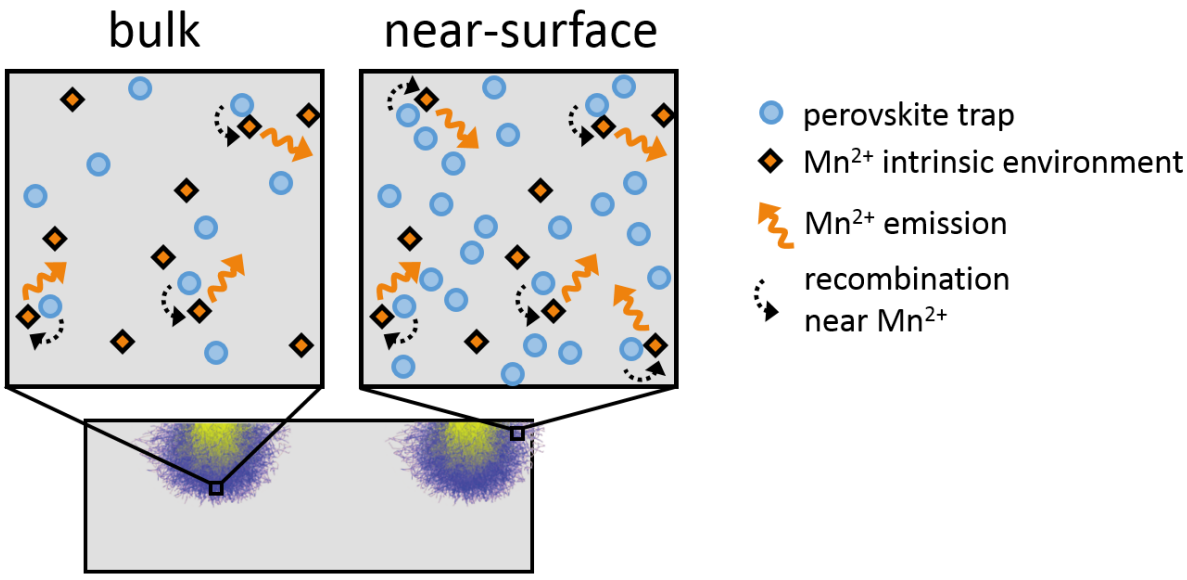

Figure 2.8: Diagram of proposed model for the observed differences between bulk and near-surface Mn^{2+}. Mn^{2+} dopants (orange diamonds) are present at constant concentration while perovskite traps (blue circles), which are present at varying concentrations, control the relative proportion of Mn^{2+} emission.

and holes available to excite them.

2.5 Conclusions and outlook

There are two key features of the experimental design that enabled the above findings—the combination of TRCL imaging and the microplate sample geometry. TRCL, as compared to CL intensity alone, gives access to a high spatial resolution photophysical map, which here allows us to distinguish the detailed nature of the difference in CL intensity between edge and middle of the Mn-doped perovskite material. The microplate sample geometry, combined with the spatial context that imaging provides, enables us to furthermore distinguish near-surface and bulk contributions to the CL signal, which would not have been possible for much smaller nanocrystals nor in ensemble averaged measurements.

Given the hypothesis that defects, which are more prominent near the surface of the microplate, could be implicated in the enhanced luminescence found at the edges of the material, an interesting consequence to note is that defects could play a positive, rather than negative, role in improving luminescence of Mn^{2+} doped perovskites. In particular, this idea suggests that if Mn^{2+} emission is the desired outcome of doping, then nanocrystals would be an optimal functional geometry, given their high surface to volume ratio. In spite

of this finding, TRCL imaging on a material form factor different from that of a nanocrystal was required to elucidate this result.

Overall, we have used TRCL imaging as a powerful method for interpreting local variations in dopant decay behavior within the context of the full sample. Specifically, this experiment has shown that TRCL imaging is capable of resolving spatial variations in recombination efficiency, which we suggest are caused by a larger surface trap density in Mn^{2+}-doped metal halide perovskites. There are many parameters that impact the emissive behavior of dopants in perovskites, not all of which are well understood or characterized. To further characterize dopant emission we have shown that lifetime measurements on the nanoscale are an extremely sensitive way to identify changes in luminescence decay caused by variations in the dopant's local environment and facilitate a more incisive interpretation than changes in emission intensity alone. TRCL imaging has the advantage of superior spatial resolution as compared to time-resolved PL imaging (FLIM) and the ability to simultaneously acquire correlated topographical information via secondary electron scattering. In the future, TRCL imaging could be useful more generally to explain the underlying source of non-spatially uniform behavior in other exciting materials, such as diamond and silicon carbide that contain defect centers used as single photon quantum emitters [72, 73].

Chapter 3

Cathodoluminescence Imaging by Resonant Energy Transfer (CLAIRE)

3.1 Introduction

Cathodoluminescence (CL) microscopy is a powerful technique for generating nanoscale images with correlated luminescence and microstructure information. However, many soft materials are susceptible to damage induced by the high energy electron beam and are therefore incompatible with CL microscopy, even with efforts to reduce electron exposure and optimize photon collection. Additionally, capturing dynamic processes in these materials requires imaging samples for an extended period of time with repeated electron beam exposure. Even when the sample's damage threshold may permit a single CL image, this limitation precludes using CL microscopy to study dynamics in soft materials.

Another approach for capturing high resolution images of complex samples is super-resolution optical microscopy. Super-resolution optical microscopy methods have enabled high-resolution fluorescence imaging of complex biological systems with chemical specificity [9]. However, due to limitations in time resolution, established super-resolution microscopy techniques often do not have the capability of observing dynamics at the nanoscale. Additionally, super-resolution techniques often require labeling with specialized fluorophores with photophysical properties specifically optimized for the experiment and often cannot take advantage of a sample's endogenous chromophores [10].

Our research group developed a super-resolution imaging platform that addresses these limitations, called cathodoluminescence-activated imaging by resonant energy transfer (CLAIRE). Specifically, CLAIRE imaging aims to combine the fast acquisition rates and nanoscale resolution of scanning electron microscopy with the chemical specificity and non-invasive nature of fluorescence microscopy.

In CLAIRE imaging, a thin cathodoluminescent scintillator film is placed between the sample of interest and the electron beam of a scanning electron microscope (SEM) (Figure 3.1). A scintillator is a material that emits lights when electrons impinge on it. A low energy

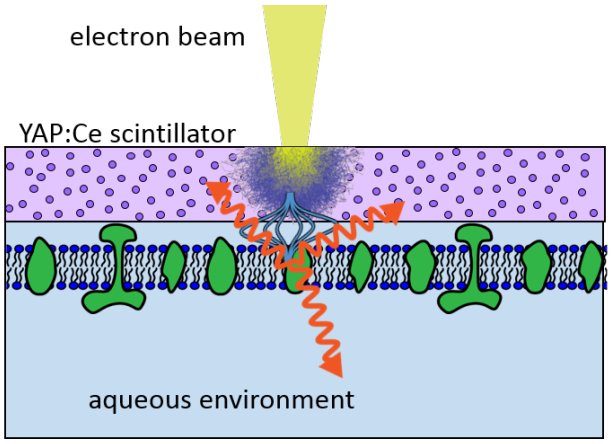

Figure 3.1: CLAIRE schematic

electron beam from the SEM is focused onto the scintillator, creating a nanoscale optical excitation source, which can then transfer energy in the near-field to the underlying sample. By rastering the electron beam across the scintillator and correlating its position with the light emitted by the scintillator and by the underlying sample, a super-resolution image can be generated. The scintillator film prevents the electron beam from making direct contact with the sample, making this technique more suitable for samples prone to electron beam damage, like soft materials.

Additionally, the scintillator acts as a barrier between the vacuum environment of the SEM and the sample environment, allowing for the sample to remain in its native environment. This is particularly appealing for biological materials, which often require an aqueous environment.

Previous work demonstrated the super-resolution capabilities of CLAIRE microscopy on static samples [74]. With metal nanostructures deposited on the CLAIRE scintillator, enhancement of the scintillator emission was observed with 46 nm lateral spatial resolution. CLAIRE microscopy was also tested on a blend of fluorescent polymers, which would be damaged by direct electron beam exposure. CLAIRE microscopy was able to distinguish the two components of the fluorescent polymer blend with a spatial resolution of 68 nm, demonstrating that CLAIRE is capable of super-resolution imaging on soft material samples. Another important previous advance was the development of the lithographic process to fabricate CLAIRE imaging chips that were capable of supporting free-standing scintillator films, first described in print in the work presented in Section 3.4 [74]. Prior experiments depended on using samples that functioned as scintillator support, and free-standing scintillator films greatly expanded the range of samples that could be used with CLAIRE microscopy, paving the way for the experiments discussed in Section 3.4.

3.2 CLAIRE scintillator growth with pulsed laser deposition

3.2.1 CLAIRE scintillator thin film requirements

The success of CLAIRE imaging depends strongly on the properties of the scintillator being used. In addition to satisfying the condition of overlapping scintillator emission and sample absorption, other scintillator properties are important for optimizing the signal of a CLAIRE experiment. For the scintillator that we consider here, the emission comes from dopants in the host material that behave as point emitters. A highly emissive scintillator will yield more photons, enabling either better contrast or shorter pixel dwell times needed to achieve the necessary contrast, giving rise to better spatial or temporal resolution, respectively. Faster emitter lifetimes enable the emitter to cycle more times during the pixel dwell time, leading to overall more emitted photons. For clarity in interpreting CLAIRE images, the scintillator must also be uniformly bright so that variations in scintillator or sample brightness can be unambiguously attributed to some change in the sample. For the scintillator to be uniformly bright, the emissive dopant must be uniformly distributed in the scintillator. The scintillator must also be uniformly flat to decouple changes in contrast due to scintillator topography from changes in contrast due to actual sample differences, because near-field interactions depend on the distance between the sample and the emitters in the scintillator. One example is Förster resonant energy transfer (FRET), which scales with $1/r^6$ distance between the donor (scintillator) and acceptor (sample chromophore) and is sensitive to changes on the order of nanometers [75].

3.2.2 Pulsed Laser Deposition of YAP:Ce

The scintillator material that we use for CLAIRE experiments is $YAlO_3$:Ce, cerium-doped yttrium aluminum perovskite (YAP:Ce). In this material, the Ce^{3+} dopants substitute for Y^{3+} in the lattice and are the source of CL emission from the scintillator, acting individually as point emitters. To satisfy the requirements of scintillator uniformity and flatness, we grow YAP:Ce scintillator films using pulsed laser deposition (PLD), which enables epitaxial growth of the chosen material (YAP:Ce) on top of a substrate with a suitably matched crystal lattice structure. PLD uses a pulsed high power laser to ablate the desired material (target), forming a high energy plume of the substituent atoms. The atoms in the plume travel to a heated substrate, which provides sufficient energy for the atoms to move to positions corresponding to the low energy crystal lattice. This process preserves the stoichiometry of the target material, with possible adjustments made by introducing gas to the PLD process, such as O_2 gas for growing oxide materials.

The scintillator must be thick enough that the electron beam plume does not "leak" through the material in a CLAIRE experiment, so a deposition rate is a limiting factor in the selection of possible methods. Some methods for growing well-ordered crystals layer by layer (e.g. atomic layer deposition) are poorly suited because of slow deposition rates.

Another advantage to having a tens of nanometer thick scintillator is that the scintillator must be robust enough to be free-standing, which is helped by having a thicker scintillator. Other faster methods for thin film deposition, like sputtering, can often yield films that are not sufficiently flat or may have undesirable voids.

To achieve uniform YAP:Ce growth, deposition on a substrate with the matching crystal structure is necessary. We grow YAP:Ce on two buffer layers, 20 nm of $LaAlO_3$ (LAO) and 5 unit cells of $SrTiO_3$ (STO) deposited on Si (200 μm thick, 100 orientation) using molecular beam epitaxy prepared by Zhe Wang in the Darrell Schlom group. YAP:Ce was successfully grown with laser ablation using a KrF laser emitting at 248 nm, with a repetition rate of 8 Hz, and a 47 mJ focused laser beam energy. The substrate, diced to a size of 5 mm by 8 mm, was heated to 770 °C, and a O_2 pressure of 0.41 mTorr to achieve the correct oxygen stoichiometry. Correctly deposited YAP:Ce appears brown. After previous extensive characterization of YAP:Ce grown via PLD, we now more quickly monitor the success of PLD by verifying the CL spectrum, measuring the emitted photon counts relative to a known YAP:Ce sample, and visually inspecting the surface roughness of the deposited material with SE imaging. AFM can additionally be used to verify surface roughness and thickness of the deposited YAP:Ce layer.

3.2.3 Towards YAP:Ce growth on an additional PLD system

To improve our ability to more readily grow YAP:Ce, we also began testing PLD growth parameters using a different system. While growth parameters should be adaptable from the existing PLD system, adjustments were still necessary and have not yet yielded high quality YAP:Ce film deposition. The largest change between PLD conditions was a change in the laser source, with the newer setup using a frequency doubled Nd:YAG laser emitting at 532 nm, with laser powers ranging from 1.5 to 2.9 W and a fixed repetition rate of of 30 Hz. Other tested conditions were close to previously used parameters, with O_2 pressure ranging from 0.5 to 2 mTorr and substrates heated at 780 °C. These PLD conditions yielded growth that primarily comprised nanometer to micron sized boulders of material unevenly deposited on the substrate (Figure 3.2).

This undesirable film morphology may have been caused by the change in laser wavelength from the previously working KrF laser at 248 nm to the Nd:YAG laser emitting at 532 nm. Successfully ablating the target material with the laser is essential for creating desirable conditions in the plume of atoms ablated from the target to achieve proper deposition. If the absorption spectrum of the material does not overlap well with the wavelength of the ablating laser, the target material can undergo other processes, such as subsurface boiling, which can lead to the release of clumps of the target material rather than a fine spray of atoms. To address this issue, we switched to an ultraviolet (UV) excitation source at 266 nm by adding another frequency doubling crystal to the Nd:YAG laser. Continued optimization of the conditions for YAP:Ce growth on this PLD system are now possible. Overall, PLD allows us to achieve the scintillator growth necessary for CLAIRE imaging and further PLD optimizations will improve the experimental pipeline for CLAIRE imaging.

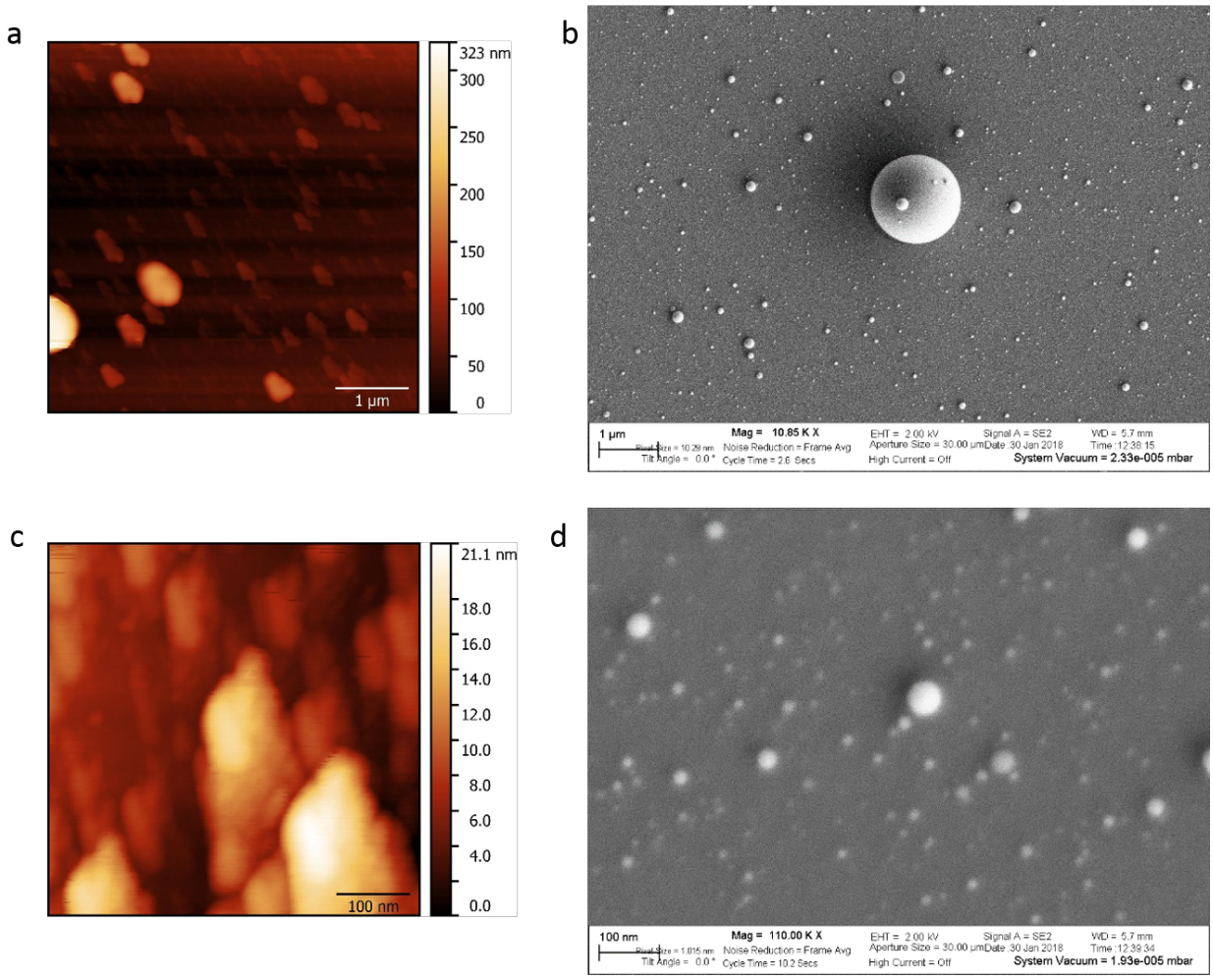

Figure 3.2: AFM and SEM images showing PLD deposited material. (a) AFM image of large deposits of material (b) SEM image of large deposits of material (c) AFM image of smaller deposits of material (d) SEM image of smaller deposits of material

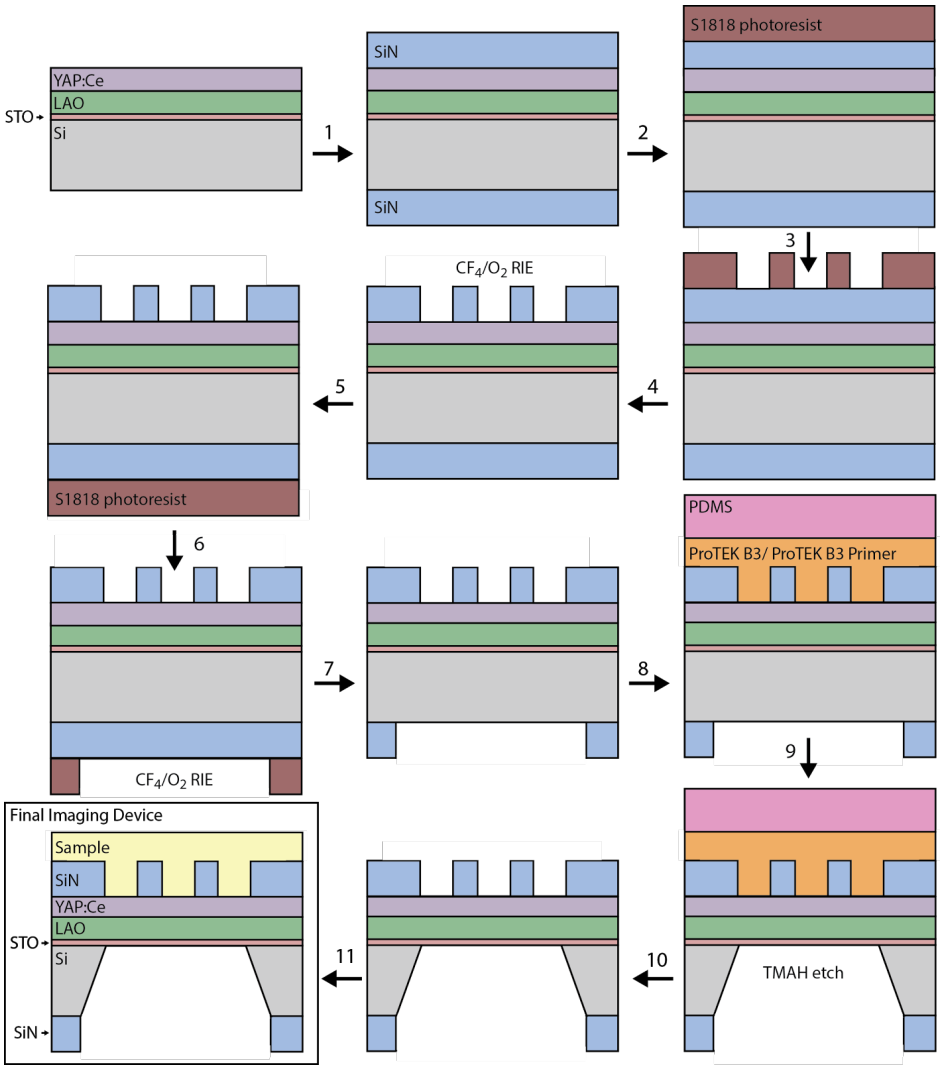

Figure 3.3: Flow chart showing CLAIRE chip wet etch process.

3.3 Production of CLAIRE imaging chips using wet etch lithography

After growing YAP:Ce on the LAO/STO/Si substrates, the next step towards CLAIRE imaging is to modify the chip to produce a free standing film of the scintillator by removing the Si in a small region to create a free-standing membrane. This can be achieved by removing the Si via wet or dry etch. The wet etch process is described here.

3.3.1 Pre-etch chip preparation

The YAP:Ce/Si chip produced with PLD must first be cleaned to remove residual silver paste used to attach substrates to the heater during the PLD process to produce a uniform surface for etching. The YAP:Ce side is first covered using UV release tape to prevent any scratches during this process. The silicon side is then wet polished by hand using 5 μm, 1 μm and 0.5 μm grit diamond lapping paper by using a finger to move the chip across the wet lapping paper in an "figure eight" pattern to ensure even polishing. The polished side is inspected using an optical microscope to ensure that the surface is evenly clean without visible pits. The chip is then removed from the UV release tape and cleaned by soaking in acetone, isopropyl alcohol (IPA), and MilliQ water for 5 minutes each, and further cleaned with an O_2 reactive ion etch (RIE) to remove any organic residue. The chip is then commercially polished on the Si side to produce a smooth, flat surface.

Silicon nitride (SiN) is deposited on both the YAP:Ce and Si sides of the scintillator to provide structural support to the final CLAIRE chip and as an etch stop for the Si side of the chip. The chip is first cleaned with the same acetone, IPA, and water soak followed by O_2 RIE. SiN is then deposited in a 1 μm layer on both sides of the chip using plasma enhanced chemical vapor deposition (PECVD) (Figure 3.3, step 1). The SiN should evenly coat the entire chip, otherwise unprotected areas of the chip will be etched away in subsequent steps of the process.

3.3.2 Patterning the structural support on the scintillator side of the imaging chip

Next, the SiN on the scintillator side is patterned using photolithography. The SiN on this side is patterned with 10 μm wide cylindrical wells in which the scintillator is exposed. This provides a layer of structural support for the scintillator, so that each contiguous area of free-standing scintillator is a 10 μm wide circle surrounded by supportive SiN. The pattern is produced using a photoresist process to selectively etch away the SiN in the desired areas. This is achieved by adding a layer of photoresist (Figure 3.3, step 2), exposing the desired pattern to UV light, and removing the exposed areas of photoresist, leaving the SiN in the desired area exposed (Figure 3.3, step 3). The exposed SiN can then be removed by reactive ion etch (Figure 3.3, step 4). Specifically, this is achieved using the protocol described as follows.

The chip is once again cleaned by soaking in acetone, IPA, and MilliQ water, followed by an O_2 RIE. In addition to removing organic residue, the O_2 RIE process imparts a charge to the substrate surface, making the surface more hydrophilic and helping the photoresist to evenly coat the surface of the chip. S1818 photoresist is pipetted onto the YAP:Ce side of the chip such that the chip is fully covered, and a thin layer is created by spincoating at 6000 rpm for 6 seconds, 2500 rpm for 1 minute, and then 6000 rpm for 6 seconds. The photoresist is heated at 95 °C for 2 minutes on a hot plate to drive off excess solvent and then cooled to room temperature. The chip is placed underneath a chromium mask with the desired circle

array pattern, with the photoresist layer between the chip and the mask. The photoresist is exposed to UV light using a 365 nm wavelength lamp through the mask for 10 seconds at 15 MW/cm^3. The chip is removed from the mask and placed in MF-319 developer for 2 minutes until the exposed resist is dissolved. The chip is then rinsed with water and visually inspected in the optical microscope to ensure that the photoresist is completely removed. In the case of over or underexposure, the circles in the array produced by the chromium mask may be larger or smaller than desired. In this case, the photoresist can be removed by soaking in remover 1165 and the photoresist can be reapplied and re-exposed until the desired size and feature cleanliness is achieved.

The exposed SiN can then be removed using a CF_4/O_2 RIE etch. First, to protect the SiN on the Si side of the chip from undercutting during the RIE process, the chip is taped to a glass slide with Kapton tape covering all four sides of the chip. The SiN is etched with 40 sccm CF_4 and 20 sccm O_2 at 100 W for approximately 2 minutes per 1 μm of SiN. When the etch is finished, the exposed YAP:Ce should be a flat brown color when inspected with an optical microscope. Any residual SiN will appear as green and pink patches on the YAP:Ce and is removed with continued CF_4/O_2 RIE etching until the YAP:Ce is completely exposed. The chip is then detached from the glass slide and the S1818 photoresist is removed by soaking the chip in photoresist remover 1165 for several minutes, until completely dissolved in the remover. The chip is cleaned by soaking in acetone, IPA, and MilliQ water sequentially for 5 minutes each, and then dried with N_2 again.

3.3.3 Removing Si to expose free-standing scintillator

The SiN is then patterned on the Si side of the chip. This side of the chip faces the electron beam in the CLAIRE experiment configuration and has large rectangular wells that expose the YAP:Ce film. On this side of the chip, the SiN primarily acts as a protective layer to confine the etching process to the exposed Si areas created using photolithography. To create the rectangular wells in the Si, the SiN must first be removed to expose the Si to the etching solution. This pattern is produced using the same photoresist and CF_4/O_2 RIE process as is used for the YAP:Ce side of the chip. The chip is again cleaned via O_2 RIE and S1818 photoresist is spincoated on the Si side of the chip and baked as described above (Figure 3.3, step 5). The chip is then taped on a laminate mask with larger rectangular features and exposed to UV light for 10 seconds at 15 MW/cm^3. The exposed photoresist is removed as previously described and the remaining photoresist is inspected (Figure 3.3, step 6). The chip is once again attached to a glass slide with Kapton tape, and the exposed SiN is removed with the same CF_4/O_2 RIE process (Figure 3.3, step 7). Again, the etch is visually inspected for remaining SiN and is continued until the Si is fully exposed and the etched rectangles are a uniform silver color. The photoresist can then be removed by soaking in remover 1165, and the chip is cleaned by soaking in acetone, IPA, and MilliQ water, and dried with N_2.

Before the Si can be etched, the patterned scintillator side of the chip must be protected from the etching solution with layers of ProTEK B3 polymer and polydimethylsiloxane

(PDMS) (Figure 3.3, step 8). First, ProTEK B3 primer is spincoated onto the chip at 2500 rpm and an acceleration of 7000 rpm/s and baked at 205 °C for 5 minutes. Another layer of ProTEK B3 primer is applied using the same spincoating and baking conditions. The ProTEK B3 is applied by spincoating at 6000 rpm with an acceleration of 7000 rpm/s for 6 seconds, then 2500 rpm and 7000 rpm/s for 1 minute, and finally 6000 rpm and 7000 rpm/s for 6 seconds, in sequence. The ProTEK B3 is then baked for 10 minutes at 130 °C and 45 minutes at 205 °C and the chip is cooled to room temperature. PDMS is prepared by mixing 3 g of PDMS with 0.3 g of PDMS curing agent in a plastic weigh boat and degassed by applying vacuum to a plastic vacuum container for 30 minutes. The PDMS is spincoated on top of the ProTEK B3 layer at 1000 rpm for 5 minutes and cured at 120 °C for 30 minutes.

With the other side of the chip protected, the Si is ready to be etched (Figure 3.3, step 9). First, the native oxide layer on the Si is removed with a KOH etch. A 30% KOH solution is heated to 70 °C and the chip is placed in a Teflon holder in a Teflon basket and submerged in the KOH solution for 10 minutes. The basket with the chip is then quickly transferred to a 25% tetramethyl ammonium hydroxide (TMAH) solution and heated at 50 °C overnight. After etching overnight, the chip is transferred to a fresh 25% TMAH bath heated at 30 °C and left to etch for several more hours until the Si is gone and the free-standing circles of scintillator are visible. Etching can be monitored by holding the chip up to a light source to see if the opaque Si has been sufficiently removed. The Teflon basket containing the chip is then transferred to water to rinse away the TMAH from the chip. The protective PDMS and ProTEK B3 layers are removed by soaking the chip in ProTEK remover for 45 minutes (Figure 3.3, step 10). The chip is cleaned by carefully dipping in MilliQ water sideways to avoid putting pressure on the free-standing scintillator windows and finally cleaned by dipping in spectroscopic grade methanol.

With this lithography process, the goal of creating free-standing scintillator windows for a CLAIRE experiment while maintaining enough structural stability to perform the experiment is achieved (Figure 3.3, step 11). Another lithography method, using a deep reactive ion etch to remove the Si and dispensing with the SiN structural framework on the scintillator side, has also been developed and successfully used for CLAIRE experiments.

3.4 CLAIRE microscopy using nanoparticle labels

CLAIRE greatly reduces the electron beam-sample interaction compared to direct electron microscopy, which enables studying nanoscale dynamics in soft material samples. To benchmark this capability, we require a controllable sample that exhibits some dynamic behavior in an environment compatible with CLAIRE microscopy. One possibility is metal nanoparticles, which are a desirable CLAIRE contrast agent because they are robust to photobleaching, which otherwise causes undesirable signal decay, and because they interact through a resonant interaction, that is typically longer-range than the FRET interaction that would be occur with an organic chromophore. This interaction also scales with the curvature of the metal particle, rendering shapes with high curvature, such a nanocube corners, particularly

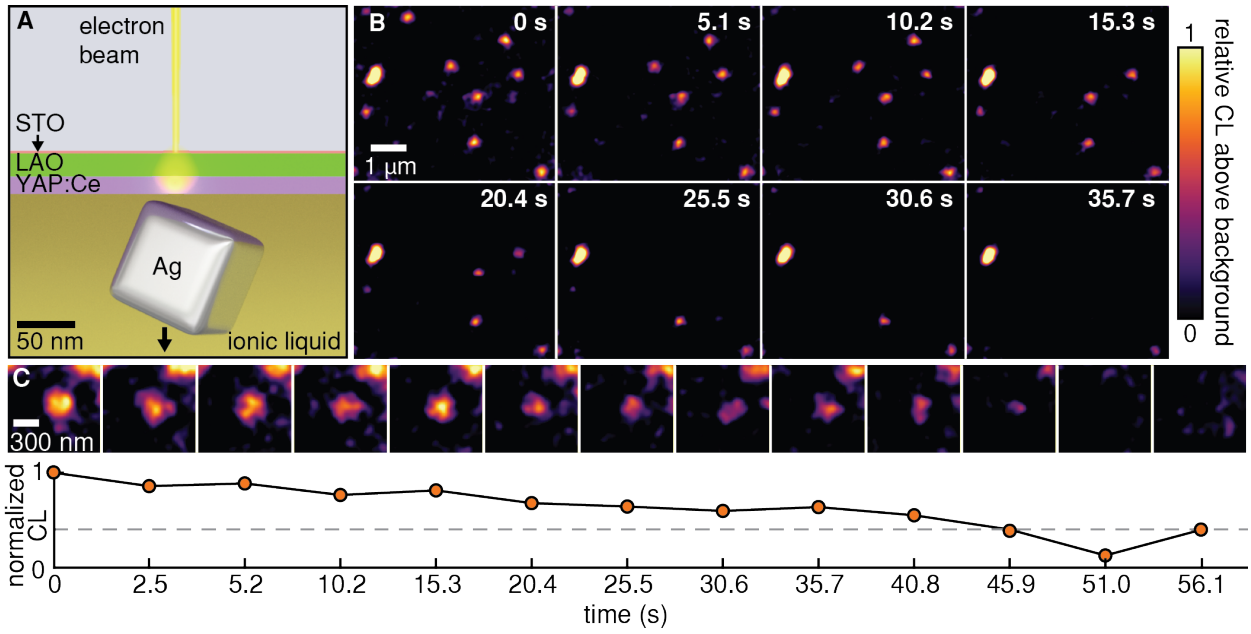

Figure 3.4: Imaging dynamic desportion of Ag nanocubes with CLAIRE microscopy. (a) Schematic of CLAIRE imaging of Ag nanocubes in ionic liquid. (b) Frames from a CLAIRE movie showing particle desorption from the scintillator. (c) CLAIRE images of the gradual desorption of a single particle and plot of the corresponding CLAIRE signal. Adapted from Reference [76].

useful. Nanoparticle labels are commonly used in other microscopy techniques and metal nanoparticles could similarly be used as labels for CLAIRE imaging in a variety of systems that are non-luminescent.

3.4.1 CLAIRE imaging of metal particle desorption

In earlier work, metal nanostructures deposited on the sample side of the scintillator surface of a CLAIRE chip had been shown to locally enhance the scintillator emission, suggesting that metal nanoparticles should provide good contrast for CLAIRE imaging [74]. The next requirement for studying dynamics instead of static structures is to provide an environment in which the nanoparticles are able to move. We do so by immersing the particles in a low vapor pressure liquid environment, which is compatible with the vacuum environment inside the SEM used for CLAIRE imaging. Silver nanocubes that are 100 nm wide were dropcast onto the scintillator side of a CLAIRE imaging chip and covered with a 0.5 μL drop of 1-Butyl-3-methylimidazolium hexafluorophosphate ($BMIM^+$ PF_6^-), a low vapor pressure ionic liquid. The CLAIRE chip is then flipped upside-down from the sample deposition position such that in the final sample geometry, Ag nanocubes initially adhere to the bottom of the

CLAIRE imaging chip with a volume of ionic liquid surrounding them (Figure 3.4a).

The metal nanoparticles that were deposited on the scintillator surface appear in CLAIRE images as enhancement of the scintillator above the position of the nanoparticle, which can be verified by increasing the accelerating voltage and penetration depth of the electron beam to directly visualize the metal particles through the scintillator membrane. For the 100 nm Ag cubes, CLAIRE contrast was found to be highest in the range of 480 nm to 540 nm, so subsequent data were collected in that wavelength range. We found that with continued imaging, the bright spots corresponding to the Ag nanocubes disappear (Figure 3.4b). This can be explained by the particles originally at the scintillator surface moving further away as they desorb from the surface and are suspended in the bulk liquid. Many nanocubes desorb quickly, but for slower desorbing nanocubes, the desorption can be tracked over time, with gradually decreasing CL signal indicating that the nanocube is slowly moving away from the scintillator (Figure 3.4c). The loss of signal is attributed to desorption and not electron beam induced decomposition because the scintillator film greatly reduces the extent of electron interaction with the sample, as discussed in Section 3.4.2. These dynamics were measured at framerates of 1.23 fr/s, demonstrating that CLAIRE imaging is capable of simultaneous high spatial and temporal resolution. The ultimate time and spatial resolution of the experiment depends on the combination of the electron beam scan speed and the size of the measured field of view, so higher time resolution can in principle be attained by scanning the smallest field of view that still captures the desired sample dynamics.

3.4.2 CLAIRE imaging of polymer particle motion

One of the advantages of CLAIRE imaging is its reduced invasiveness compared to direct electron microscopy techniques. To demonstrate that CLAIRE is capable of imaging dynamics in a sample that is substantially more electron beam sensitive, we observe polymer nanoparticle motion with CLAIRE using the experimental scheme shown in Figure 3.5a. Nanoparticles made of a blend of poly(9,9-di-*n*-octylfluoronyl-2,7-diyl) (PFO) and poly[((9,9-di-*n*-octylfluorenyl-2,7-diyl)-*alt*-co-(1,4-benzo-2,1',3-thiadiazole)] (F8BT) were mixed into a low vapor pressure liquid (Edwards Ultragrade 19 vacuum pump oil), placed under vacuum to remove excess solvent, and the resulting solution was dropcast onto a CLAIRE imaging chip. The polymer blend is chosen such that the absorption spectrum (Figure 3.5b, blue curve) overlaps with the emission spectrum of the YAP:Ce scintillator (Figure 3.5b, purple curve) and the emission spectrum is sufficiently red-shifted (Figure 3.5b, green curve) so that the signal can be easily spectrally separated from the YAP:Ce emission and detected between 530 nm to 590 nm.

We verify that we can detect the fluorescence from the polymer nanoparticles as expected, as shown in a CLAIRE image of two nanoparticles (Figure 3.5c). Additionally, this demonstrates that CLAIRE imaging is non-invasive. We show that the sample is sensitive to the electron beam by initially taking a CLAIRE image (Figure 3.5d), increasing the electron beam accelerating voltage to allow direct electron beam-sample interaction through the scintillator, and then taking a CLAIRE image of the same particle after electron beam expo-

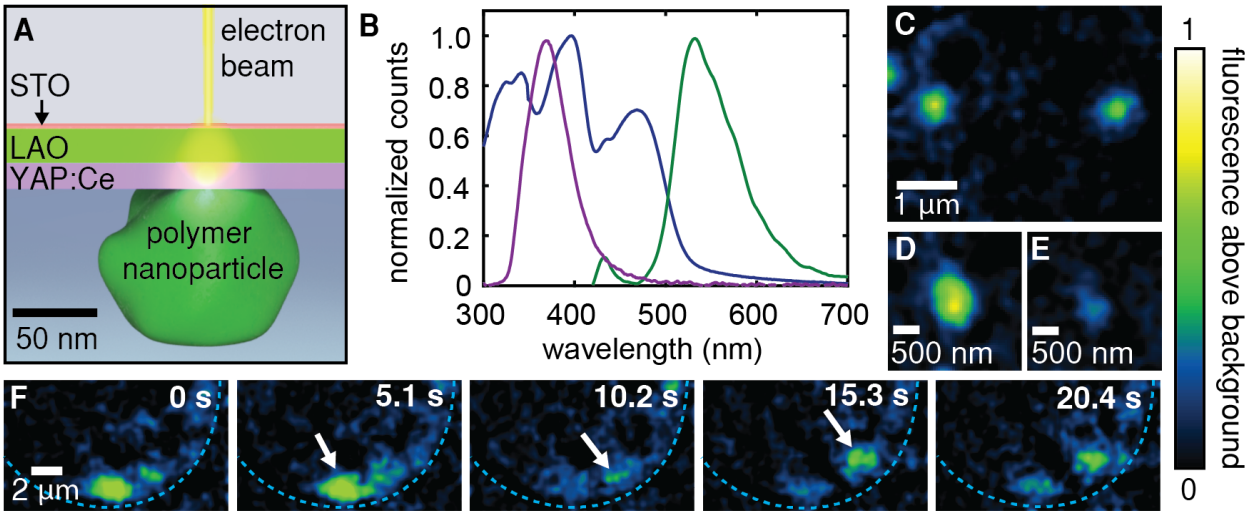

Figure 3.5: Imaging polymer nanoparticle motion with CLAIRE microscopy. (a) Schematic of CLAIRE imaging of polymer nanoparticles. (b) CL spectrum of YAP:Ce (purple) and polymer nanoparticle absorption (blue) and emission (green) spectra. (c) CLAIRE image of two polymer nanoparticles. (d) CLAIRE image of a single polymer nanoparticle. (e) Reduction in the emitted light from the same particle shown in (d) after increasing the electron beam penetration depth. (f) CLAIRE image time series showing polymer nanoparticle motion. Adapted from Reference [76].

sure (Figure 3.5e). The fluorescence signal is greatly reduced after the direct electron beam exposure, showing that CLAIRE imaging does reduce the electron beam-sample interaction and enables imaging of samples that would otherwise be too fragile for direct electron beam imaging. Additionally, we image dynamics of these polymer nanoparticles. Frames from a CLAIRE movie show the position of the fluorescence signal shifting over time (Figure 3.5f). This is due to some motion of the polymer nanoparticle, possibly polymer nanoparticle shifting or translating across the scintillator surface. The shift in signal is unlikely to be caused by decomposition of the nanoparticle because a decomposition should appear as a decrease in the polymer particle fluorescence rather than the lateral shift of the bright fluorescent spot. The motion could be caused by either heat or charge accumulation in the scintillator which would change the adhesion of the particle to the scintillator surface and cause the particle to move. Overall, this demonstrates that CLAIRE is capable of imaging dynamics in soft material samples.

3.4.3 Future applications of nanoparticle CLAIRE labels

Having shown that CLAIRE microscopy is capable of non-invasively imaging motion in nanoparticle samples, we are positioned to extend this work to more complex systems. CLAIRE imaging is only sensitive to contrast near the scintillator film, which makes studying two-dimensional translation parallel to the scintillator film appealing, since the contrast mechanism will inherently reject any bulk signal contribution. This direction also draws upon our work imaging nanoparticle dynamics at an ionic liquid droplet surface using SEM (Chapter 4), which is also a two-dimensional electron beam sensitive process. Well-characterized CLAIRE labels are an important part of the CLAIRE imaging toolkit because they are adaptable to a wider range of samples than CLAIRE imaging of samples with endogenous interactions with YAP:Ce. Developing a new scintillator with a different spectrum for each new sample's endogenous chromophore is also more involved than employing labels.

3.5 Aqueous encapsulation with graphene for CLAIRE

CLAIRE imaging is additionally well-suited to soft material samples because the scintillator film physically separates the vacuum environment of the SEM from the sample. This separation enables the sample to have its own environment, which is particularly important for biological soft material samples that require an aqueous environment. Towards this end, we have developed an aqueous encapsulation scheme compatible with the CLAIRE imaging chips with the goal of imaging biological soft materials in a suitable environment. Graphene has been previously demonstrated as a suitable material for aqueous encapsulation for electron microscopy [77]. Previous efforts have used graphene alone or in conjunction with other materials to image various samples under aqueous conditions [78, 79]. We developed a graphene encapsulation method that additionally incorporates the geometry of the CLAIRE imaging chip.

To contain a sample, the encapsulation method must be compatible with the CLAIRE imaging chip. With the existing chip geometry, the sample is surrounded on the sides by the supporting SiN framework and on the electron beam side by the scintillator film (Figure 3.6). The sample side is the remaining side to be enclosed to achieve aqueous encapsulation. Therefore, the goal is to use graphene as the bottom layer of the enclosure.

3.5.1 Graphene encapsulation method

Development of the graphene encapsulation method was tested using the SiN framework described in Section 3.3 deposited on a glass slide rather than the CLAIRE chip scintillator. This method preserves the geometry of the system while being more compatible with optical microscopes to verify the aqueous encapsulation. Additionally, the graphene layer's seal depends most strongly on the interaction between the graphene and SiN, so substituting a different material for the scintillator should not change the effectiveness of the encapsulation method. The glass test substrates are also simpler to construct than CLAIRE imaging chips,

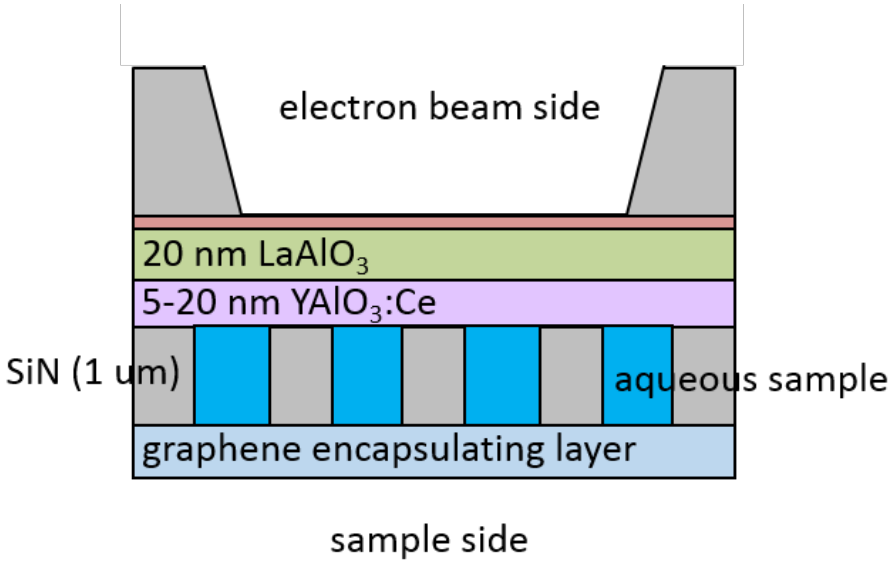

Figure 3.6: CLAIRE encapsulation diagram.

enabling faster testing of different encapsulation methods. The following methods have not yet been used on the more fragile CLAIRE imaging chips.

We used a water-mediated graphene transfer process to place graphene on the test SiN framework substrate (Figure 3.7). This was useful because it could be easily adapted to the necessary aqueous conditions required by the sample (e.g. if the sample required a particular buffer solution). In this case, multi-layer (6 to 8 layers) graphene was used for increased mechanical robustness and further strengthened by spincoating a thin supporting layer of poly(methyl methacrylate) (PMMA). Commercial multilayer graphene grown by chemical vapor deposition on copper foil was treated by O_2 reactive ion etch to remove graphene from one side of the copper foil (Figure 3.7, step 1). PMMA (495,000 molecular weight in anisole, at 6% weight concentration) was spincoated at 5000 rpm for 50 seconds onto the graphene side of the copper foil to produce a layer approximately 500 nm thick (Figure 3.7, step 2). The copper foil was removed by floating the copper foil/graphene/PMMA stack on the surface of a 20% ammonium persulfate etching solution until no visible copper foil remained (Figure 3.7, step 3). To rinse away remaining etchant, a clean glass slide was used to transfer the remaining graphene/PMMA stack to the surface of clean water. To perform this transfer, the glass slide was slid underneath the floating graphene/PMMA stack and lifted from underneath to pick up the graphene (Figure 3.7, steps 5 and 6). The glass slide was then lowered into fresh water at an angle, and so long as the graphene had not dried onto the glass slide, the graphene could be floated on the surface of the water (Figure 3.7, step 7). This process was repeated at least twice to remove residual copper ions and etchant solution. The graphene/PMMA stack was then transferred to the surface of the desired sample solution

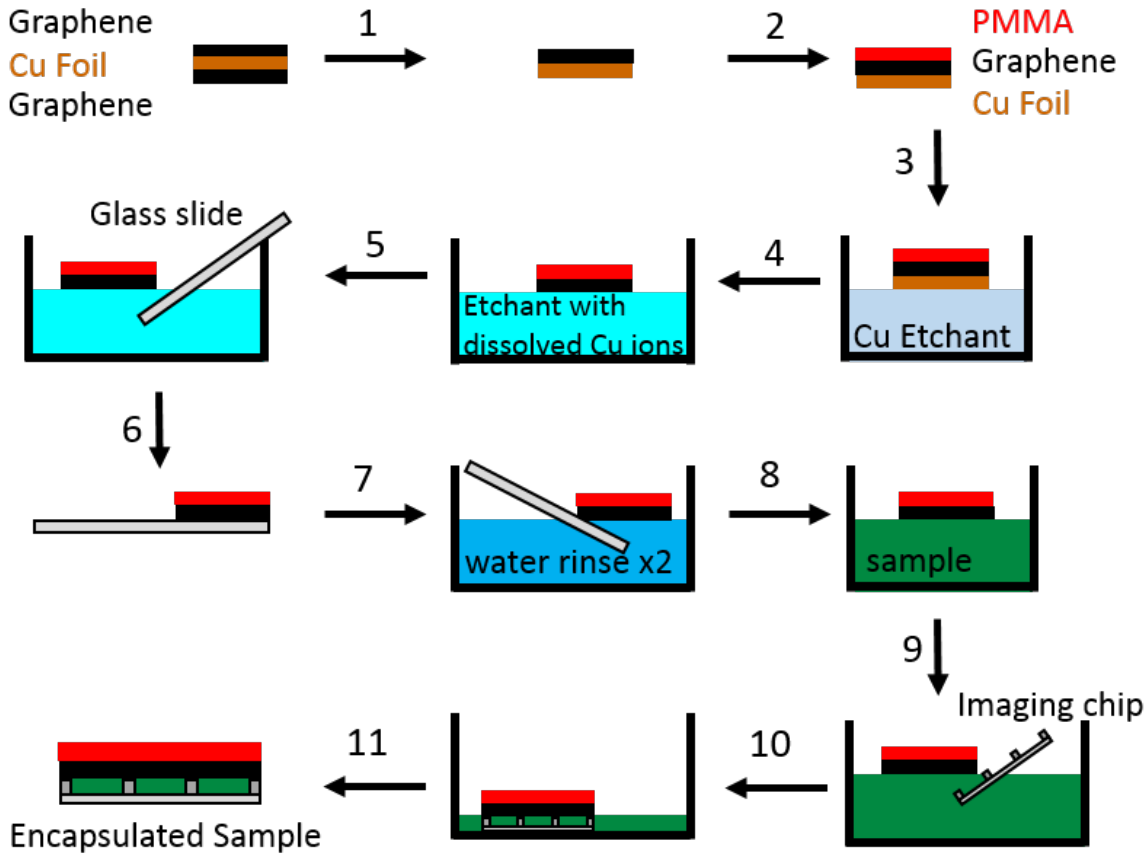

Figure 3.7: Diagram of Graphene Encapsulation Method.

using the same glass slide method (Figure 3.7, step 8). Encapsulation could then be achieved by submerging the test CLAIRE chip underneath the graphene/PMMA stack (Figure 3.7, step 9) and removing excess sample solution until the graphene/PMMA stack falls down onto the top surface of the chip (Figure 3.7, step 10). After removing the encapsulated chip from the remaining solution and allowing any excess solution to evaporate from between the graphene/PMMA stack and the substrate (Figure 3.7, step 11), the remaining solution was sealed in the wells formed by the SiN.

3.5.2 Graphene Encapsulation Testing and Verification

To test graphene encapsulation of aqueous solution, we used a solvatochromic dye, coumarin 343, which emits at a different wavelength in its hydrated and dry forms (Figure 3.8). When hydrated, it emits strongly at 490 nm and when dry, it emits much more weakly at 580 nm. The spectra in Figure 3.8b have been normalized to show the wavelength shift and have not

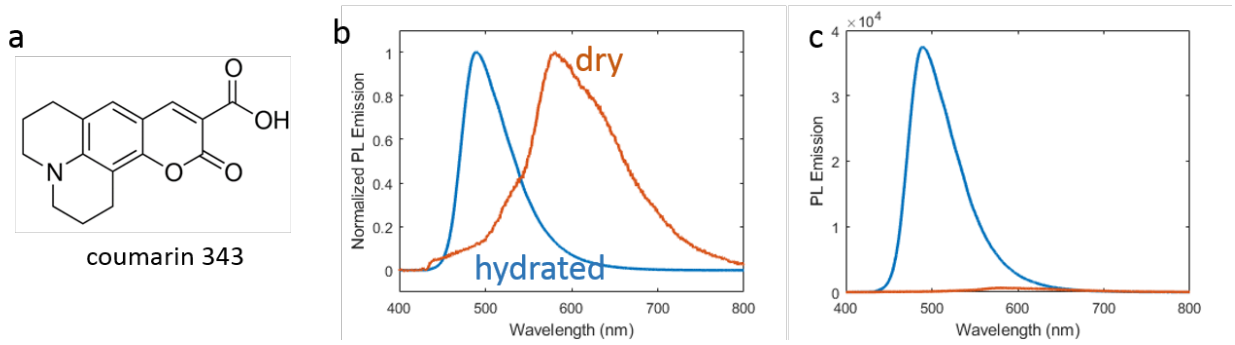

Figure 3.8: Coumarin 343 structure (a) normalized photoluminescence spectrum (b) and un-normalized photoluminescence spectrum (c)

been nomalized in Figure 3.8c to show that the hydrated emission is much stronger than the dry emission. PL spectra were recorded by exciting with a 405 nm LED focused through a confocal microscope and detected by using a fiber to couple the signal to a QE65PRO spectrometer with a HC1-QE grating (Ocean Optics). The wet spectrum was collected by pipetting a saturated coumarin 343 solution onto a glass coverslip and the dry spectrum was recorded after the water had evaporated.

Using a confocal laser scanning microscope with an excitation source at 405 nm, we verified the presence of water trapped in the SiN wells of the test substrate (Figure 3.9a). The presence of water was confirmed in the confocal microscope after having left the encapsulated test substrate in the SEM vacuum chamber overnight, (Figure 3.9b) showing that the encapsulation method is more than sufficient for the vacuum conditions required by the CLAIRE experiment (Figure 3.9). While the emission from the sample after testing in the vacuum chamber is dimmer, the wavelength of the emission still corresponds to that of hydrated coumarin 343 and should still indicate the presence of water. One possible contribution to the dimming luminescence is that the coumarin 343 solution used for these experiments is a saturated solution and coumarin 343 has limited solubility in water [80]. As time elapses, solvated coumarin 343 could attach to the sides of the encapsulating well. In particular, graphene is capable of quenching the emission of nearby fluorophores and could plausibly quench more of the coumarin 343 emission if the dye were to settle at that interface [81]. The graphene encapsulation method was also tested on a solution of fluorescent microbeads and confirms that the sample particles in solution can be trapped using this method.

Additionally, we verified that the encapsulated water remains fluid. Fluorescence recovery after photobleaching (FRAP) is a commonly used technique to measure diffusion of a fluorescent dye into a bleached area. By photobleaching the coumarin 343 in one of the SiN wells containing water, we observe the recovery of hydrated coumarin 343 signal within that well (Figure 3.10 a,b,c). This shows that the coumarin 343 is able to diffuse into the encapsulated well, confirming that the encapsulated water is fluid. However, it also demonstrates

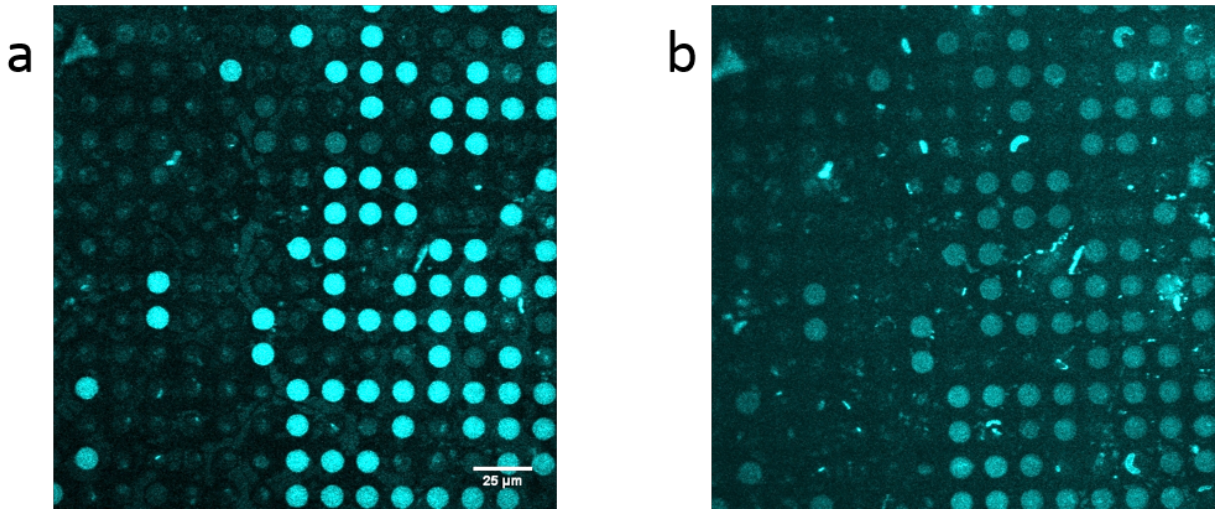

Figure 3.9: Emission of hydrated coumarin 343 encapsulated in wells (a) after drying at ambient conditions and (b) after 14 hours in the SEM vacuum chamber. Luminescence corresponds to the presence of hydrated coumarin 343 and the dimmer luminescence in (b) is likely caused by coumarin 343 settling out of solution.

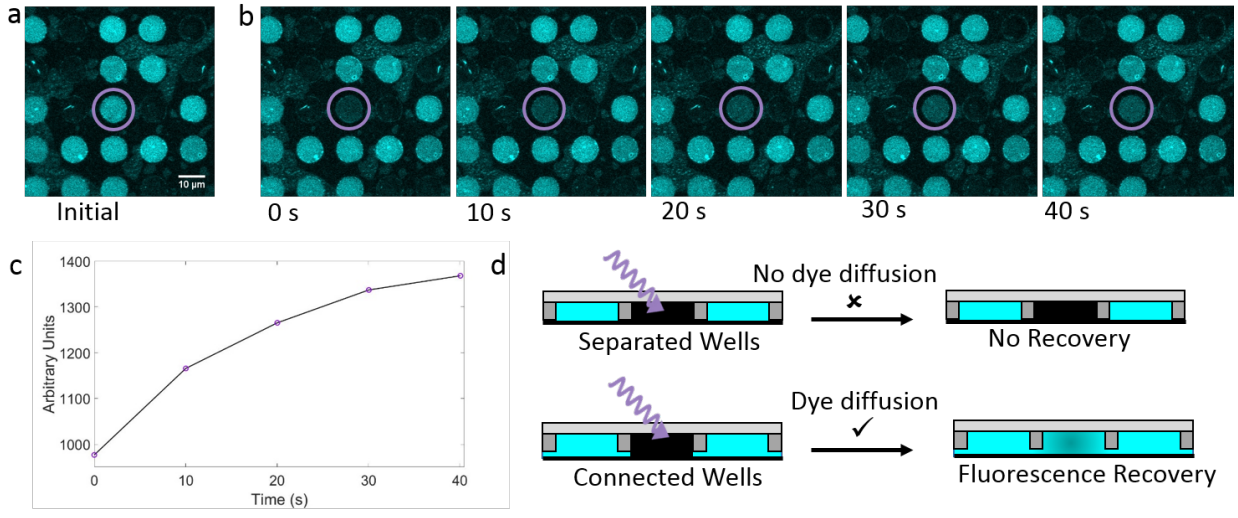

Figure 3.10: Characterization of coumarin 343 diffusion (a) Wells containing hydrated coumarin 343 fluoresce blue (false color). (b) Time series of center well post-bleach (purple circle) (c) Plot of fluorescence recovery. (d) Diagram of possible encapsulation scenarios.

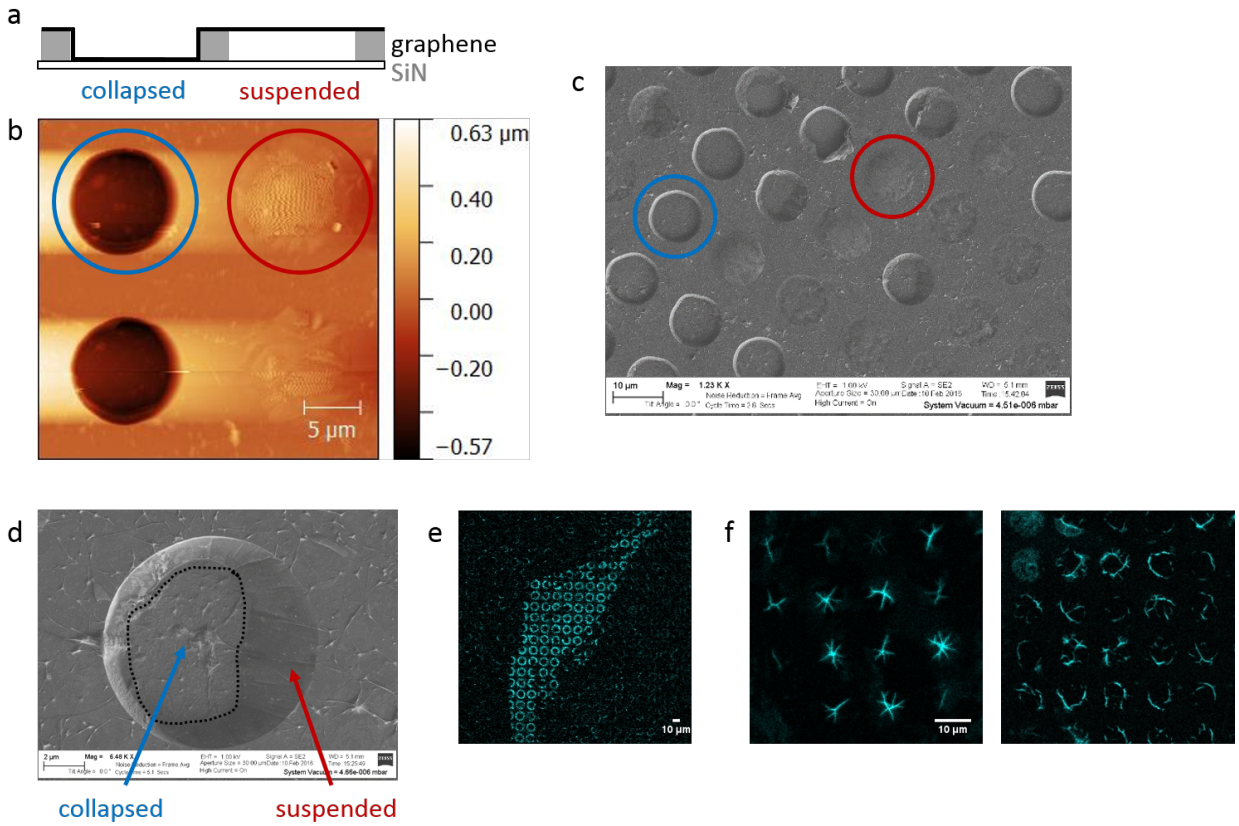

Figure 3.11: Images of graphene encapsulation over a test chip. (a) Diagram of graphene (black) sunk into (left) or suspended over (right) SiN wells (gray). (b) AFM image of graphene sunk into (left, blue circle) and suspended over (right, red circle) wells. (c) SEM image of graphene covering a chip, with a mixture of graphene sunk into (blue circle) and suspended over (red circle) wells. (d) SEM image of graphene partially suspended over a well, with the sunken-in region outlined in black. (e) Fluorescence image showing examples of partial encapsulation with the graphene in the center of the well collapsed. (f) Fluorescence images showing partial encapsulation with solution trapped in graphene wrinkles.

that coumarin 343 can diffuse between encapsulated wells, so the wells are not encapsulated as isolated entities but rather as networks of connected wells (Figure 3.10d). While isolated wells might be more advantageous in the event that a portion of the encapsulation fails, such as the thin free-standing scintillator cracking above a well, they are not a necessary requirement for aqueous encapsulation.

3.5.3 Graphene encapsulation method development

To arrive at the successful encapsulation method described here, troubleshooting was focused entirely on the application of the graphene layer, since the substrate geometry is set by the pre-existing CLAIRE chip design. The largest hurdle to successful encapsulation was the graphene's inherent flexibility that allows it to adhere to both the sides and bottom of the well, pushing out the sample solution rather than encapsulating it, depicted in Figure 3.11a (left), where the wells formed by the SiN supports are exaggerated in height for clarity. This can be visualized with atomic force microscopy (AFM) (Figure 3.11b) and SEM (Figure 3.11c), which shows wells with graphene sunk into the bottom (blue circles) and wells with graphene suspended above the well as desired (red circles). Other intermediate forms, where the graphene collapses into the center of the well but leaves some remaining fluid around the edges (Figure 3.11 d,e) or where the graphene traps liquid in wrinkles inside the well are also possible (Figure 3.11f).

To reduce the flexibility of the graphene, PMMA was chosen as a readily available material that could be added to the graphene to increase the thickness and reduce the flexibility. PMMA thickness could be easily changed by varying the speed at which the PMMA is spincoated into the graphene layer. Maintaining some of the flexible nature of the graphene/PMMA stack is advantageous for the stack to be able to make good contact with the rigid substrate. PMMA provides the additional benefit of holding the graphene stack together during the copper etch and water rinse processes. At these stages, graphene alone is susceptible to breaking apart or wrinking in on itself as it adheres to the glass slide used for transfer. The PMMA prevents this occurrence and therefore improves the ability to produce a contiguous encapsulating layer.

The PMMA thickness ultimately controls how well the graphene encapsulation works. The current protocol produces a PMMA layer that is is 500 nm thick. If the PMMA is too thin (thinner than 300 nm), the graphene/PMMA stack is not rigid enough to remove the issues caused by graphene flexibility. However, when the PMMA is too thick (thicker than 1 μm), the encapsulation also appears to be less successful, possibly because the encapsulation requires the graphene to conform to the SiN framework, and the rigidity of excessively thick PMMA may reduce this interaction. The thickness of the applied PMMA layer can be controlled both by spincoating parameters and by the initial concentration of the PMMA solution. With too low of a PMMA concentration, the resultant PMMA layer is too thin to provide support for the graphene layer, and with too high PMMA concentration, the PMMA layer is too thick for the graphene layer to adhere well to the substrate. Concentrations between 4 wt% and 11 wt% PMMA were tested and 6 wt% yielded the most consistent results. Spincoating speeds also change the thickness of the PMMA, with faster speeds producing thinner PMMA layers. Speeds between 1,000 rpm and 10,000 rpm were tested, and 5,000 rpm worked most consistently with the 6 wt% PMMA. Because there are two parameters to control PMMA thickness, PMMA concentration and spin speed, this exact combination is probably not a unique solution and the 500 nm thickness of the resulting PMMA layer is the most important result. One additional consideration is that the spincoating conditions

may change the uniformity in the thickness of the PMMA layer, especially considering the higher viscosity of concentrated PMMA solutions.

Possible approaches to producing higher yields of encapsulated wells include changing the CLAIRE chip geometry by tuning the aspect ratio of the wells, either by decreasing the diameter to make the suspended graphene area smaller or increasing the depth of the wells to increase the tolerance for graphene bending into the well. Another avenue for optimization is to continuing to tune the thickness of the PMMA layer beyond the tested parameters to match those conditions. Changing the CLAIRE chip geometry has tradeoffs; with a smaller well diameter, less YAP:Ce scintillator area will be available for imaging and practical lithography considerations limit the depth of SiN that can easily be deposited and etched into wells. Graphene encapsulation is compatible with the current CLAIRE chip design. While continued optimization will be useful for increased experimental simplicity, the current graphene encapsulation method is sufficient for a CLAIRE experiment of an aqueous sample.

3.6 Towards CLAIRE of photosynthetic membranes

CLAIRE microscopy is particularly well-suited for soft material samples with high concentrations of endogenous chromophores that preclude the use of specific fluorescent labels by crowding the available wavelength range. One target system is the motion of the photosystem II protein complex within photosynthetic membranes [82]. Photosystem II (PSII) complexes are housed in the grana, structures comprised of closely stacked membrane discs inside of the chloroplast. When PSII is photodamaged, it must move to the stroma, more loosely packed regions of the membrane, where the repair protein complex is housed. Currently, PSII motion has not been directly observed and whether PSII diffuses randomly to arrive at the stroma or moves in a directed manner towards the stroma is not known. Protein diffusion within grana has been characterized recently with high speed AFM, but unambiguous assignment of similarly sized protein complexes remains a challenge for high speed AFM [83]. Many of the protein complexes in these photosynthetic structures contain different chromophores and the chromophores are densely packed, making other super-resolution fluorescence methods difficult to apply. CLAIRE is well suited for this system, since it can take advantage of a native PSII chromophore, chlorophyll *a*. The emission spectrum of the YAP:Ce scintillator overlaps with the absorption spectrum of chlorophyll *a* so that using the endogenous chromophore as the fluorescent reporter is possible. In this scenario, CLAIRE would enable label-free super-resolution imaging of photosynthetic membranes.

3.6.1 Preliminary encapsulation of photosynthetic structures

Aqueous encapsulation is particularly important for imaging dynamics in photosynthetic membranes, since proteins in dry membranes are not capable of motion. An intermediate approach to the full aqueous encapsulation described in Section 3.5.1 is to use graphene to en-

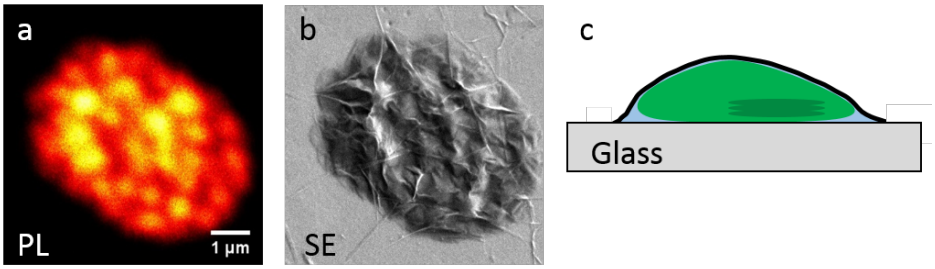

Figure 3.12: Correlated PL and SE imaging of a DEC. (a) PL image of encapsulated DEC cholorphyll *a* emission. (b) SE image of the same encapsulated DEC. (c) Diagram of encapsulated DEC

capsulate larger photosynthetic structures, such as de-enveloped chloroplasts (DECs), which are able to provide structural support to the graphene. In this case, multilayer graphene was prepared as described in Section 3.5.1 without the addition of the PMMA layer.

DECs were deposited on glass or silicon and that substrate was submerged under a clean floating multilayer graphene stack and lifted to encapsulate the sample under the graphene. Intermediate to CLAIRE, this approach also enables correlated SEM and fluorescence imaging of the same DEC sample, although this approach is not capable of capturing dynamics of nanoscale fluorescence information (Figure 3.12). The graphene encapsulated DEC was first imaged with a scanning confocal microscope, detecting the native chromophore chlorophyll *a*. The same sample was then imaged at 2 kV in the SEM. In this case, the graphene layer is sufficiently conductive that the insulating glass substrate does not accumulate charge to an extent that is detrimental for imaging. The encapsulated DEC retains its expected oval shape and the characteristic puncta, highly emissive spots a few hundred nm in diameter corresponding to stacks of grana, are visible in both the PL image and SE image. In this case, coumarin 343 encapsulated with the DECs was an unreliable reporter on the hydrated state of the sample, possibly because the DEC provided an environment that was more similar to the hydrated than dry environment. The coumarin 343 was dissolved into the aqueous solution used to transfer the graphene layer on top of the sample and should have been present in any encapsulated water.

Another approach to encapsulation is to replace the aqueous environment with a low vapor pressure liquid environment. Because the low vapor pressure liquid will remain as a liquid in the SEM vacuum chamber, it does not need to be additionally encapsulated. Additionally, if the refractive index of the liquid is similar to the refractive index of the sample, the presence of the liquid prevents internal reflection of emitted sample photons from the sample-vacuum interface. The sample-vacuum internal reflection otherwise creates an interference signal as a result of the difference in path length between light reflected from the sample-vacuum interface and light from the sample-scintillator interface. This interference signal appears on top of the desired CLAIRE signal, so removing the undesired

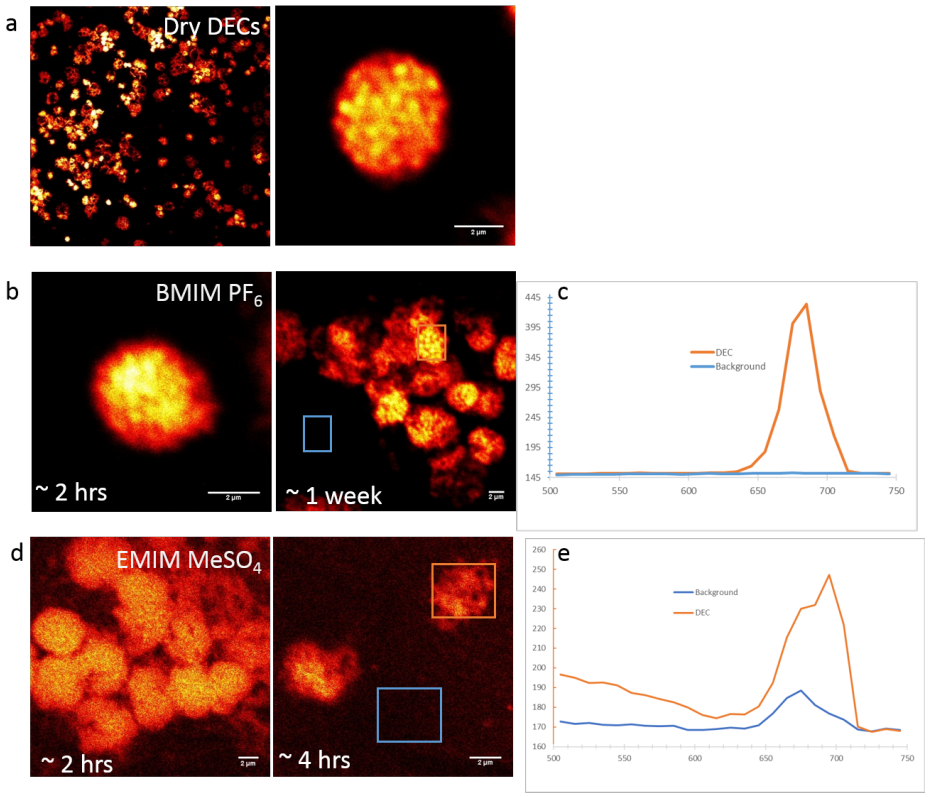

Figure 3.13: Images and spectra of DEC stability in ionic liquids. (a) PL images of dry DEC controls. (b) PL images of DECs surrounded by $BMIM^+$ PF_6^-. (c) PL spectra of DECs (orange box) and background (blue box) after one week. (d) PL images of DECs surrounded by $EMIM^+$ $MeSO_4^-$. (e) PL spectra of DECs (orange box) and background (blue box) after four hours.

interference signal is advantageous. On the other hand, using low vapor pressure liquid removes the benefit of being able to observe the sample in a relevant aqueous environment. For the DECs, this may not be necessary since the imaged area of the sample is directly in contact with the CLAIRE chip and the ionic liquid would primarily be in contact with the opposite side of the chloroplast, similar to the geometry in Section 3.4.

We verified the compatibility of the DEC sample with different ionic liquids (ILs), a class of low vapor pressure liquids. DECs were deposited on clean glass substrates and covered with a droplet of IL. In control DECs not covered by IL, puncta corresponding to stacks of grana are characteristically visible. DEC samples covered in 1-butyl-3-methylimidazolium hexafluorophosphate ($BMIM^+$ PF_6^-) retained clear puncta and normal chlorophyll a spectra after a week of being covered. However, DEC samples covered in 1-ethyl-3-methylimidazolium methyl sulfate ($EMIM^+$ $MeSO_4^-$) degraded on the timescale of a few hours. The puncta

became less distinctly visible and the background fluorescence spectrum contained contributions from chlorophyll *a*. This demonstrates that DECs are not stable in $EMIM^+$ $MeSO_4^-$ and some chlorophyll *a* previously confined to the DECs was solubilized in the bulk IL. However, $BMIM^+$ PF_6^- appears to be a good choice for IL encapsulation of DECs.

3.7 Conclusions and outlook

CLAIRE imaging combines the advantages of nanoscale resolution, fast scanning to enable capturing dynamics, and chemical specificity. We have benchmarked our ability to image nanoparticle dynamics with CLAIRE, which is both inherently interesting and useful for future applications as CLAIRE-compatible labels. We have also established a protocol for using CLAIRE imaging with solvent environments that are not inherently compatible with the SEM vacuum environment, providing a path towards future experiments with samples in an aqueous environment. Finally, we have begun to test CLAIRE imaging on photosynthetic membranes which are interesting systems that can not be readily studied with existing super-resolution microscopy techniques. With the combination of these developments, we are well poised to continue using CLAIRE imaging for a variety of future samples.

Chapter 4

Electron beam induced dynamics in doped colloidal interfacial monolayers

4.1 Introduction

Colloids provide an accessible platform as model systems for studying interatomic and intermolecular interactions and associated phase behavior as well as a platform for the bottom-up design of next generation materials [25]. Colloidal systems are most typically studied with optical microscopy, which is well developed but limited to particle sizes above the optical diffraction limit. With scanning electron microscopy's superior spatial resolution, we are able to study colloidal systems comprised of smaller particles. This is particularly important for studying particle interactions that scale with size, where using a model system comprised of particles on a smaller size scale is advantageous for making comparisons to even smaller molecular or atomic systems. In particular, polycrystalline colloidal systems containing dopant impurities, in the form of differently sized particles, are useful model systems for studying grain boundary segregation.

In addition, colloids provide an opportunity to discover emergent phenomena distinct from those occurring in traditional condensed matter systems. The exploration of soft matter driven away from equilibrium by various means has opened new possibilities to study and create systems in novel dynamic regimes. One possible result of studying nanoscale colloid dynamics is that the size of the particle becomes closer to that of the solvent molecules, which must rearrange to accommodate changes in the particle position. A regime where the timescale of this solvent rearrangement is closer to the timescale of particle motion has not been extensively explored.

An additional feature of electron microscopy imaging used in the experiments discussed here is the more perturbative electron irradiation used to generate contrast in the images. In this case, the electron beam can act as a driving force to introduce different processes, and has previously been used to drive particle assembly at the nanoscale, such as coarsening 2D defected solids [24]. Understanding the interaction between electron radiation and particle

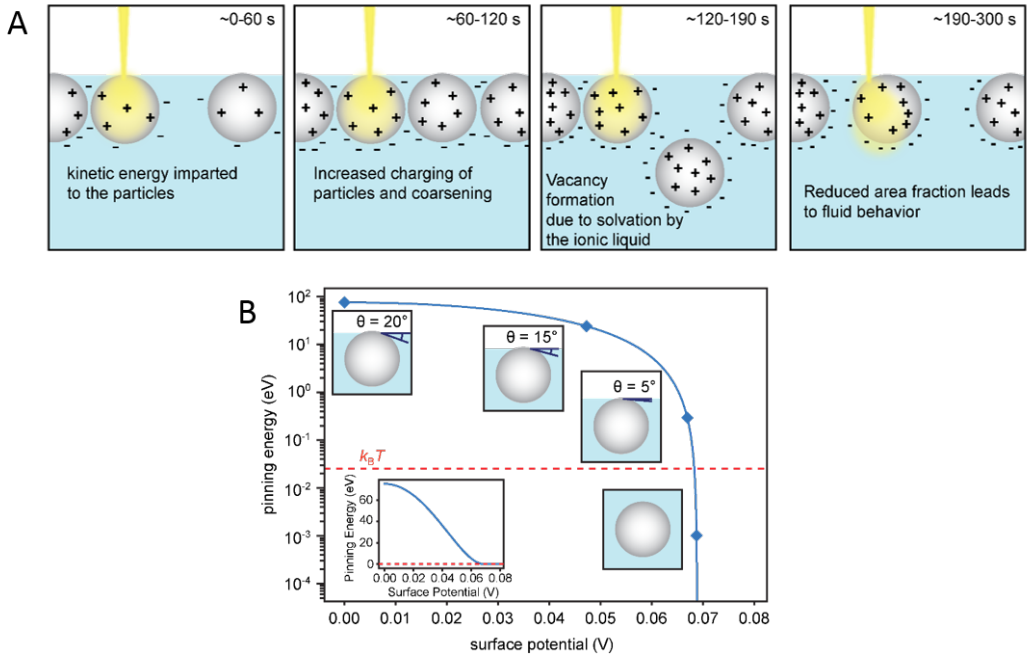

Figure 4.1: Schematic showing the response of a silica particle to electron beam perturbation at an ionic liquid-vacuum interface. (a) Schematic showing how electron beam perturbation charges a particle to induce coarsening and eventual sinking. (b) The decreasing pinning energy of the particle to the solvent-vacuum interface with increasing surface potential demonstrates that charged particles sink when the pinning energy, which quantifies the work required to move a particle from the interface into the solution, is of order k_BT (red dashed line). Adapted from Reference [24].

dynamics or assembly is interesting and not well understood.

4.1.1 Prior work

Previous work in our lab explored the effect of electron beam perturbation on a polycrystalline monolayer of silica nanoparticles pinned to the top interface of a low vapor pressure ionic liquid droplet. The electron beam was able to drive dynamics within the system [24]. Initially, the electron beam irradiation caused the particles to begin fluctuating in their positions in the lattice (Figure 4.1a). These fluctuations enabled the coarsening of the monolayer as the initial smaller grains were able to translate or re-orient to merge into larger grains.

The particles were initially mostly submerged in the ionic liquid, with a contact angle at zero charge of 15 to 20 degrees (Figure 4.1b). As charge accumulated inside the insulating particles, counterions from the ionic liquid were recruited to the particle surface to screen the charge, eventually covering the surface and resulting in the particle's desorption from

the ionic liquid interface, leaving vacancies in the lattice (Figure 4.1b). We discuss particle sinking in greater detail in Section 4.3.2. The buildup of particle vacancies caused a decrease in the area fraction of particles in the monolayer, inducing a melting transition. Here, we seek to expand our capability to control the assembly of colloidal monolayers and our understanding of how the electron beam drives colloidal monolayer dynamics, specifically in a system where the main polycrystalline lattice is comprised of 300 nm silica particles and additional larger 1 μm silica particles are interspersed in the crystal lattice. We define the main lattice particles as 300 nm diameter particles and dopants as the lower concentration 1μm diameter particles.

4.2 Colloidal monolayer assembly, imaging, and image analysis

4.2.1 Protocol for assembling doped colloidal monolayers

In these recent experiments, the silica particle monolayers form as the silica particles rise to the surface of a droplet containing ionic liquid (IL) and glycerol because their presence at the vacuum-IL interface reduces the free energy of the system [24]. The sample is prepared by mixing together the silica particles in aqueous solution, IL, and glycerol, subsequently dropcasting this solution onto a silicon substrate, and removing excess water by placing the sample in a vacuum chamber. This general overview is explained in more detail below.

Substrate cleaning

Silicon substrates are rinsed in acetone, isopropyl alcohol (IPA) and MilliQ water, dried with a stream of N_2 gas, and then visually inspected for any residue. If any contaminants remain, they can be wiped off using a foam tipped swab soaked in IPA, then re-rinsed with acetone, IPA, and MilliQ water, and dried again with N_2. Alternatively, substrates were cleaned by sonication while immersed in sequence in acetone, IPA, 2% Hellmanex detergent, and water for 10 minutes each, rinsed with MilliQ water, and dried with a stream of N_2 gas. Substrates are then further cleaned with a 2 minute O_2 plasma reactive ion etch.

Ionic liquid and glycerol handling

The ionic liquid 1-ethyl-3-methylimidazolium ethyl sulfate ($EMIM^+$ $EtSO_4^-$) is hygroscopic, so a number of protocols were used to control the hydration level of the samples. The ionic liquid used for these experiments was freshly purchased and stored in a glovebox. The ionic liquid was only removed from the glovebox in aliquots. The glycerol used in these experiments was similarly stored in the glovebox and only removed in small aliquots. Any samples containing ionic liquid or glycerol were also stored in the glovebox if not used immediately.

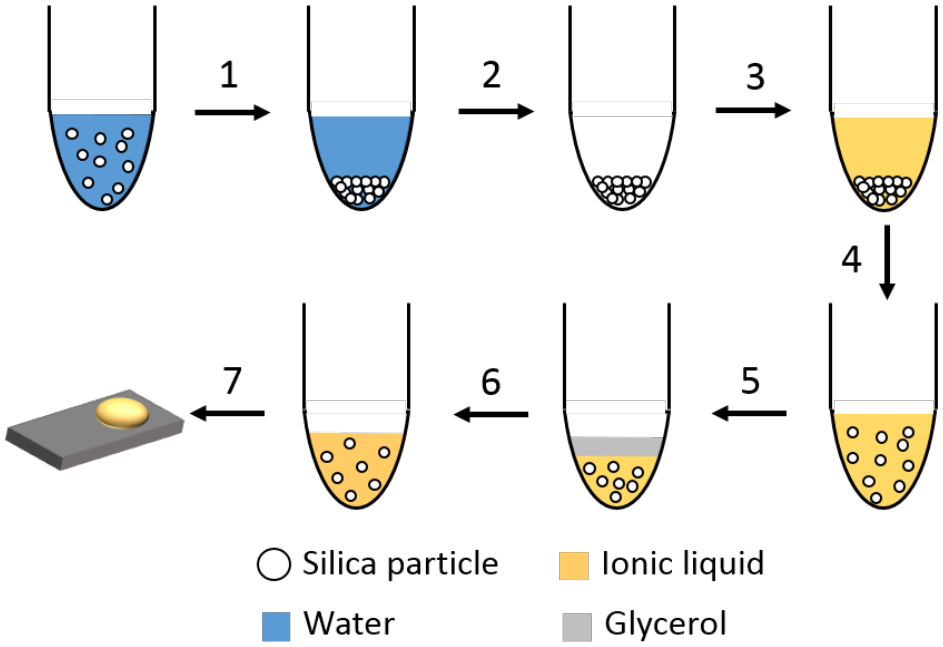

Figure 4.2: Schematic showing sample preparation for an interfacial colloidal monolayer (not to scale).

One source of difficulty in preparing these samples worth noting is the viscosity of the ionic liquid and glycerol, which both flow very slowly and therefore require care to ensure that the entire expected volume has been pulled into the micropipette tip before removing it from the solution. This is especially noticeable for smaller pipette tips with narrow entrance holes. For this reason, preparing larger volumes of samples than necessary (10s to 100s of μL to ultimately use less than 1 μL per sample) is convenient, such that small variations in volume measurement accuracy have a smaller overall impact in the final concentration of each component of the sample.

Silica particle solution preparation

To consistently form polycrystalline interfacial monolayers consisting of 300 nm diameter lattice particles and 1 μm diameter dopant particles, we experimented with multiple sample compositions with different concentrations of particles, IL, and glycerol. In what follows, we describe the standard protocol common to all of them for preparing the base mixture of particles in IL with the possible addition of glycerol. The stated volumes correspond to those used to prepare the 2:1 300 nm:1 μm, 75% IL 25% glycerol particle solution used for the primary datasets described in this chapter. The 2:1 ratio of 300 nm diameter lattice particles to 1 μm diameter dopant particles reflects the ratio of particles present in the

sample preparation solution but does not reflect the ratio of particles that comprise the final monolayer, which we discuss further in Section 4.2.2.

Silica particles were purchased in aqueous solution from Nanocomposix and transferred into $EMIM^+$ $EtSO_4^-$ as follows. Before measuring particles, the particle solution was mixed well by shaking the bottle, which was particularly important for achieving accurate particle concentrations, since the particles readily sink to the bottom of the solution. The volume containing the desired number of particles was measured using a micropipette and dispensed into a microcentrifuge tube (Figure 4.2, starting point). The solution was centrifuged at 7000 rpm for 2 minutes, until a visibly separated pellet of particles formed at the bottom (Figure 4.2, step 1). As much as possible of the supernatant was removed by pipetting away the top aqueous layer, avoiding removing any particles (Figure 4.2, step 2). If the volume of particles needed to produce the desired final number of particles exceeded the volume of the microcentrifuge tube, the process of centrifuging, removing supernatant, and then adding more particles was repeated until the pellet contained the concentrated particles from the required volume of the initial particle solution.

To make 200 μL of particle solution at a final concentration of 13 mg/mL of 300 nm particles and 250 mg/mL of 1 μm particles (corresponding to a 2:1 particle number ratio), we used 260 μL of 10 mg/mL 300 nm particles and 5 mL of 10 mg/mL 1 μm particles. To determine these particle quantities, we used the volume of a sphere of the expected diameter as $\frac{4}{3}\pi r^3$, where r is the radius of the sphere, and the density of silica, given by the manufacturer as 2.2 g/cm^3 [84], to calculate the number of particles per unit mass as 3.22×10^{10} 300 nm diameter particles per mg of silica and 8.68×10^{10} 1 μm diameter particles per mg of silica. Using this ratio, we found that a 2:1 particle ratio of 300 nm particles to 1 μm particles is a 1:18.5 weight ratio, corresponding to the 2.6 mg of 300 nm diameter silica particles and 50 mg of 1 μm particles used in the sample preparation.

The particles were next transferred into the IL. The $EMIM^+$ $EtSO_4^-$ was pipetted into the microcentrifuge tube (Figure 4.2, step 3) and the particles were suspended into the solution by slowly pulling the solution into and expelling it from the pipette tip, while avoiding forming bubbles (Figure 4.2, step 4). At this stage, the ionic liquid was viscous and the particles were densely packed together and prone to forming chunks, so resuspending slowly was optimal to avoid clogging the pipet tip. To achieve a final volume of 200 μL, IL was added until the total volume of the solution was around 170 to 180 μL, resuspended, and then additional IL was added until the final volume was 200 μL. These preparation conditions worked well for these particles, but for future samples, supernatant removal and resuspension could be optimized by producing a tighter or looser pellet by centrifuging at higher or lower speeds, respectively.

The final step in preparing the particles in IL solution was to remove any remaining water. We did this by heating the solution at 60 °C for an hour in a vacuum oven at roughing pressure to drive off remaining water. After the removal of water, this solution could be stored in the glovebox for future use and thoroughly mixed before subsequent use. The final volume of 200 μL was chosen for ease of performing the protocol. Volumes that are too small would result in a small particle pellet, which was more difficult to isolate from

the supernatant, and was also difficult to re-suspend by pipetting up and down with small volumes of IL. Larger volumes would require more time in the vacuum oven to remove the residual water.

For samples with mixtures of particles of different sizes, the particles could be mixed together initially or they could be prepared in separate IL solutions and then mixed together. Due to the viscosity of the final IL mixture, mixing the particles together when they were still in the aqueous solution appeared to yield more consistent mixing. However, mixing differently sized particles after they had been transferred to the IL was advantageous for testing many different particle size ratios, since it reduced the number of initial solutions to be prepared. Ultimately, the method of mixing the particles together while they were still in aqueous solution and subsequently transferring the particle mixture to the IL was used for the final experiments.

The $EMIM^+$ $EtSO_4^-$ particle suspension was then mixed with glycerol (Figure 4.2, step 5). For a 75% IL 25% glycerol solution, 15 μL of the prepared particle in IL solution was mixed with 5 μL of glycerol. Before measuring the particle solution, it was mixed again by pipetting the solution up and down to ensure that the particles had not settled to the bottom of the tube. The glycerol was added and the solution was mixed by pipetting up and down very thoroughly (Figure 4.2, step 6). To ensure that particles were well dispersed in solution and not clumped together, the solution was then sonicated for 10 minutes. The sample could also be stored in the glovebox after this stage for future use, but should be re-sonicated and mixed before subsequent uses.

Monolayer assembly

Once the particle/IL/glycerol solution had been prepared and the substrates had been cleaned, one could proceed to form the colloidal monolayer droplet on the substrate. The particle solution was mixed again by pipetting up and down at least twenty times just prior to deposition to ensure that the particles did not settle to the bottom of the microcentrifuge tube. The particle solution (0.3 μL) was pipetted onto the cleaned Si substrate, taking care to deposit the solution in a single droplet without smearing it sideways or introducing air bubbles (Figure 4.2, step 7). The substrate with the droplet was then immediately transferred to a vacuum chamber and pumped down to roughing pressure for 10 minutes, followed by 30 minutes at high vacuum pressure with a turbo pump for final water removal.

Sample transport to the scanning electron microscope

To ensure that the samples stayed dry after the final water removal in the wet lab, we used the following methods. After removal from the vacuum chamber, samples were immediately placed into a gel box, chosen to hold the sample in place without touching the top sample surface, and were brought into the glovebox. Inside the glovebox, the gel boxes were transferred into a vacuum nipple, keeping the top of the gel box facing directly up so as not to have the liquid sample drop slide off the substrate. The vacuum nipple was closed with the

samples inside of it so that the samples could be stored in a water-free atmosphere. The vacuum nipple was then brought out of the glovebox and was ready for transport to the SEM. Samples were typically prepared the day before imaging, but Section 4.3.1 below describes the *in-situ* observation of monolayer formation once droplets are set on the Si substrate.

Adaptations from previous assembly methods

The current protocol differs from the protocol employed in Reference [24] for making this system. The two notable differences are the water removal conditions and the addition of glycerol. In the previous version of this protocol, the aqueous particle solution and ionic liquid were mixed together and directly deposited onto the substrate, resulting in a droplet that still contained a relatively large volume of water. The only water removal step occurred at this stage, where the droplet on the substrate was placed in a different vacuum chamber at 40 mTorr. In that earlier version of the assembly, placing the sample in vacuum also resulted in a reduction in volume of the droplet, which may contribute to how the silica particles travel to and assemble at the surface. This mechanism would likely depend on the rate of water removal and the initial proportion of water present in the droplet. We find that the addition of glycerol and the removal of water before the droplet deposition yields ordered monolayers with more consistency than the previous protocol.

4.2.2 Sample Optimization

Glycerol concentration

The addition of glycerol to the ionic liquid solution is an important difference compared to the previous version of this sample preparation described in Reference [24], which contained only the ionic liquid and colloidal particles. Glycerol was added to diminish the screening of the charged particles (after electron beam exposure) by the ionic liquid, with the intention of prolonging the time that the particles remain at the surface of the ionic liquid droplet before sinking and in the imaging field of view. We also found that the addition of glycerol produced samples whose initial conditions were more consistently densely packed and polycrystalline. By contrast, samples prepared without glycerol under otherwise similar conditions often had different initial morphologies and a different response to the electron beam. Glycerol concentrations of 75%, 50%, 35%, 25%. 20%, 15%, 10%, 5%, and 0% were tested, with 25% glycerol yielding the most consistent sample formation behavior and electron beam response over several different sample duplicates and different imaging sessions. The use of a solution containing both glycerol and ionic liquid, although chosen to reduce the ionic liquid screening during the SEM experiment, also affects the formation of the colloidal monolayer. The presence of both ionic liquid ions and glycerol likely changes the interaction between the solvent and particles as well as the viscosity of the solution, and both of these are plausible reasons that glycerol influences the morphology of the lattice that is formed to be the initial condition for electron beam imaging.

Particle size mixtures

Here, we define the main lattice particles as 300 nm diameter particles and the dopant particles as 1 μm diameter particles. Various ratios of 300 nm diameter lattice particles and 1 μm diameter dopant particles were tested to produce colloidal lattices with good mixing between the particle sizes and a meaningful number of 1 μm diameter dopants. The final lattices have a substantial amount of heterogeneity in the number of dopants per field of view, ranging from areas where 1 μm dopants outnumber the 300 nm lattice particles to areas entirely without dopants (examples shown in Figure 4.10 initial time points). To facilitate the experiment, optimizing for a particle mixture that gave a large area of monolayer with one to tens of dopants per SEM field of view was desirable. A final particle mixture of two 300 nm lattice particles per one 1 μm dopant particle was used, although ratios close to this (5:2 or 3:2 ratios of 300 nm to 1 μm particles) also gave similar results. The number of dopants required in solution far exceeded the actual stoichiometric ratio apparent in even the most densely doped regions of the sample, possibly due to the fact that the larger particles may diffuse more slowly and have less probability of finding the surface of the droplet during the monolayer formation process [85].

Total particle concentration

The total particle concentration in the liquid droplet also plays a role in the formation of the monolayer. We find that with increasing particle concentrations, the monolayer forms more consistently and generally occupies a larger area of the droplet surface. This concentration far exceeds the number of particles that would be required to cover the surface of the droplet and suggests that more of the particles sink to the bottom of the droplet than find the top surface. While stable monolayers can form with lower particle concentrations, the higher concentrations yield more reproducible results. Undoped monolayers were tested with an initial concentration of 10 mg/mL, 20 mg/mL and 50 mg/mL, with 50 mg/mL producing the most consistent polycrystalline monolayers. Doped monolayers were tested at a lower concentration of 1.3 mg/mL 300 nm particles and 25 mg/mL 1 μm particles and a tenfold higher concentration of 13 mg/mL 300 nm particles and 250 mg/mL 1 μm particles, where the latter also produced the more consistent monolayers.

Controls

Due to the sensitive nature of these samples and the inherent variation from sample to sample, we implemented a variety of controls to ensure reproducible results. We verified that the time between sample preparation and imaging did not change the behavior of the sample. We also confirmed that our protocol for removing excess water from the commercial IL is sufficient by comparing to a sample that was heated under vacuum for two days and found no difference in the final sample. We tested the duration of the final removal of water from the dropcast sample and found no large differences when leaving the samples in the vacuum chamber for longer, demonstrating that this step is sufficient for removing as much

remaining water as possible. Additionally, we compared samples stored in a moisture-free environment to samples stored at ambient atmospheric conditions to confirm that the sample response to the electron beam does change based on its environmental exposure to moisture.

Additional methods for future monolayer assembly

Some development that may provide inspiration for further experiments includes changing the nature of the sample or the preparation method. One sample parameter that could be tried more extensively is the type of ionic liquid used. There is a large variety of ionic liquids available that may interact with the particles differently, possibly uncovering different types of dynamics to explore. We tried preparing samples with $EMIM^+$ $MeSO_4^-$, and found inconsistent results. The sample preparation method also has additional room for exploration. We found that blotting the top of the droplet with a large flat surface, such as a piece of waxed weighing paper, produced very large crystalline domains in undoped samples which also dispersed very quickly upon electron beam exposure. This could be a promising avenue for manipulating the lattices into other desirable morphologies.

4.2.3 Imaging

Imaging this system requires unique considerations because the electron beam acts both as the driving force for the dynamics as well as the method for imaging them. Therefore, electron beam exposure needed to be carefully managed while imaging these samples. To avoid unnecessary electron beam exposure before the experiment begins, the microscope is focused on one area of the sample, the electron beam is blanked, and the sample is translated to a fresh area of the sample that will also be in focus before the imaging begins. Additionally, between experiments the electron beam is blanked and the sample is translated to avoid collecting data from areas adjacent to previously exposed areas. To control for changes in droplet curvature, imaging was performed in the center of the droplet.

The imaging conditions are another essential aspect of managing the electron beam exposure. Magnification, pixel size, pixel array size, and pixel dwell time were chosen to optimize time resolution while allowing for images with sufficient contrast to perform the particle detection analysis described in Section 4.2.4. To achieve this balance, we needed to consider that the electron beam is perturbative: too much electron beam exposure drives the dynamics too quickly to capture, but the electron beam is also the method for imaging, so insufficient electron beam exposure produces images without enough contrast to analyze the particles. Using the InLens detector of the SEM provided better contrast compared to the SE detector, possibly because the collection geometry is more favorable to electrons exiting vertically from the sample. Ultimately, the optimal balance was achieved using electron beam parameters of 6 kV and 60 pA current, imaging parameters of 7000× magnification and 396 × 396 pixels for a pixel width of 40.2 nm and a full imaging field of view of 15.9 μm, and scanning parameters of 2 μs/pixel resulting in frame times of 313 ms/frame. Movies were recorded in a Zeiss Gemini Supra 55 VP-SEM using a custom software built on the

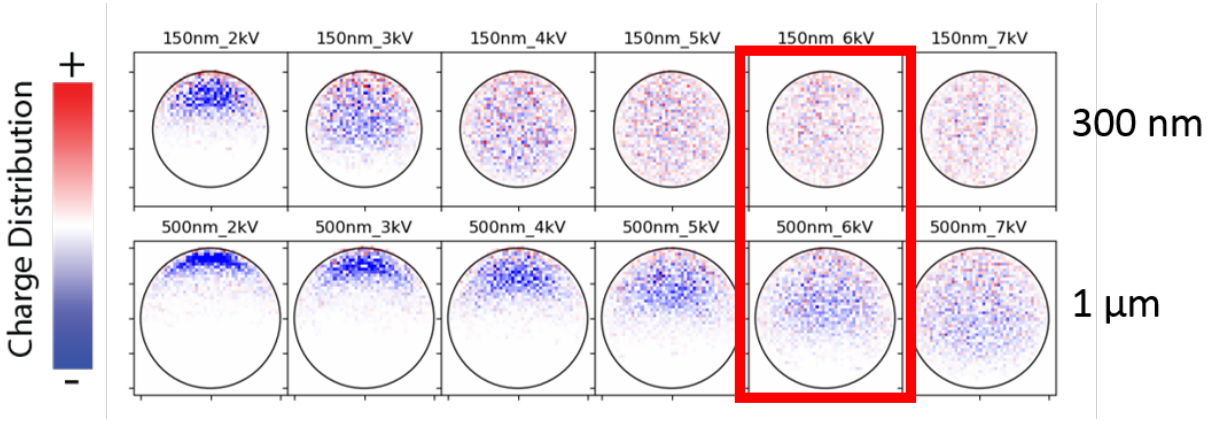

Figure 4.3: CASINO simulations of charge accumulation in particles at different voltages. Note that the net charge accumulation depends not only on the beam flux but also on the beam transmission through the bottom surface of the particle, which occurs far less in the larger 1 μm dopant particles than in the smaller 300 nm lattice particles.

ScopeFoundry platform developed by Ed Barnard, Shaul Aloni, and Frank Ogletree at the Molecular Foundry.

We arrived at these parameters using the following approach. Our aim was to slow down the dynamics as much as possible so that the evolution could be captured by more total frames, providing as much information as possible about how particle positions evolve with time. In other words, we wanted to optimize all parameters to prevent undersampling of events such as particle position fluctuations or translations. Because the electron beam interaction drives the dynamics, we use the lowest beam current possible that still allows us to clearly distinguish and detect the particles, which is 60 pA in this case. To optimize the accelerating voltage, we note that increasing the accelerating voltage leads to charge being deposited deeper into the sample. This effect can be simulated using CASINO, an electron scattering Monte Carlo simulation described in Reference [19], for particles of different diameters and accelerating voltages (Figures 4.3, 4.4). At lower accelerating voltages, more of the charge is therefore deposited at the surface, i.e., in the silica beads rather than in the bulk solution, which therefore accumulate charge faster and disperse more quickly [24]. Therefore, up to a certain point, higher accelerating voltages are desirable for extending the duration over which we can observe the system evolve. However, at higher accelerating voltages, two detrimental effects emerge. First, with the electrons being deposited further into the system, fewer secondary electrons escape from the sample to be detected and proportionally more of the volume that is irradiated by the electron beam is the bulk IL that is beneath the silica particles, indicated by the increase in the transmitted fraction of primary electrons with increasing accelerating voltage (Figure 4.4). This leads to reduced imaging contrast of the interfacial silica particles at higher accelerating voltages. Second, the ionic liquid is

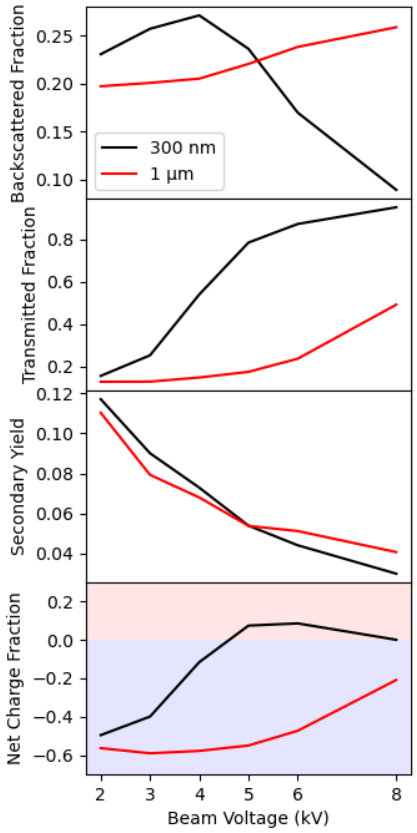

Figure 4.4: Plots showing the results of CASINO simulations for electron trajectories and charge accumulation shown in Figure 4.3. The backscattered fraction indicates the percent of electrons that exit the particle in the top direction (moving back towards the direction of the electron beam excitation). The transmitted fraction indicates the percentage of electrons that exit the particle by penetrating through it (moving in the same direction as the electron beam excitation). The secondary yield is the number of secondary electrons generated during the scattering simulation. The net charge fraction is the combination of the trapped primary electrons, which contribute a negative charge, and secondary yield, which contributes a positive charge.

not fully impervious to the electron beam. With more charge being deposited into the bulk ionic liquid, we observe the emergence of visible ionic liquid damage, possibly caused by electron beam catalyzed cross-linking, which appears as dark contrast in the SE images [86, 87]. After testing accelerating voltages from 2 kV to 10 kV in 1 kV increments, we found that 6 kV was a good balance between the relative advantages of low and high accelerating voltages (Figure 4.3, red box).

Next, we selected a magnification of 7000× to achieve a field of view that would encompass a few large grains in the polycrystalline lattice while having high enough magnification to clearly resolve individual particles. Then we optimized the time resolution, where the number of frames per second is determined by the combination of the number of pixels per scan and the pixel dwell time. We tested pixel counts ranging from 1064 × 1064 to 200 × 200 and pixel dwell times ranging from 10 μs to 1.5 μs. With too few pixels, the particles cannot be clearly distinguished from each other but too many pixels give redundant information at the expense of time resolution. Similarly, with insufficient pixel dwell time, the signal is noisy and particles become difficult to distinguish, but increased pixel dwell times give diminishing returns in image clarity. We found that the combination of 396 × 396 pixels and 2 μs/pixel was sufficient for compatibility with the analysis described in Section 4.2.4, which sums frames in sets of two, to reliably assign particle positions.

An important aspect of the imaging concerns the sensitivity of the sample to its environment. We find that with prolonged exposure to the vacuum environment inside the SEM, the samples begin to respond differently to electron beam perturbation, specifically by dispersing much more quickly. The time of this transition varies from day to day, but typically occurs on the timescale of 45 minutes to 2 hours. Samples that have been loaded into the SEM vacuum chamber at the same time undergo this transition at roughly the same time, regardless of conditions like total electron beam exposure. We speculate that because this happens to all of the samples inside the vacuum chamber, that this is not an effect of imaging but rather the sample environment. Since the samples are exposed to the ambient atmosphere while they are mounted to the sample stage and loaded into the vacuum chamber, the possibility of the hygroscopic ionic liquid absorbing ambient humidity and then progressively releasing the water inside the vacuum chamber is one possible contribution to this transition. Another possible contribution is the buildup of carbonized material as a byproduct from the interaction between the electron beam and the IL and glycerol sample during imaging. Experimentally, we addressed this slow change by only using data from samples that have not yet undergone this transition. We used separate vacuum nipples to store and transport the samples so that we had several fresh samples available for each imaging session.

4.2.4 Image analysis

Particle detection and tracking

To quantitatively analyze the dynamics of the particles within the monolayer, we must be able to detect them in an image and follow them from frame to frame. First, HDF5 files from

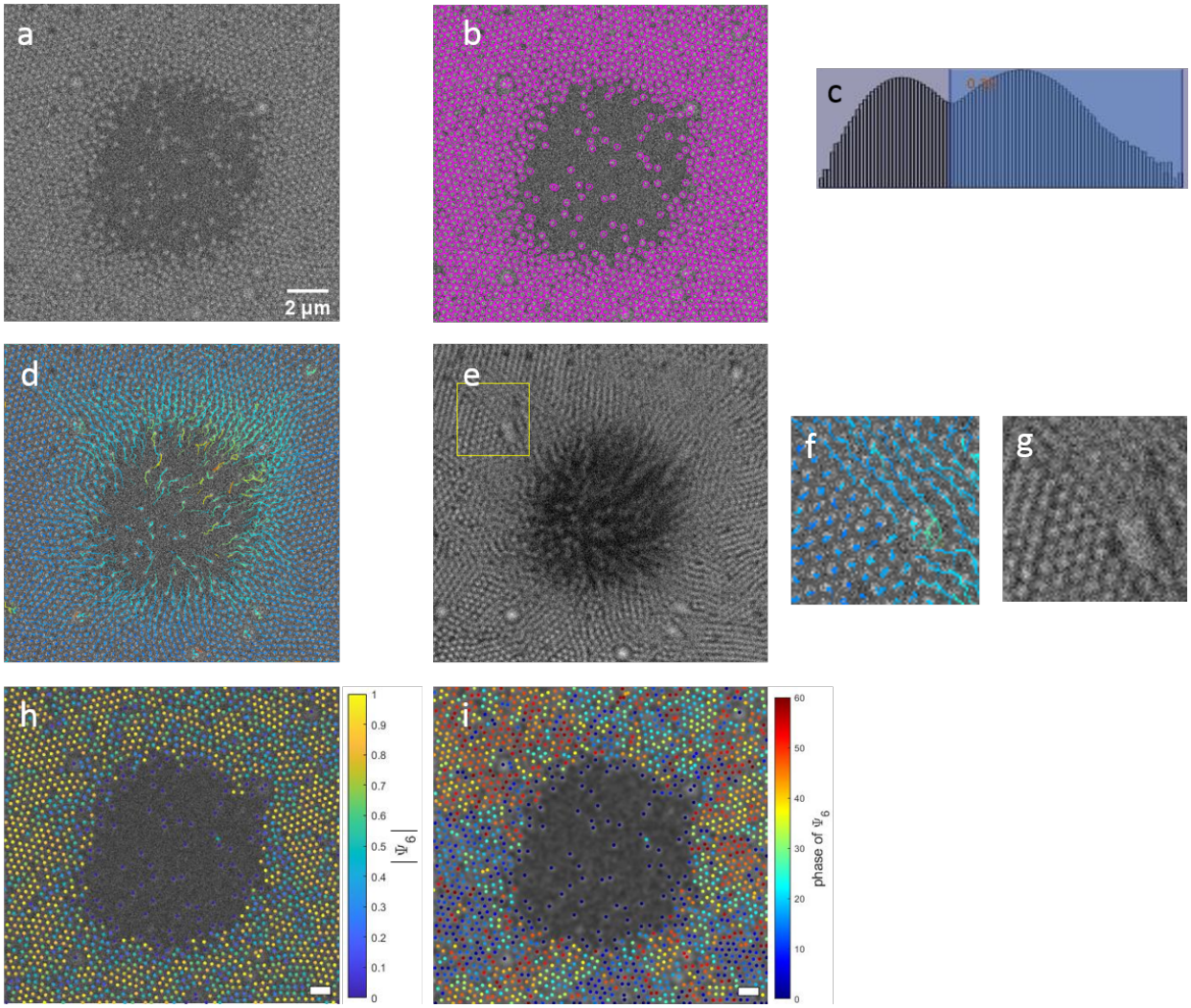

Figure 4.5: Lattice particle detection and tracking shown on an example image frame. (a) InLens data averaged over two frames. (b) Detected particles overlaid in magenta circles. (c) Histogram of mean particle intensity used to filter particle assignments. (d) Particle tracks overlaid in false color corresponding to mean particle velocity, where blue corresponds to a slower velocity and red corresponds to a faster velocity. (e) Fifteen frames averaged to show particle motion, with region for comparison indicated in yellow. (f,g) Zoomed-in comparison of (d) and (e) respectively. (h) Map of the bond order parameter magnitude. (i) Map of the bond order phase.

the microscope were restructured to be compatible with the ImageJ HDF5 importer using Matlab. To achieve better contrast, we add together frames in sets of two (Figure 4.5a), for a time resolution of 626 ms/frame. We then use the TrackMate plugin in ImageJ to perform both the particle detection and tracking. The parameters for the Laplacian of Gaussian detector for particle detection using TrackMate were a blob diameter of 0.28 μm, to account for the apparent reduced width due to the particles being mostly submerged in the IL and a threshold of 0 (Figure 4.5b). We then removed spurious particle detection in the bare spots of the monolayer by using the median intensity of the pixels within the detected spot to construct a histogram with two peaks corresponding to higher intensity (real particles) and lower intensity (spurious particles), and selecting a cutoff at the lowest point in the histogram between the high and low peaks (Figure 4.5c, cutoff indicated by blue shading). Another false positive can occur when the algorithm incorrectly assigns the 1 μm dopant particles as a few 300 nm particles. For preliminary analysis, these were not removed, since they comprise a very small portion of the total number of particles, but they can be manually removed. At this stage, we also removed "particles" detected at the edge of the frame corresponding to imaging artifacts due to the scanning response. For particle tracking, we used the built in "Simple LAP tracker" in TrackMate, with a linking max distance of 0.250 μm, a gap-closing maximum distance of 0.1 μm, and a gap-closing frame gap of 1. TrackMate was used to visualize the generated tracks and generate videos of the tracks overlaid onto the particle movies (Figure 4.5d).

Another method that was utilized for visualizing areas of enhanced particle motion is to add frames together in large sets. Particles that are relatively stationary will appear as single spots while particles that move over the duration of the averaged frames will appear as streaks. The number of frames was adjusted based on the extent of particle motion, with a typical set of 15 frames used for these samples and imaging conditions (Figure 4.5e). The frame averaging method is advantageous for quickly assessing bulk particle motion, since the frame averaging method is much less computationally complicated than the particle detection and linking used in TrackMate. Additionally, using an analysis method that does not use particle detection or tracking allows us to directly compare the output to the TrackMate analysis to qualitatively verify the accuracy of our particle tracking. Between the two methods, areas generally showed the same magnitude and direction of particle motion, confirming that the TrackMate linking method is generally accurate (Figure 4.5 f,g). However, the TrackMate analysis provides particle-level information that is needed for more extensive analysis. For the more extensive analysis, output files from TrackMate were loaded into a custom Matlab code. The custom Matlab code was used to compute the bond order parameter magnitude and phase, defined at the end of this section.

Detecting and tracking the dopants is a desirable analysis capability for calculating any correlations between the positions of the lattice particles and dopants. The same TrackMate ImageJ plugin can be used to track the dopants with some modifications, albeit with more user input (Figure 4.6). A Gaussian filter with a radius of 1.2 was applied to the data before loading into TrackMate. An estimated blob diameter of 0.75 μm was used to initially assign particle locations, with were then filtered using the total intensity and spot quality, manually

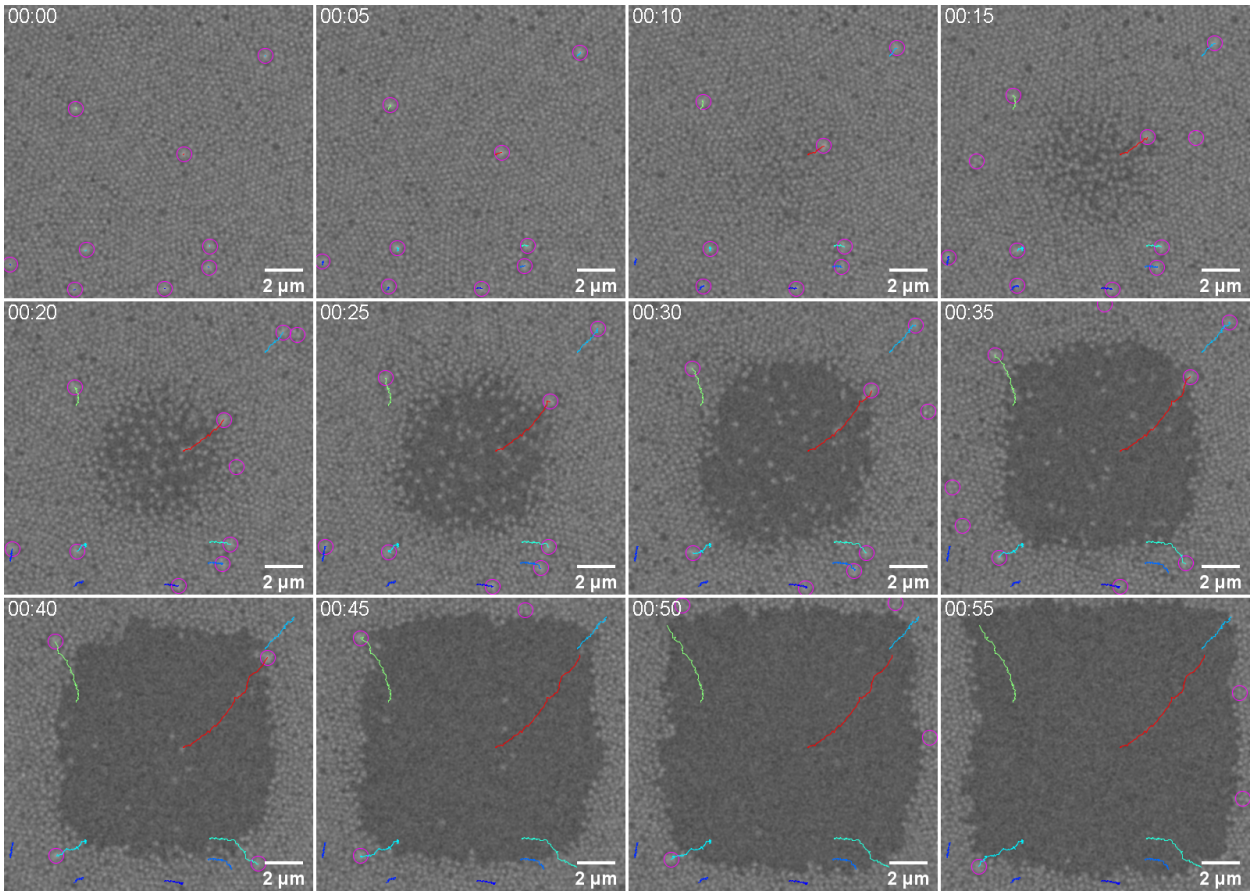

Figure 4.6: Frames of a movie showing dopant tracking. Dopants are circled in magenta and tracks are indicated by colored curves.

choosing the threshold for excluded points until only the dopants were positively identified, with the minimal number of falsely identified dopants present. Tracking was then done with the Simple LAP tracker with a linking max distance of 0.75 μm, a gap-closing maximum distance of 0.2 μm and a maximum frame gap of 2. Incorrectly identified dopants typically occur randomly and can be filtered out by selecting for particles with track lengths greater than two frames.

Bond order parameter phase and magnitude calculation

We use the bond order parameter magnitude and phase to quantify the crystallinity of individual particles with respect to the orientation and position of their nearest neighbors. We define the bond order parameter as $\Psi_{6,j} = \frac{1}{N_{nn}} \sum_{k=1}^{N_{nn}} e^{6i\theta_{j,k}}$, where N_{nn} is the number of neighboring particles within 0.4 μm and $\theta_{j,k}$ is the angle between the bond vector connecting

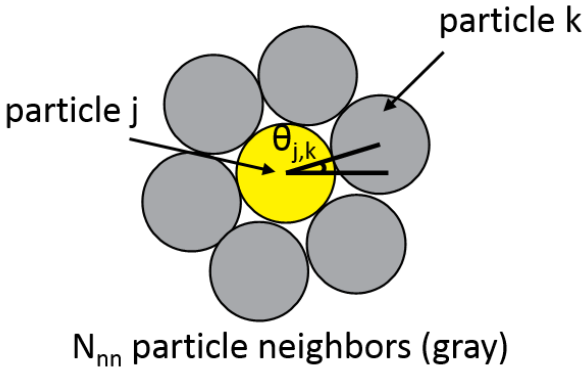

Figure 4.7: Diagram defining bond order parameter variables.

the particle j and the neighboring particle k and the horizontal reference (Figure 4.7). The magnitude, which ranges from 0 to 1, describes the local order of the particle. The phase, which ranges from 0 degrees to 60 degrees for a hexagonal lattice, describes the orientation of the crystalline region that the particle is in. To aid in interpreting the local order and orientation of particles in the monolayers, we generate false color maps corresponding to the bond order parameter magnitude and phase, respectively (Figure 4.5 h,i).

4.3 Electron beam induced dispersal of doped interfacial colloidal monolayers

4.3.1 Formation of colloidal monolayers

We find that we are able to consistently produce polycrystalline colloidal monolayers with dopants interspersed in the lattice, with a positive correlation between the position of the dopants and the position of disordered interfaces. By depositing the ionic liquid, glycerol, and particle solution onto a substrate immediately before imaging, we are able to observe the formation of this monolayer on a macroscopic scale (Figure 4.8) by using the high vacuum of the SEM chamber in place of the final vacuum stage of the typical sample preparation protocol (Section 4.2.1). We observe that particle density initially builds up in a ring (lighter contrast) midway between the center and the edge of the liquid droplet. The ring gradually expands in width over the course of an hour, until it has expanded to completely fill in the center of the droplet. Before the surface of the droplet has reached a steady coverage, the lattice at the surface of the droplet already has the same polycrystalline order as a typical fully formed lattice. This insight was enabled by the newly developed protocol for the monolayers (4.2.1), where the monolayer is assembled from a solution containing only particles, IL, and glycerol, which are both vacuum compatible liquids (4.2, step 7). In

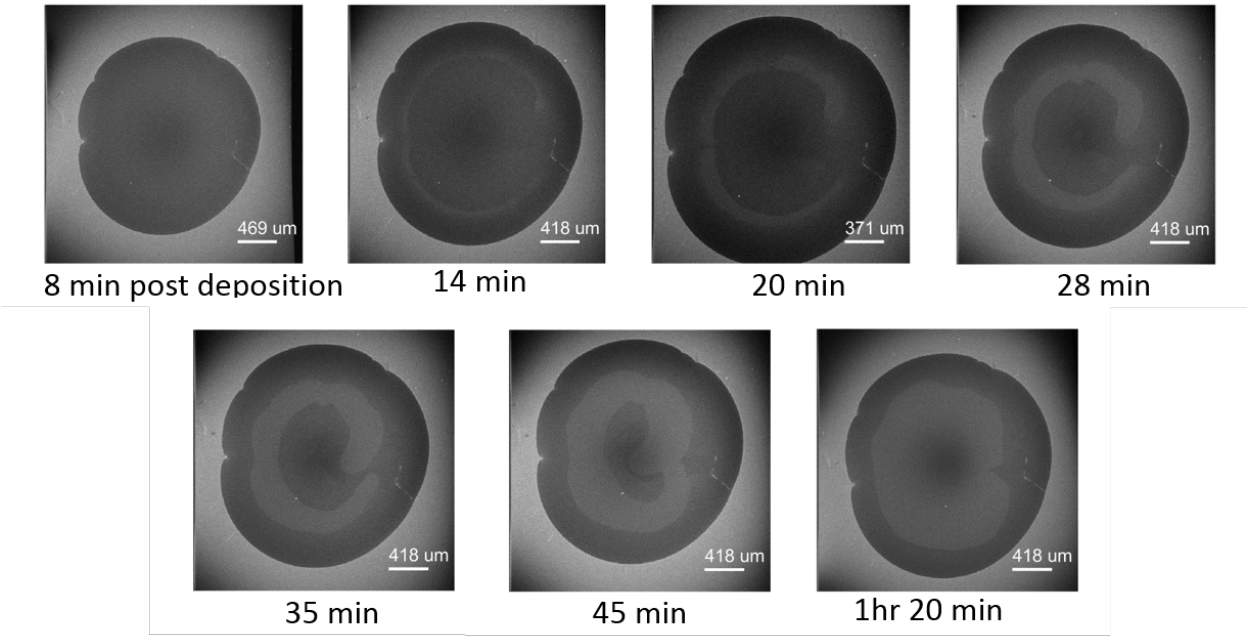

Figure 4.8: Images showing progression of monolayer assembly over time. SE images recorded at 6 kV.

previous work, the monolayer lattice was assembled from a solution containing particles, IL, and water, where monolayer assembly occurred at the same time as the removal of the water [24]. Because the water removal step is incompatible with measuring the sample inside the SEM vacuum chamber, the monolayer assembly could not previously be directly observed with the SEM.

4.3.2 Response to electron beam perturbation

The particles in the monolayer are initially static and have reached a stationary configuration during the overnight wait time between the monolayer assembly and the measurement. The particles begin to move in response to electron beam exposure within the first one or two frames, where the electron beam direction is normal to the direction of particle motion. To control the electron beam exposure such that each measurement begins with a static lattice, we electrostatically blank the electron beam between measurements and move the imaging area to avoid previously exposed areas, as described in Section 4.2.4.

With electron beam exposure, the particles in the lattice always follow the following pattern, regardless the number of 1 μm diameter dopants in the frame (Figure 4.9). First, the particle density in the center of the frame decreases. The central area of reduced density expands and particles begin to flow away from the center of the frame. Eventually, a bare

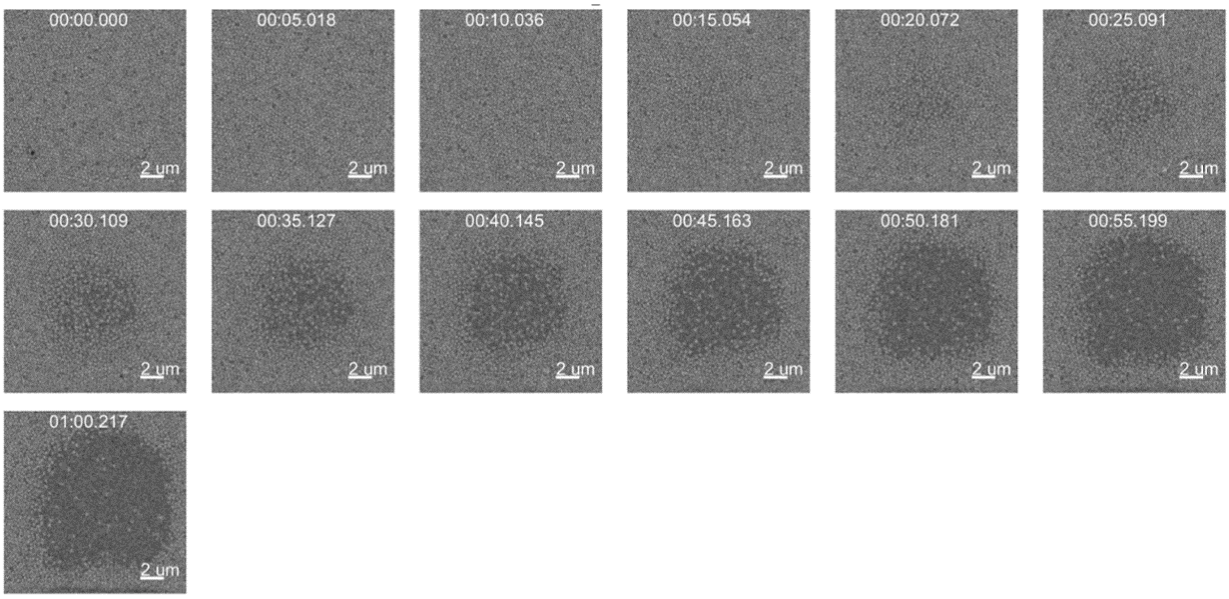

Figure 4.9: Frames from a movie showing response of monolayer to electron beam perturbation.

area forms in the center of the frame, and a higher density of particles forms around the edge of the frame. The exact width of this high density border can vary from experiment to experiment. The formation of the bare patch is typically centered in the field of view but can form off center as well if the initial particle density loss occurs off-center, speculatively due to some random fluctuation in particle density that causes the initial loss in density to occur there.

To explain the loss in particle density, we consider two ways that the particles can leave the imaging field of view. The particles can either sink into the bulk liquid or they can translate laterally out of the field of view. In these experiments, we observe instances of both cases. We expect particle sinking to be a two stage process, where particles are first de-pinned from the interface and subsequently sink to the bottom of the IL/glycerol droplet. Initially, uncharged particles are pinned to the vacuum-IL/glycerol interface to minimize free energy. Moving an uncharged particle from this interface into the bulk solution has an energy penalty on the order of 25 eV, which we assign as the pinning energy [24]. As the silica particles are irradiated by the electron beam, they accumulate charge, and the increased surface potential stabilizes the particle-IL interaction and destabilizes the particle-vacuum interaction, reducing the pinning energy. This results in more IL counterions covering the particle surface until the particle is no longer pinned to the interface. With the charged particle submerged in the ionic liquid, we next consider the effect of gravity by approximating the gravitational potential energy as mgh, where m is the mass of a single colloidal particle,

g is the gravitational constant, and h is the height of the ionic liquid/glycerol droplet. We calculate the mass of the particles to be 3.11×10^{-14} g for a 300 nm lattice particle and 1.15×10^{-12} g for a 1 μm dopant particle, using a density of 2.2 g/cm^3 and the volume of a sphere, $\frac{4}{3}\pi r^3$, where r is the radius of the particle. The height of the droplet is approximated to be 30 μm by taking the difference in the working distance of the electron beam focused on the top of the IL/glycerol droplet compared to the working distance of the electron beam focused on the substrate. Using these values, the gravitational potential energy of a 300 nm lattice particle is 0.057 eV and is 2.1 eV for a 1 μm dopant particle. These energies are much lower than the 25 eV pinning energy for a neutral particle, which is consistent with the observation that the uncharged particles populate the top interface of the droplet. However, when the particles accumulate charge and become submerged, the contribution of the pinning energy decreases and gravitational energy dominates, resulting in the particles sinking into the IL/glycerol droplet. Alternately, the density of the silica particles, 2.2 g/cm^3 [84] is greater than that of the ionic liquid (1.24 g/cm^3 [88]) or glycerol (1.26 g/cm^3 [89]), so a fully submerged particle is expected to sink. In our group's previous work, particle sinking rate was found to be independent of position within the imaged area [24], so we do not attribute the preferential loss in density at the center solely to particle sinking.

To explain the two observations that the center undergoes the decrease in density first and that particles remain at the border of the frame, we speculate that this effect is caused by the geometry of the imaging field of view. As the electron beam interacts with the sample, potential energy is built up in the system in the form of charge from the electron beam accumulating in the silica particles, which are insulators. Calculations suggest that this energy is not thermal, i.e. the electron beam hardly elevates the temperature of the monolayer, although the extent to which this energy is electrostatic is at least to a great extent mitigated by IL screening [24]. Areas near the edge of the field of view have a bath of unexposed sample nearby in which to deposit that energy, whereas areas in the center of the field of view are bounded on all sides by areas also exposed to the electron beam. This circumstance builds up a gradient in potential energy that is highest in the center of the field of view. In response to this gradient, the particles or the underlying solution could move outwards towards the area of lower energy deposition, leading to an outward flow that results in an overall lower particle density in the center of the field of view.

Within this framework for lattice dynamics, the number of dopants present in the lattice changes the lattice's response to electron beam perturbation. With more dopants, the decrease in particle density proceeds more quickly (Figure 4.10). In lattices with more dopants, the initial loss in particle density appears earlier compared to lattices with fewer dopants and the overall decrease in particle density then occurs progressively more quickly. This can be quantified by using the particle tracking data to plot the area fraction of 300 nm diameter lattice particles, which decreases more quickly at higher dopant concentrations (Figure 4.11). This decrease in density is correlated to a decrease in the magnitude of the bond order parameter, consistent with the loss of crystalline order that accompanies the decrease in particle density.

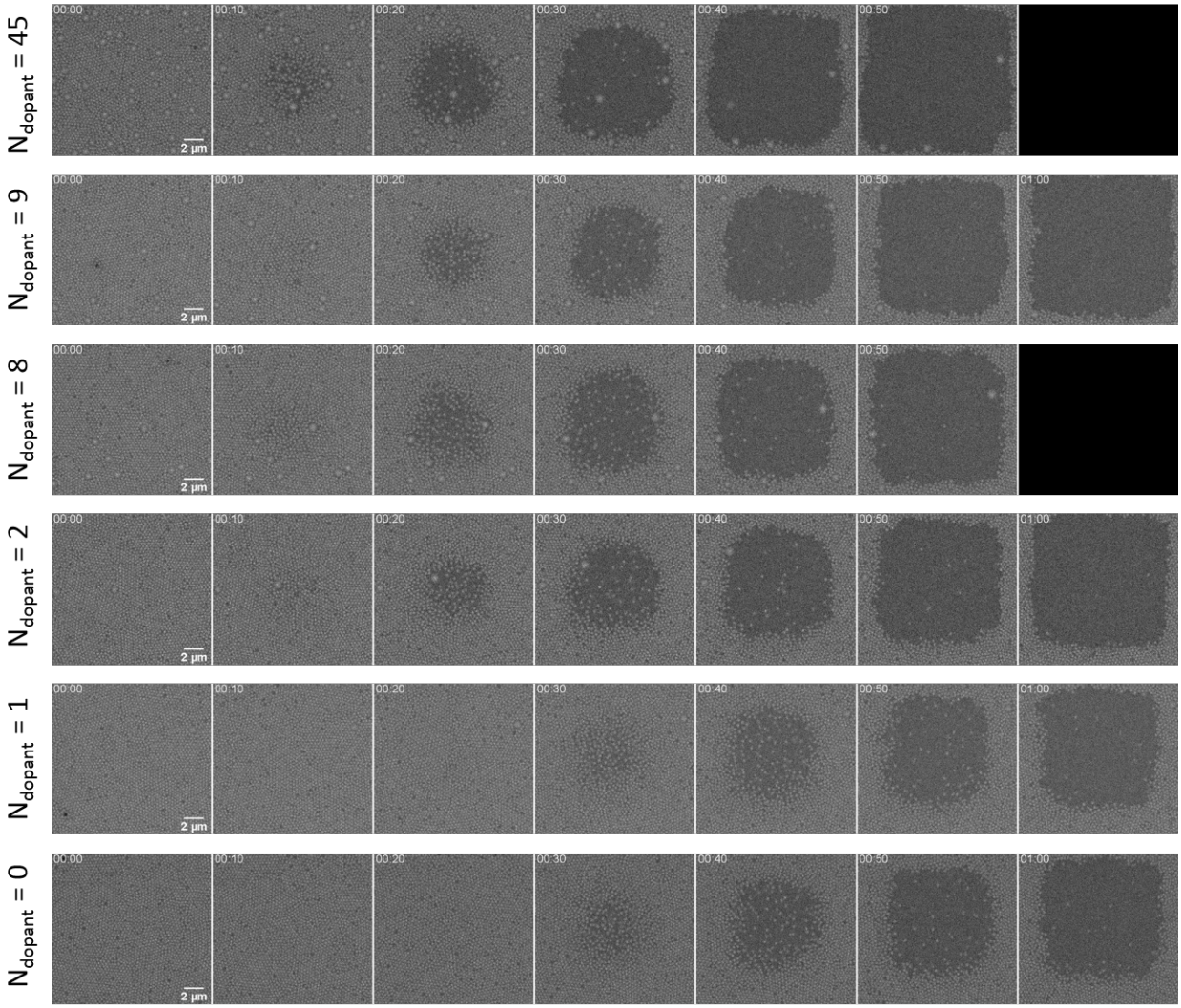

Figure 4.10: Frames from movies showing response of monolayer to electron beam perturbation at different dopant concentrations. Frames are spaced every 10 seconds with black frames corresponding to time points where no data was recorded.

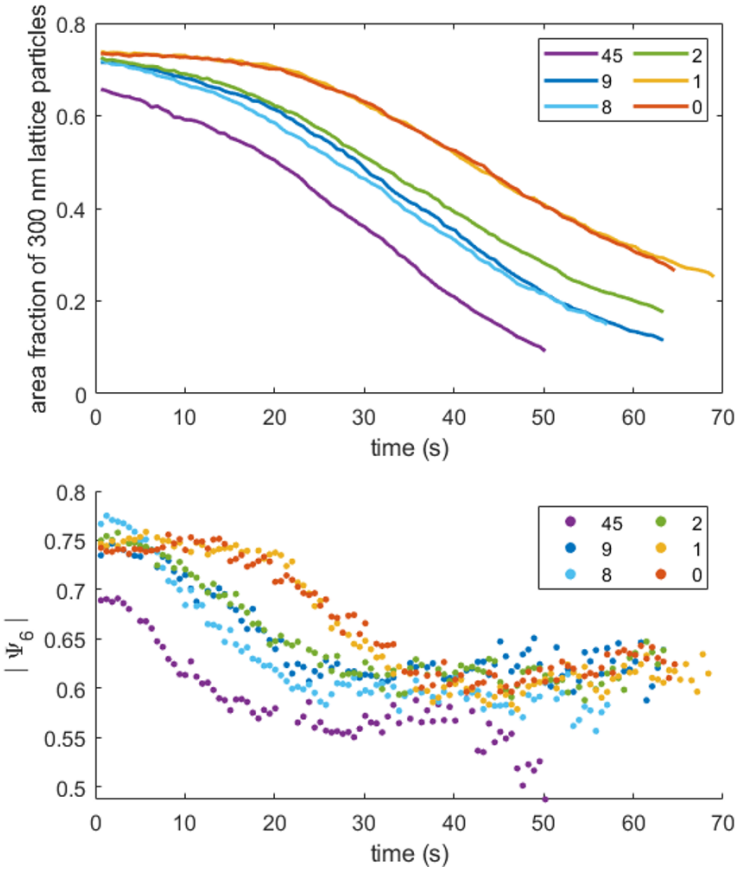

Figure 4.11: Plots of the area fraction of particles and bond order parameter magnitude for different dopant concentrations shown in Figure 4.10.

4.3.3 Lattice polycrystallinity does not appear strongly correlated to dopant concentration

To further analyze the evolution of the colloidal monolayer with changing dopant concentration, we examine the crystal grain orientation of the 300 nm diameter particle lattice relative to the positions of the 1 μm diameter dopants. We calculate the Ψ_6 phase for each particle and use it to generate a false color map in which crystal grains are clusters of similarly colored particles with similar orientations (Figure 4.12). The positions of the 1 μm dopants are marked with pink circles. In all dopant number cases, the starting lattice is similarly polycrystalline, comprised of a few large crystal grains and other less ordered areas. With continued electron beam exposure, the particle density and crystalline order in the center of the field of view decrease. The dopants primarily move towards the edge of the field of view and occasionally sink into the bulk liquid droplet. The position of the dopants appears

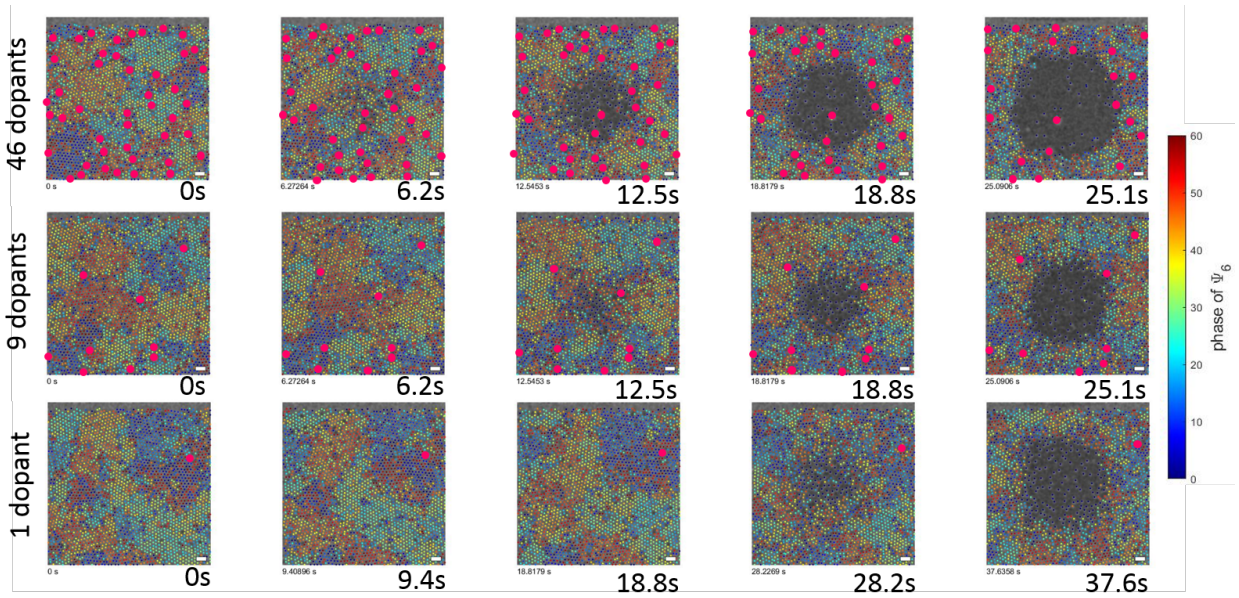

Figure 4.12: False color maps of crystal grain orientation and dopant position (pink circles).

to be correlated with the position of disordered particles between crystal grains. Because the size of a 1μm dopant is not commensurate with a given number of close-packed 300 nm lattice particles, the fact that the dopants do not exist inside perfect crystal grains is not necessarily surprising. Nevertheless, with the time resolution currently available for imaging the formation of the monolayer, whether the dopants migrate to the disordered interfaces between crystal grains or the presence of a dopant promotes formation of a disordered interface around it is unknown.

In addition, we find that the number of dopants does not strongly affect the polycrystallinity of the initial monolayer, prior to electron beam exposure (Figure 4.13). Using $|\Psi_6|$ magnitude to determine the local order surrounding a given lattice particle, we designate lattice particles as ordered ($|\Psi_6| \geq 0.7$, blue) or disordered ($|\Psi_6| < 0.7$, yellow). We calculate the particle's order using an average of the first four frames for improved particle localization and generate a false color map showing regions of order and disorder, with dopant particle locations shown in maroon (Figure 4.13, left). Comparing the number fraction of ordered and disordered particles, we do not find a clear trend with changing dopant number (Figure 4.13, right). With this analysis, we suggest that the degree of polycrystallinity present in the initial monolayer lattice is not dependent on the dopant concentration.

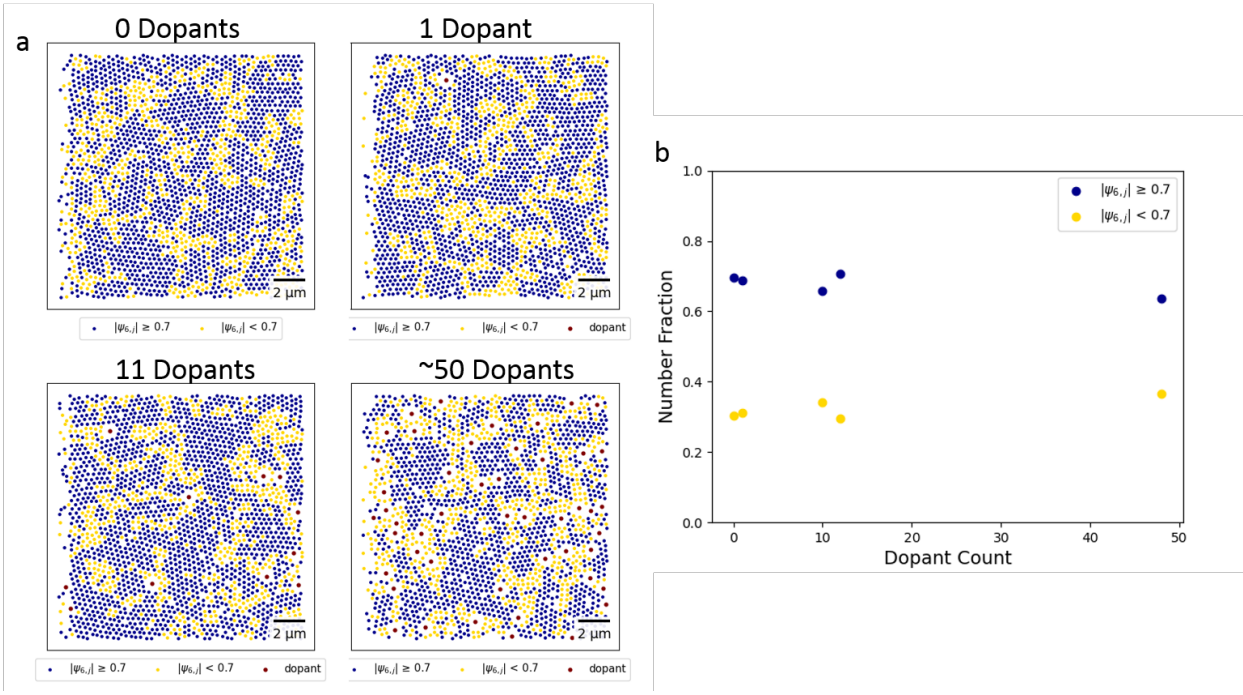

Figure 4.13: Visualization of unchanging lattice order with changing dopant concentration. (a) False color maps of $|\Psi_6|$ with varying dopant concentration, with ordered particles assigned to $|\Psi_6| \geq 0.7$ in blue and disordered particles assigned to $|\Psi_6| < 0.7$ in yellow. (b) Plot of number fraction of ordered ($|\Psi_6| \geq 0.7$, blue) and disordered ($|\Psi_6| < 0.7$, yellow) particles with respect to dopant count.

4.3.4 Lattice particle motion does not appear strongly correlated to dopant presence

We also visualize the trajectories of the 300 nm diameter lattice particles to map how the 300 nm diameter lattice particles respond to the electron beam perturbation (Figure 4.14). We overlay the trajectory path of up to the previous 15 particle positions, with trajectories colored according to the mean particle velocity over the course of the 15 frames. False particle assignments on dopant locations were not removed and incorrectly appear as clusters of short lived, fast moving trajectories. We observe that particles move outwards from the center of the field of view. Longer trajectories, indicating more particle motion, appear earlier in the center of the field of view compared to the edge. Trajectories sometimes align with with lattice planes, suggesting that concerted motion of particles is possible. The length of trajectories is not uniform across all areas of the lattice. Some areas of lattice particles are more stationary, visualized as shorter trajectories, while other areas are more mobile, and have longer trajectories. There is no visually apparent correlation between the mean

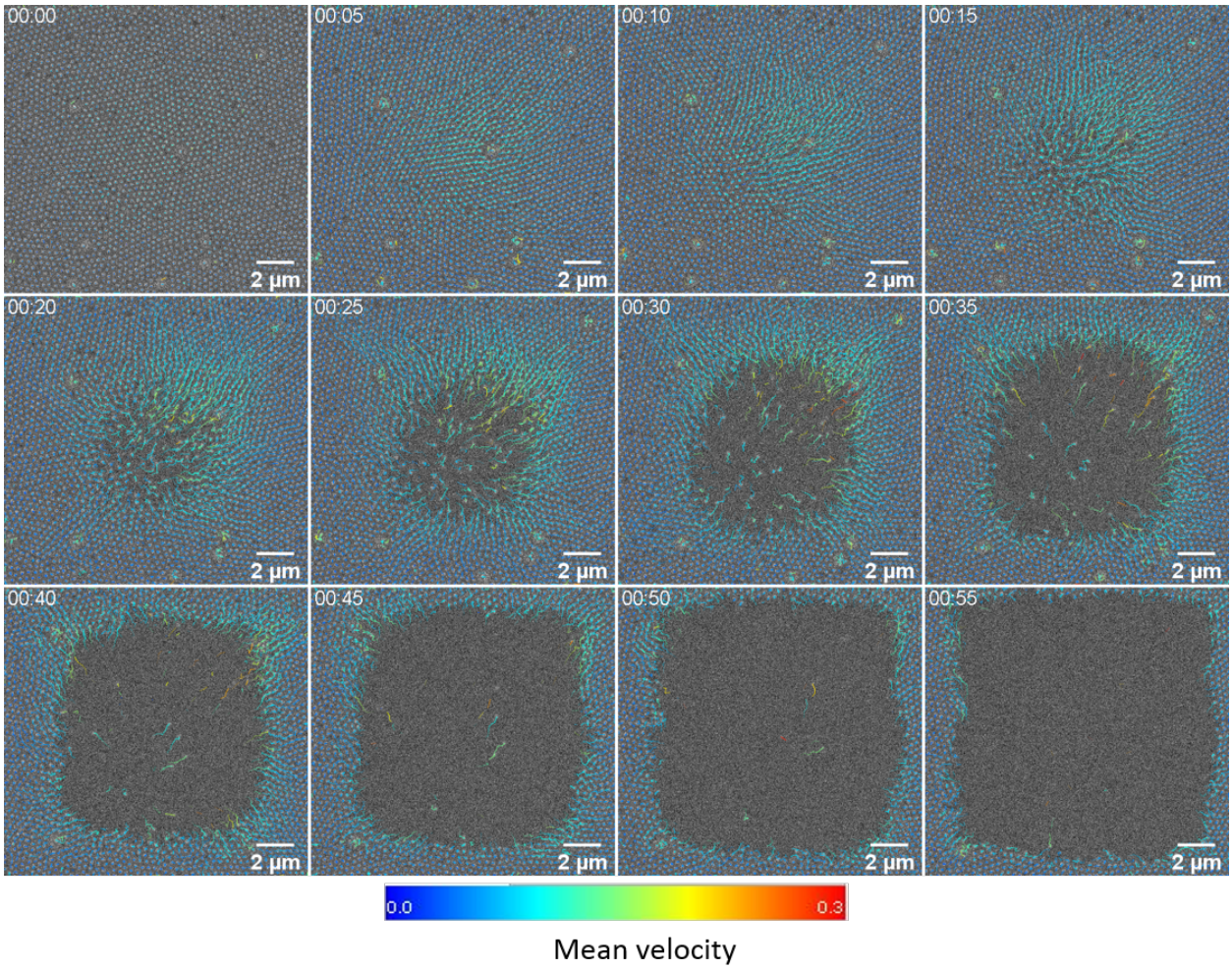

Figure 4.14: Velocity maps of particles showing the trajectory path of up to the previous 15 particle positions, with trajectories colored according to mean particle velocity over the course of the 15 frames. False particle assignments on dopant locations were not removed and incorrectly appear as short lived, fast moving trajectories.

velocity or trajectory length of the 300 nm diameter lattice particle with the position of 1 μm diameter dopant particles.

4.3.5 Summary of experimental results

To consider possible explanations for this dopant concentration dependent monolayer dispersal, we reconsider the known conditions of the experiment. The sample begins as a stationary polycrystalline lattice which is initially formed on the timescale of an hour and then equilibrated overnight. The electron beam deposits energy and charge into the system, which causes the initially static particles to begin to fluctuate and enables the particles in the lattice to explore new configurations. The charge accumulates in the silica particles and the ionic liquid solvent responds by screening this accumulated charge. The presence of the uncharged glycerol serves to reduce the ease with which the ionic liquid ions can form a capacitive double layer around the particle. This initial movement is followed by the decrease in particle density. In previous colloidal monolayer experiments in our lab that did not use glycerol and that were done with different electron beam parameters, particle density was reduced primarily by particles depinning from the surface and sinking into the bulk solution and this sinking was randomly distributed across the field of view [24]. In this case, we observe a combination of particles flowing outward from the center of the frame and some instances of sinking. In both the previously studied system and in this one, the reduction in particle density begins from the center, but a major difference from the previously studied system is that the reduction in particle density is dominated by outward expansion of the monolayer.

We find that the lattice dispersal depends on two things, both of which should therefore play a role in a plausible explanation for this process. The first is the number of dopants in the particle lattice, where a larger number of dopants is correlated with faster dispersal of the lattice. The second is the effect of the electron beam, without which the lattice would remain as a polycrystalline monolayer. Specifically, we find that electron beam perturbation causes the lattice particles to flow outwards. This is consistent with a speculated electron beam induced energy gradient (Section 4.3.2) where either the particles or their surrounding solution flow outwards in response to this gradient. The role of the dopants in this process is less clear, with possible hypotheses presented in Section 4.4.

4.4 Hypotheses for observed colloid dynamics

We find that the number of dopants present in the lattice controls how fast the lattice disperses, with a larger number of dopants leading to faster lattice dispersal. While we have generated a few explanations consistent with this observation, none thus far is definitive.

4.4.1 Dopant-induced changes in particle flow

One possible explanation is that the presence of dopants changes the flow of particles moving out of the frame. Uninterrupted crystal grains have less free volume for the particles to begin moving around in compared to crystal lattices with dopants that inherently break up the lattice packing and co-occur with disordered boundaries and other types of defects. With more accessible area in which the particles can rearrange, the lattice may be able to accommodate the outward flow of the electron beam exposed particles more easily, enabling the dispersal of particles outwards compared to lattices with fewer dopants. Additionally, for a particle in the center of an ordered grain to move to the edge of a frame, the particle must undergo some concerted motion with its neighbors, since there are no open spaces for that particle to move into. If the presence of dopants increases the polycrystallinity of the lattice, the typical length scale of the crystal grain size is decreased, relaxing this constraint.

However, we do not find this to be a complete explanation. While a large number of dopants can result in a more disrupted crystal lattice, the lattice is already polycrystalline without the introduction of dopants. For smaller numbers of dopants, while the dopant position and disordered interface positions appear correlated, this does not necessarily result in an increase in the number of disordered interfaces. By visual inspection of lattices where grains are identified in false color of the Ψ_6 phase, we do not find a large difference in the initial grain size of the lattice, especially in the comparison between one and nine dopants (Figure 4.12), which does result in a notable change in the time of lattice dispersal. Additionally, we use the particle tracking capability to visualize the trajectory and velocity of particles and do not find an obvious difference in particles near or far from dopants, based on visual inspection of trajectories with false color corresponding to particle velocity overlaid on particle image data (Figure 4.14). However, both of these initial analyses of grain polycrystallinity or particle velocity were performed by using some quantitative metric to apply false color to data and perform a visual comparison. A more thorough and completely quantitative analysis, such as computing characteristic grain sizes, directly comparing the distribution of particle velocities at different dopant concentrations, or calculating the correlation between particle velocity and distance from dopants, will provide more insight.

4.4.2 Differential charge buildup

Another possible explanation for the dopant concentration dependence of the monolayer dispersal centers on the differential electron beam interaction with monolayer particles compared to the larger dopant particles. The effect of accelerating voltage on electron beam penetration was simulated using CASINO [19] and considered when selecting imaging conditions (Section 4.2.3) and is further analyzed here. CASINO was used to model the charge deposition in particles of sizes corresponding to the lattice particles and the dopants at different accelerating voltages, neglecting the presence of the solvent (Figure 4.3, experimental condition of 6 kV highlighted in red). The electron beam deposits charge in the particles, which initiates the observed dynamics. Because the dopants are larger than the

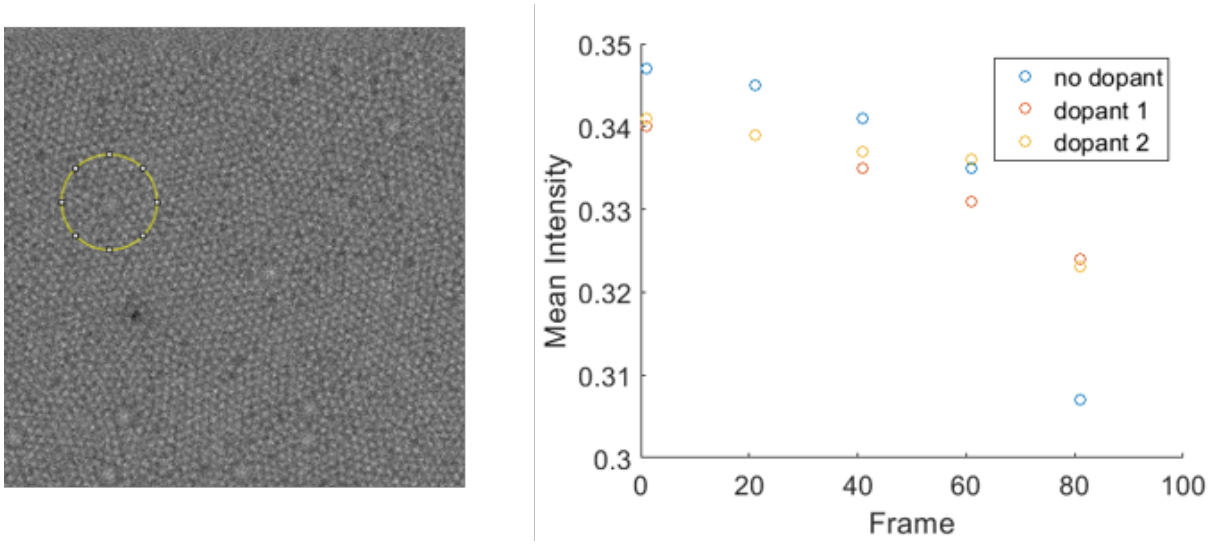

Figure 4.15: Image of example ROI selection and plot of grayscale mean intensity surrounding a dopant.

monolayer particles, the electron beam is absorbed entirely by the dopant particles but penetrates through the smaller monolayer particles (Figure 4.3). Specifically, at 6 kV, 23% of electrons are transmitted through 1 μm diameter dopants, while 87% of electrons are transmitted through 300 nm diameter lattice particles (Figure 4.4, transmitted fraction). Charge buildup in these particles depends greatly on the ability of low energy secondary electrons to escape from the material, which is relatively enhanced in the 300 nm monolayer particles, where the path for escape from any point in the particle is shorter compared to the path a secondary electron must take to escape from the 1 μm dopant. The CASINO simulations show that there should be increased negative charge buildup in the dopant particles compared to the lattice particles, which remain close to neutral charge. While the CASINO simulations do not directly suggest a direct mechanism for charge-based repulsion, if there were some electron beam induced interaction that was repulsive, it would lead to the dispersal of the lattice. In this case, more dopants would cause more overall repulsive interactions and therefore the lattice would disperse more quickly.

We initially assessed this hypothesis by monitoring the grayscale intensity of a region of interest (ROI) centered on a dopant particle, where the grayscale intensity is correlated to the number of particles within the ROI that contribute to a positive signal over the dark background (Figure 4.15). As the lattice disperses, the grayscale intensity decreases, which is consistent with the reduced particle density. However, we do not find a significant difference between the ROI containing a dopant compared to an ROI comprised of only lattice particles, showing that the expected density decrease near a dopant due to repulsive interactions is not apparent with this analysis method. The analysis could be improved by using the already

existing particle and dopant tracking capability, using their positions to calculating the pair distribution function of lattice particles near a dopant to see if less obvious change in the interparticle interaction is occurring. Additionally, since the preferential charge buildup would depend on the depth of the e-beam penetration, measuring monolayer dispersion as a function of accelerating voltage, which would generate different charge deposition depth profiles, would be another means to test this hypothesis.

On the other hand, despite higher simulated charge on the dopants, the ions that comprise the ionic liquid in the solvent are able to screen charge. This likely diminishes any repulsive effects, unless the screening capacity diminishes with increasing amounts of deposited charge controlled by the amount of electron beam exposure. The surface area of a 1 μm diameter dopant particle is 3.14 μm^2, which is 11 times greater than the 0.28 μm^2 surface area of a 300 nm diameter lattice particle. While these areas do not correspond exactly to the submerged area of the particle, this preliminary comparison suggests that the extent of ionic liquid screening should be greater for the dopant particles, given their much larger surface area available for interaction with the ionic liquid. For screening of the particle by the ionic liquid, the ratio of submerged surface area to accumulated charge should control the extent to which the ionic liquid screens the charged particles. An important consideration is that the larger dopant particles intercept more of the electron beam and are more highly charged than the smaller lattice particles (Figure 4.4). Additionally, because the larger dopant particles have a larger radius, the electron beam inputs more electrons into a dopant particle compared to a smaller radius lattice particle. One factor to consider is that we expect that the contact angle between the solvent and particle to remain constant. Since the radius of curvature for the 1μm dopant particles is larger, they should protrude further out of the solvent. Another consideration is the presence of glycerol in the solvent solution, which could diminish the screening effect of the ionic liquid by changing the arrangement of ionic liquid ions near the surface of the silica particles.

4.4.3 Electron beam interaction with ionic liquid and glycerol solution

Yet another dimension to be considered in the experimental interpretation is the interaction between the electron beam and the IL and glycerol bath. The electron beam directly interacts with any exposed liquid above or in the interstices between particles, which are almost fully submerged, and can also penetrate through the 300 nm lattice particles to interact with the liquid beneath those particles. The presence of dopants introduces a different geometry which changes the extent of those interactions, by some combination of increasing the volume of liquid above a dopant particle, changing the size of interstitial regions by disrupting particle packing (Figure 4.16, yellow), or blocking the electron beam from interacting with the liquid layer below the dopant (Figure 4.16, blue). The exact nature of the electron beam interaction with the ionic liquid and glycerol is not obvious, although it can certainly induce chemistry, since prolonged exposure to the electron beam will produce a new material with

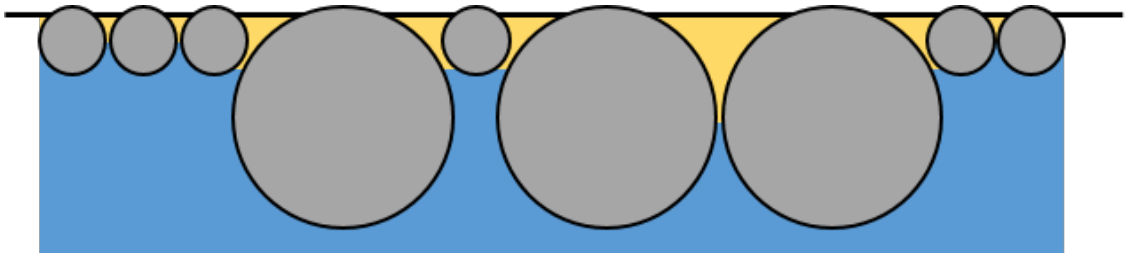

Figure 4.16: Illustration of possible electron beam and liquid interaction volumes. Particles (gray) are drawn to scale in relative diameter but not necessarily to scale in interparticle spacing. Interstitial and above-particle volume is shaded yellow and the liquid layer below lattice particles is shaded blue.

dark contrast, which we speculate to be some polymerized ionic liquid. The buildup of some species in the area of IL/glycerol that interacts with the electron beam, possibly some charged species, radicals, or even heat, would create a gradient in the frame compared to unexposed areas of the sample, possibly then resulting in liquid flow to eliminate the gradient. Because the presence of dopants can tune the extent of electron beam interaction with the liquid, the formation of this gradient and the system's response could plausibly be dependent on the dopant concentration. Since the exact nature of the electron beam interaction with the liquid is not well defined, quantitatively proving this hypothesis presents some difficulty.

4.5 Conclusions and outlook

We are able to consistently produce interfacial polycrystalline colloidal monolayers with large particle dopants at an IL/glycerol-vacuum interface and study their response to electron beam perturbation. A key modification in this system relative to earlier work (Reference [24]) is the introduction of glycerol to the liquid droplet, which at 25% concentration greatly improves the reproducibility with which we can form well-ordered crystalline monolayers. With the doped monolayers, we find that they consistently respond to electron beam perturbation with a reduction in particle density at the center of the field of view due to a combination of outward particle flow and sinking, to fill most of the frame. The rate at which this reduction in monolayer density occurs is dependent on the number of dopants present. While we have not yet fully explained this process, we have outlined several plausible explanations to explore, including dopant-induced changes in particle flow, differential charge buildup in dopant particles compared to lattice particles, and changes in the electron beam interaction with ionic liquid and glycerol caused by the presence of dopants. We will work towards building a model that takes into account the balance of energies, including the interfacial pinning energy and energy accumulated in the particles over the course of the experiment, particle diffusion, and the balance between electrostatic and classical contribu-

tions to the dynamics observed here. Overall, the combination of imaging and simultaneous sample perturbation in SEM imaging is a unique approach to probing the possible dynamics in colloidal monolayers under a non-equilibrium driving protocol.

Chapter 5

Overall conclusions and outlook

Low-dose electron microscopy and cathodoluminescence microscopy are important tools in the imaging science repertoire, especially for capturing dynamics in nanoscale systems. They provide a powerful combination of fast scanning, which enables studying faster dynamics, and nanoscale resolution, which enables studying systems that are inaccessible to other diffraction-limited microscopy techniques. In particular, cathodoluminescence microscopy also enables direct correlation between spatial and photophysical properties.

Using TRCL microscopy, we demonstrated that we can distinguish different Mn^{2+} dopant emitter lifetimes in metal halide perovskite microplates and correlated those changes to the position of the Mn^{2+} dopant in the sample. Measuring changes in the dopant lifetimes allowed us to gain insight into how the dopant's local environment can be used to enhance its emission. In this case, the spatial resolution enabled by the focused electron beam excitation was essential to attribute the change in the lifetime of the Mn^{2+} dopant to the Mn^{2+} at the surface of the host material. TRCL microscopy can be extended to other materials where nanoscale spatial variation in their luminescence properties cannot be understood with changes in emission wavelength or emission intensity alone.

For softer materials, such as organic or biological materials, we have developed CLAIRE microscopy, which retains the spatial and temporal resolution of direct cathodoluminescence microscopy while greatly reducing the damage to the sample caused by the electron beam. We have demonstrated CLAIRE imaging of metal and polymer nanoparticle dynamics, paving the way for the use of nanoparticles as CLAIRE labels and for using CLAIRE to image dynamics in soft materials. We have continued to extend our capabilities, developing a graphene encapsulation method to make CLAIRE compatible with aqueous samples and performing preliminary experiments towards label-free CLAIRE imaging of photosynthetic membranes. Overall, this work provides a foundation for CLAIRE as a minimally invasive super-resolution microscopy technique that is well suited for imaging dynamics in soft materials at the nanoscale.

For non-luminescent samples, low dose electron microscopy is a powerful technique for imaging dynamics. We used low-dose SEM to drive and characterize the dynamics of a colloidal monolayer comprised of nanoparticles assembled at the surface of an ionic liquid

droplet. While the ionic liquid is sensitive to electron beam exposure, we demonstrate that with careful management of the electron dose, this does not prevent the use of SEM to characterize the dynamics.

Together, these studies show that low-dose SEM-based imaging is powerful for characterizing a range of different systems, all requiring nanoscale spatial resolution and fast temporal resolution.

Bibliography

(1) Guigas, G.; Weiss, M. *Biochimica et Biophysica Acta (BBA) - Biomembranes* **2016**, *1858*, 2441–2450.

(2) Trimble, W. S.; Grinstein, S. *The Journal of Cell Biology* **2015**, *208*, 259–271.

(3) Boles, M. A.; Engel, M.; Talapin, D. V. *Chemical Reviews* **2016**, *116*, 11220–11289.

(4) Li, S.; Guo, X.; Sun, M.; Qu, A.; Hao, C.; Wu, X.; Guo, J.; Xu, C.; Kuang, H.; Xu, L. *Nanoscale* **2021**, *13*, 2302–2311.

(5) Walla, P. J. In *Modern Biophysical Chemistry*; John Wiley & Sons, Ltd: 2014, pp 169–182.

(6) Hecht, E. In *Optics*, 3rd ed; Addison-Wesley: 1998, pp 433–511.

(7) Wen, H.; Cherukara, M. J.; Holt, M. V. *Annual Review of Materials Research* **2019**, *49*, 389–415.

(8) Shapiro, D.; Thibault, P.; Beetz, T.; Elser, V.; Howells, M.; Jacobsen, C.; Kirz, J.; Lima, E.; Miao, H.; Neiman, A. M.; Sayre, D. *Proceedings of the National Academy of Sciences* **2005**, *102*, 15343–15346.

(9) Walla, P. J. In *Modern Biophysical Chemistry*; John Wiley & Sons, Ltd: 2014, pp 183–202.

(10) Hauser, M.; Wojcik, M.; Kim, D.; Mahmoudi, M.; Li, W.; Xu, K. *Chemical Reviews* **2017**, *117*, 7428–7456.

(11) Garcia, R. *Chemical Society Reviews* **2020**, *49*, 5850–5884.

(12) Raybin, J.; Ren, J.; Chen, X.; Gronheid, R.; Nealey, P. F.; Sibener, S. J. *Nano Letters* **2017**, *17*, 7717–7723.

(13) Dunn, R. C. *Chemical Reviews* **1999**, *99*, 2891–2928.

(14) Kim, J.; Song, K.-B. *Micron* **2007**, *38*, 409–426.

(15) Reimer, L., *Scanning Electron Microscopy: Physics of Image Formation and Microanalysis*, 2nd ed; Springer: 1998.

(16) Goldstein, J. I.; Newbury, D. E.; Michael, J. R.; Ritchie, N. W. M.; Scott, J. H. J.; Joy, D. C. In *Scanning Electron Microscopy and X-Ray Microanalysis*, Goldstein, J. I., Newbury, D. E., Michael, J. R., Ritchie, N. W., Scott, J. H. J., Joy, D. C., Eds.; Springer: New York, NY, 2018, pp 111–121.

(17) Bischak, C. G.; Sanehira, E. M.; Precht, J. T.; Luther, J. M.; Ginsberg, N. S. *Nano Letters* **2015**, *15*, 4799–4807.

(18) Goldstein, J. I.; Newbury, D. E.; Michael, J. R.; Ritchie, N. W. M.; Scott, J. H. J.; Joy, D. C. In *Scanning Electron Microscopy and X-Ray Microanalysis*, Goldstein, J. I., Newbury, D. E., Michael, J. R., Ritchie, N. W., Scott, J. H. J., Joy, D. C., Eds.; Springer: New York, NY, 2018, pp 147–164.

(19) Demers, H.; Poirier-Demers, N.; Couture, A. R.; Joly, D.; Guilmain, M.; Jonge, N. d.; Drouin, D. *Scanning* **2011**, *33*, 135–146.

(20) Franken, L. E.; Grünewald, K.; Boekema, E. J.; Stuart, M. C. A. *Small* **2020**, *16*, 1906198.

(21) Muller, D. A. *Nature Materials* **2009**, *8*, 263–270.

(22) Ophus, C. *Microscopy and Microanalysis* **2019**, *25*, 563–582.

(23) Egerton, R. F.; Malac, M. *Journal of Electron Spectroscopy and Related Phenomena* **2005**, *143*, 43–50.

(24) Bischak, C. G.; Raybin, J. G.; Kruppe, J. W.; Ginsberg, N. S. *Soft Matter* **2020**, *16*, 9578–9589.

(25) Manoharan, V. N. *Science* **2015**, *349*, DOI: `10.1126/science.1253751`.

(26) Kohlstedt, K. L.; Glotzer, S. C. *Physical Review E* **2013**, *87*, 032305.

(27) Yacobi, B. G.; Holt, D. B., *Cathodoluminescence Microscopy of Inorganic Solids*; Plenum Press: 1990.

(28) Bischak, C. G.; Hetherington, C. L.; Wu, H.; Aloni, S.; Ogletree, D. F.; Limmer, D. T.; Ginsberg, N. S. *Nano Letters* **2017**, *17*, 1028–1033.

(29) Bischak, C. G.; Wong, A. B.; Lin, E.; Limmer, D. T.; Yang, P.; Ginsberg, N. S. *The Journal of Physical Chemistry Letters* **2018**, *9*, 3998–4005.

(30) Guria, A. K.; Dutta, S. K.; Adhikari, S. D.; Pradhan, N. *ACS Energy Letters* **2017**, *2*, 1014–1021.

(31) Das Adhikari, S.; Guria, A. K.; Pradhan, N. *The Journal of Physical Chemistry Letters* **2019**, *10*, 2250–2257.

(32) Parobek, D.; Roman, B. J.; Dong, Y.; Jin, H.; Lee, E.; Sheldon, M.; Son, D. H. *Nano Letters* **2016**, *16*, 7376–7380.

(33) Liu, W.; Lin, Q.; Li, H.; Wu, K.; Robel, I.; Pietryga, J. M.; Klimov, V. I. *Journal of the American Chemical Society* **2016**, *138*, 14954–14961.

(34) Mir, W. J.; Jagadeeswararao, M.; Das, S.; Nag, A. *ACS Energy Letters* **2017**, *2*, 537–543.

(35) Lin, C. C.; Xu, K. Y.; Wang, D.; Meijerink, A. *Scientific Reports* **2017**, *7*, 1–10.

(36) Liu, H.; Wu, Z.; Shao, J.; Yao, D.; Gao, H.; Liu, Y.; Yu, W.; Zhang, H.; Yang, B. *ACS Nano* **2017**, *11*, 2239–2247.

(37) Zou, S.; Liu, Y.; Li, J.; Liu, C.; Feng, R.; Jiang, F.; Li, Y.; Song, J.; Zeng, H.; Hong, M.; Chen, X. *Journal of the American Chemical Society* **2017**, *139*, 11443–11450.

(38) Yuan, X.; Ji, S.; De Siena, M. C.; Fei, L.; Zhao, Z.; Wang, Y.; Li, H.; Zhao, J.; Gamelin, D. R. *Chemistry of Materials* **2017**, *29*, 8003–8011.

(39) De, A.; Mondal, N.; Samanta, A. *Nanoscale* **2017**, *9*, 16722–16727.

(40) J. Mir, W.; Swarnkar, A.; Nag, A. *Nanoscale* **2019**, *11*, 4278–4286.

(41) Dastidar, S.; Egger, D. A.; Tan, L. Z.; Cromer, S. B.; Dillon, A. D.; Liu, S.; Kronik, L.; Rappe, A. M.; Fafarman, A. T. *Nano Letters* **2016**, *16*, 3563–3570.

(42) Zhu, J.; Yang, X.; Zhu, Y.; Wang, Y.; Cai, J.; Shen, J.; Sun, L.; Li, C. *The Journal of Physical Chemistry Letters* **2017**, *8*, 4167–4171.

(43) Biswas, A.; Bakthavatsalam, R.; Kundu, J. *Chemistry of Materials* **2017**, *29*, 7816–7825.

(44) Chen, D.; Fang, G.; Chen, X.; Lei, L.; Zhong, J.; Mao, Q.; Zhou, S.; Li, J. *Journal of Materials Chemistry C* **2018**, *6*, 8990–8998.

(45) Xu, K.; Vliem, J. F.; Meijerink, A. *The Journal of Physical Chemistry C* **2019**, *123*, 979–984.

(46) Rossi, D.; Parobek, D.; Dong, Y.; Son, D. H. *The Journal of Physical Chemistry C* **2017**, *121*, 17143–17149.

(47) Huang, G.; Wang, C.; Xu, S.; Zong, S.; Lu, J.; Wang, Z.; Lu, C.; Cui, Y. *Advanced Materials* **2017**, *29*, 1700095.

(48) Das Adhikari, S.; Dutta, S. K.; Dutta, A.; Guria, A. K.; Pradhan, N. *Angewandte Chemie International Edition* **2017**, *56*, 8746–8750.

(49) Xu, K.; Lin, C. C.; Xie, X.; Meijerink, A. *Chemistry of Materials* **2017**, *29*, 4265–4272.

(50) Chen, D.; Fang, G.; Chen, X. *ACS Applied Materials & Interfaces* **2017**, *9*, 40477–40487.

(51) He, T.; Li, J.; Ren, C.; Xiao, S.; Li, Y.; Chen, R.; Lin, X. *Applied Physics Letters* **2017**, *111*, 211105.

(52) Fei, L.; Yuan, X.; Hua, J.; Ikezawa, M.; Zeng, R.; Li, H.; Masumoto, Y.; Zhao, J. *Nanoscale* **2018**, *10*, 19435–19442.

(53) Li, Z.-J.; Hofman, E.; Davis, A. H.; Khammang, A.; Wright, J. T.; Dzikovski, B.; Meulenberg, R. W.; Zheng, W. *Chemistry of Materials* **2018**, *30*, 6400–6409.

(54) Ji, S.; Yuan, X.; Li, J.; Hua, J.; Wang, Y.; Zeng, R.; Li, H.; Zhao, J. *The Journal of Physical Chemistry C* **2018**, *122*, 23217–23223.

(55) Das Adhikari, S.; Behera, R. K.; Bera, S.; Pradhan, N. *The Journal of Physical Chemistry Letters* **2019**, *10*, 1530–1536.

(56) Dutta, S. K.; Pradhan, N. *The Journal of Physical Chemistry Letters* **2019**, *10*, 6788–6793.

(57) Pinchetti, V.; Anand, A.; Akkerman, Q. A.; Sciacca, D.; Lorenzon, M.; Meinardi, F.; Fanciulli, M.; Manna, L.; Brovelli, S. *ACS Energy Letters* **2019**, *4*, 85–93.

(58) Wei, Q.; Li, M.; Zhang, Z.; Guo, J.; Xing, G.; Sum, T. C.; Huang, W. *Nano Energy* **2018**, *51*, 704–710.

(59) Berezin, M. Y.; Achilefu, S. *Chemical reviews* **2010**, *110*, 2641–2684.

(60) Cole, M. J.; Siegel, J.; Webb, S. E. D.; Jones, R.; Dowling, K.; Dayel, M. J.; Parsons-Karavassilis, D.; French, P. M. W.; Lever, M. J.; Sucharov, L. O. D.; Neil, M. a. A.; Juškaitis, R.; Wilson, T. *Journal of Microscopy* **2001**, *203*, 246–257.

(61) Bastiaens, P. I. H.; Squire, A. *Trends in Cell Biology* **1999**, *9*, 48–52.

(62) Duong, T.; Mulmudi, H. K.; Shen, H.; Wu, Y.; Barugkin, C.; Mayon, Y. O.; Nguyen, H. T.; Macdonald, D.; Peng, J.; Lockrey, M.; Li, W.; Cheng, Y.-B.; White, T. P.; Weber, K.; Catchpole, K. *Nano Energy* **2016**, *30*, 330–340.

(63) Dar, M. I.; Jacopin, G.; Hezam, M.; Arora, N.; Zakeeruddin, S. M.; Deveaud, B.; Nazeeruddin, M. K.; Grätzel, M. *ACS Photonics* **2016**, *3*, 947–952.

(64) Atre, A. C.; Brenny, B. J. M.; Coenen, T.; García-Etxarri, A.; Polman, A.; Dionne, J. A. *Nature Nanotechnology* **2015**, *10*, 429–436.

(65) Cortecchia, D.; Lew, K. C.; So, J.-K.; Bruno, A.; Soci, C. *Chemistry of Materials* **2017**, *29*, 10088–10094.

(66) Ponce, F. A.; Srinivasan, S.; Bell, A.; Geng, L.; Liu, R.; Stevens, M.; Cai, J.; Omiya, H.; Marui, H.; Tanaka, S. *physica status solidi (b)* **2003**, *240*, 273–284.

(67) Moerland, R. J.; Weppelman, I. G. C.; Garming, M. W. H.; Kruit, P.; Hoogenboom, J. P. *Optics Express* **2016**, *24*, 24760–24772.

(68) Aiello, C. D.; Pickel, A. D.; Barnard, E.; Wai, R. B.; Monachon, C.; Wong, E.; Aloni, S.; Ogletree, D. F.; Dames, C.; Ginsberg, N. *arXiv:1810.07581 [cond-mat, physics:physics]* **2018**, arXiv: 1810.07581.

(69) Schindelin, J. et al. *Nature Methods* **2012**, *9*, 676–682.

(70) Luo, B.; Guo, Y.; Li, X.; Xiao, Y.; Huang, X.; Zhang, J. Z. *The Journal of Physical Chemistry C* **2019**, *123*, 14239–14245.

(71) Sun, Q.; Wang, S.; Zhao, C.; Leng, J.; Tian, W.; Jin, S. *Journal of the American Chemical Society* **2019**, DOI: 10.1021/jacs.9b09143.

(72) Bradac, C.; Gao, W.; Forneris, J.; Trusheim, M. E.; Aharonovich, I. *Nature Communications* **2019**, *10*, 5625.

(73) Castelletto, S.; Boretti, A. *Journal of Physics: Photonics* **2020**, *2*, 022001.

(74) Bischak, C. G.; Hetherington, C. L.; Wang, Z.; Precht, J. T.; Kaz, D. M.; Schlom, D. G.; Ginsberg, N. S. *Nano Letters* **2015**, *15*, 3383–3390.

(75) Walla, P. J. In *Modern Biophysical Chemistry*; John Wiley & Sons, Ltd: 2014, pp 61–104.

(76) Bischak, C. G.; Wai, R. B.; Cherqui, C.; Busche, J. A.; Quillin, S. C.; Hetherington, C. L.; Wang, Z.; Aiello, C. D.; Schlom, D. G.; Aloni, S.; Ogletree, D. F.; Masiello, D. J.; Ginsberg, N. S. *ACS Nano* **2017**, *11*, 10583–10590.

(77) Yuk, J. M.; Park, J.; Ercius, P.; Kim, K.; Hellebusch, D. J.; Crommie, M. F.; Lee, J. Y.; Zettl, A.; Alivisatos, A. P. *Science* **2012**, *336*, 61–64.

(78) Cho, H.; Jones, M. R.; Nguyen, S. C.; Hauwiller, M. R.; Zettl, A.; Alivisatos, A. P. *Nano Letters* **2017**, *17*, 414–420.

(79) Rasool, H.; Dunn, G.; Fathalizadeh, A.; Zettl, A. *physica status solidi (b)* **2016**, *253*, 2351–2354.

(80) Lapina, V. A.; Pavich, T. A.; Pershukevich, P. P.; Trofimov, A. V.; Trofimova, N. N.; Tsaplev, Y. B.; Zak, P. P. *Journal of Physical Organic Chemistry* **2017**, *30*, e3731.

(81) Kasry, A.; Ardakani, A. A.; Tulevski, G. S.; Menges, B.; Copel, M.; Vyklicky, L. *The Journal of Physical Chemistry C* **2012**, *116*, 2858–2862.

(82) Boekema, E. J.; van Breemen, J. F. L.; van Roon, H.; Dekker, J. P. *Journal of Molecular Biology* **2000**, *301*, 1123–1133.

(83) Onoa, B.; Fukuda, S.; Iwai, M.; Bustamante, C.; Niyogi, K. K. *Biophysical Journal* **2020**, *118*, 1876–1886.

(84) nanoComposix Silica Frequently Asked Questions. https://nanocomposix.com/pages/silica-frequently-asked-questions-faq (accessed Aug 12, 2021).

(85) Chai, Y.; Hasnain, J.; Bahl, K.; Wong, M.; Li, D.; Geissler, P.; Kim, P. Y.; Jiang, Y.; Gu, P.; Li, S.; Lei, D.; Helms, B. A.; Russell, T. P.; Ashby, P. D. *Science Advances* **2020**, *6*, eabb8675.

(86) Rola, K. P.; Zając, A.; Szpecht, A.; Kowal, D.; Cybińska, J.; Śmiglak, M.; Komorowska, K. *European Polymer Journal* **2021**, *156*, 110615.

(87) Minamimoto, H.; Irie, H.; Uematsu, T.; Tsuda, T.; Imanishi, A.; Seki, S.; Kuwabata, S. *Langmuir* **2015**, *31*, 4281–4289.

(88) Fröba, A. P.; Kremer, H.; Leipertz, A. *The Journal of Physical Chemistry B* **2008**, *112*, 12420–12430.

(89) Alkindi, A. S.; Al-Wahaibi, Y. M.; Muggeridge, A. H. *Journal of Chemical & Engineering Data* **2008**, *53*, 2793–2796.